University of Puerto Rico
Río Piedras Campus
Faculty of Natural Sciences
Department of Chemistry

Pt-based Electrocatalysts for Energy Conversion Reactions: An Electrochemical *In Situ* X-ray Absorption Spectroscopy Approach in Alkaline Medium

By

Joesene Javier Soto Pérez

A Dissertation Presented in Partial Fulfillment
Of the Requirement for the Degree of

Doctor of Philosophy

April 26, 2022

Accepted by the Faculty of the Department of Chemistry of the University of Puerto Rico in Partial Fulfillment of Requirement to obtain the degree of

Doctor of Philosophy

Dr. Liz M. Díaz Vázquez

Department Chair

Dr. Carlos R. Cabrera Martínez

Thesis Advisor

Dr. Jorge Colón

Thesis Committee Member

Dr. Mitk'El Santiago

Thesis Committee Member

Dr. Eduardo Nicolau

Thesis Committee Member

April 26, 2022

Dedication

To my grandmother, Hilda Luz Díaz Castro.

Acknowledgments

I would like to first appreciate all the help from Dr. Carlos R. Cabrera Martínez through out the past 7 years. He started being my advisor during the last two years of my undergraduate coursework. Due to my gratifying experience, I decided to continue my graduate journey with him at the University of Puerto Rico, Río Piedras. The last five years have been quite challenging, considering the different atmospheric phenomena and the economic circumstances in the UPR system. However, Dr. Cabrera has always found a way to pursue frontier scientific research, even if it required going out of campus. He always has his students as a priority; I will always be thankful for all the opportunities he has presented me, which are a significant part of the scientist and human being I am today. For this and many other things, I will always be grateful.

I acknowledge all the recommendations and mentorship of the members of my thesis committee, Dr. Jorge Colón, Dr. Eduardo Nicolau and Dr. Mitk'El B. Santiago. These recommendations helped me to shape my scientific work over the past five years. I would also like to thank Dr. Cabrera's research group. First, to the graduate students and colleagues, Dr. Myreisa Morales and Dr. Carlos Vélez, which were my graduate mentors when I was an undergrad student. Many of the fundamental aspects of practical electrochemistry that I developed were thanks to their mentorship. As for the practical aspects related to the use of a synchrotron source, I acknowledge Dr. Luis Betancourt and Dr. Juan Corchado for all the conversations, guidance and feedback regarding data and experimental protocols. I would also like to thank Armando Peña Duarte for constantly listening to my ideas

and providing valuable feedback. To Dr. Camila Morales for allowing me to explore and collaborate on different projects outside my scope regarding environmental remediation methods.

I also like to acknowledge undergraduate students, specifically Glen Torres, Gerardo Quintana, and Pedro Trinidad. Thanks to them, much of the research presented here was possible. The many hours spent in the laboratory, our first missed steps, the long hours of experimental synthesis, and the discussion of ideas are part of the product of my scientific accomplishments. Specifically, I would like to acknowledge Pedro Trinidad because he decided to join me in the second semester of my first graduate year and has been here through this entire journey; Pedro, much of the work here is thanks to you. I wish you great luck in your voyage to Graduate School, and for that, I am incredibly proud.

The acknowledgments now extend to our collaborators. To the personnel at Brookhaven National Laboratory (BNL), specifically Noel Blackburn, for being after Hurricane María in 2017 and opening BNL to continue our research. To Dr. Sanjaya Senanayake for always being at the disposition to provide any help when we went to BNL. To Dr. Kotaro Sasaki and the Surface Electrochemistry and Electrocatalysis group for receiving me with open doors for 6 months in 2021, providing valuable scientific recommendations and ideas. To the Cornell High energy Synchrotron Source (CHESS) personnel, specifically Dr. Kenneth Finkelstein, for being my mentor during my internship at CHESS providing fundamental aspects of synchrotron science. To Dr. Christopher Pollock and Dr. Louise Debefve for always being at their disposition to discuss synchrotron results

and helping us at our beamtimes. To Prof. Héctor D. Abruña for having his laboratory doors open all the time when we went to Cornell University and for being a mentor. To Dr. Abruña's students, Yao Yang, Andrés Molina, and Rui Zeng, for providing any help when I was in the laboratory.

I want to acknowledge my family for always being supportive without understanding what I was doing at the laboratory. To my sister, Tania Soto and my brother, Gabino Irizarry, for always believing in me regarding the circumstances and providing support and care in this journey, to my mother Liana Pérez, for giving her best at providing the best future for us, to my father Enrique Soto for being present at needed times, to my step-father Gabino Irizarry, for providing help in any way and to my uncles Cuco, Lulu, Eggie, Sandra and César. To my friends Javier, Robert, Bryant and the many I created along this journey—you are all part of my accomplishments. And to my beloved grandmother, Hilda Díaz to whom I will be forever in debt, thank you for providing a home at difficult times. I would also like to acknowledge my other collaborators, Javier Rivera, Alondra Rodríguez, Dr. Ricardo Martínez, Dr. Ratnakar Palai and Dr. Md. Ariful Hasan; thank you for trusting me in your scientific work.

I would finish by recognizing the financial support I have received from different organizations, firstly from the National Science Foundation (NSF) Center for Innovation Research and Education in Environmental Nanotechnology (CREST) Grant No.173609 and to the NSF-Partnerships for Research and Education in Materials (PREM) Center for Interfacial Electrochemistry of Energy Materials grant number (CIE^{2}M) Grant No. DMR-1827622E. I appreciate all the

help from the PREM-CIE^{2}M administrative and scientific staff for being at the disposition related to paperwork, travel plans and scientific conferences. I will also want to recognize the NSF-INTERN supplement awarded in 2021, which provided funds for my internship at BNL. The use of the Cornell Center for Materials Research Shared Facilities, which are supported through the NSF MRSEC grant number DMR-1719875, is greatly appreciated. This research used resources of the 7-BM QAS beamline of the National Synchrotron Light Source II, a U.S. Department of Energy (DOE) Office of Science User Facility operated for the DOE Office of Science by Brookhaven National Laboratory under Contract No. DE-SC0012704. This work is also based upon research conducted at the Center for High Energy X-ray Sciences (CHEXS) which is supported by the NSF under award DMR-1829070.

Abstract

It is well established that energy use via fossil fuels can be related to global warming; this renders higher atmospheric carbon dioxide levels. The migration to renewable energy technologies has proven to be an alternative to mitigate the contamination associated with fossil fuels. However, an overpotential is associated with the energy conversion reactions in renewable technologies (e.g., batteries and fuel cells (FC)). This overpotential can be minimized by incorporating effective electrocatalysts considering cost, abundance, and durability. The Oxygen reduction reaction (ORR) plays a crucial role in FCs; it has been demonstrated that at a low pH (Proton exchange membrane fuel cells (PEMFCs)), the ORR has sluggish kinetics. However, higher pH levels have been demonstrated to enhance the ORR (Alkaline exchange membrane fuel cells (AEMFCs))—opening the opportunity to explore different electrocatalysts as low-loading Platinum group metals (PGM) alloyed with first transition metals, metal oxides and non-precious metals.

In this thesis, we presented the synthesis, characterization, and performance measurements of PGM electrocatalyst alloyed to first-row transition metals for the electroreduction of oxygen in an alkaline medium. A new approach was taken to synthesizing PtNi-Nanowires (NWs) supported on Vulcan XC-72R (V) by hydrothermal synthesis and spontaneous galvanic displacement (SGD). The rotating disk-slurry electrodeposition (RoDSE) technique was used for the first time to synthesize Ni/V, Co/V and Cu/V nanoparticles and by the SGD PtNi/V, PtCo/ V and PtCu/V nanoparticles were obtained. The catalysts were submitted to

durability experiments showing similar behavior to Pt/C commercial catalyst after 10,000 and 30,000 cycles. *In situ* electrochemical X-ray absorption spectroscopy (XAS) was used to test these nanowires and nanoparticles, confirming their testing capability in an alkaline medium for the ORR and providing evidence for alloy interaction.

The Pb electroless (e-less) deposition method was explored with Au, Nb and Cu catalysts as monocrystals and nanoparticles. The PdCu (100) catalysts were obtained by the Pb e-less method. The Pd monolayer (ML) formation on Cu (100) was proven by charge density calculations on the Pb underpotential deposition (UPD) region. The PdCu (100) were submitted to ORR testing and showed better performance than Pd (*hkl*) electrocatalyst in an alkaline medium. These results suggest that the synthesis of low PGM loadings electrocatalyst can drive the ORR in an alkaline medium with enhanced performance compared to commercial Pt/C catalysts.

Table of contents

List of tables

List of figures

List of equations

List of abbreviations and symbols

A	Amperes
ADF	Annular dark field
AEMFC	Alkaline exchange membrane Fuel Cell
Ag/AgCl	Silver silver chloride electrode
At%	Atomic percentage
BF	Bright field
BNL	Brookhaven National Laboratory
C	Coulombs
C_0	Solubility of gas
CE	Counter electrode
CFN	Center for Functional Nanomaterials
CV	Cyclic voltammetry
D_0	Diffusion coefficient
DEO	Department of energy
E	Potential
E1/2	Half-wave potentical
ECSA	Electrochemical Surface Area
EDS	Energy Dispersive X-Ray Spectroscopy

E-less	electroless
E_{onset}	Onset potential
EXAFS	Extended X-ray absorption fine structure
F	Faraday constant
FC	Fuel cell
fcc	Face centered cubic
FFT	Fast Fourier transformation
GC	Glassy carbon electrode
HAADF	High Angle Annular Dark Field Scanning Transmission Electron
HER	Hydrogen evolution reaction
HgO/Hg	Mercury oxide
HOPR	High overpotential region
HRTEM	High Resolution Transmission Electron Microscopy
HUPD	Hydrogen desorption region
I	Current
ICP-OES	Inductively Coupled Plasma Optical emission spectroscopy
IR	Internal Resistance
j	Current Density

jk	Kinetic Current
jL	Limiting current
KL	Koutecký-Levich
LOPR	Low overpotential region
LSV	Linear sweep voltammetry
MEA	Membrane electrode assembly
ML	Monolayer
n	Electrons transferred
NPs	Nanoparticles
NSF	National Science Foundation
NSLS	National synchrotron light source
NSLS-II	National synchrotron light source II
NWs	Nanowires
OCP	Open circuit potential
OER	Oxygen Evolution Reaction
ORR	Oxygen Reduction Reaction
PbED	Lead e-less deposition
PEMFC	Proton Exchange Membrane Fuel Cell

PGM	Platinum group metals
PIPS	Passivated implanted planar silicon
PXRD	Powder X-ray diffraction
QAS	Quick X-ray absorption
R	Gas constant
RDE	Rotating disk electrode
RE	Reference electrode
REA	Real surface area
RHE	Reversible Hydrogen Electrode
RoDSE	Rotating disk slurry electrodeposition
rpm	Revolutions per minute
SEM	Scanning Electron Microscopy
SGD	Spontaneous galvanic displacement
SHE	Standard Hydrogen Electrodes
STEM	Scanning Transmission Electron Microscopy
UHP	Ultra high purity
UPD	Underpotential deposition
UV-vis	Ultraviolet-visible

V	Vulcan XC-72R
V_0	Kinematic viscosity
w/w %	Weight percentage
WE	Working Electrode
XAFS	X-ray absorption fine-structure
XANES	X-ray Ray absorption near edge structure
XAS	X-ray absorption spectroscopy
XRD	X-ray Diffraction
XPS	X-ray photoelectron spectroscopy
XRD	X-ray diffraction
Ω	Ohms

Chapter 1. **Introduction**

1.1. Renewable energy

Fossil fuels have been the primary source of energy generation for decades. Its continuous consumption is linked to increased greenhouse gas pollutants related to global warming. This leads us to recognize that technological advances are essential to replace our current fuel dependency.[1] The continued development of energy technologies such as photovoltaic devices, fuel cells (FCs) and batteries could provide a path for this sustainable energy landscape.[2] Among the technologies, clean hydrogen production has gathered recent interest for transport decarbonization[3], as seen from governments investing in energy programs as the hydrogen shot[4] from the US's Department of Energy (DOE). Clean hydrogen could be obtained using water splitting reactions—Hydrogen evolution reaction (HER) and oxygen evolution reaction (OER).[5] This hydrogen could be stored and used in technologies such as in hydrogen alkaline FCs, which are great contenders to replace combustion vehicles.[6]

Proton exchange membrane fuel cells (PEMFCs) can potentially fulfill energy demands at a lower environmental cost.[7] In PEMFCs, the driving of the electrochemical reactions—Hydrogen oxidation reaction (HOR) and Oxygen reduction reaction (ORR)—at high rates hinges on using high loadings of electrocatalysts to lower the associated overpotentials and promote reaction kinetics.[8,9] An alternative is to bring back anion exchange membrane fuel cells (AEMFCs), where the ORR has enhanced kinetics and enables the use of non-

precious metals and metal oxides.[10,11] To improve the technology, it is essential to know how AEMFCs work, see **Figure 1.1**.

1.2. Alkaline exchange membrane fuel cells

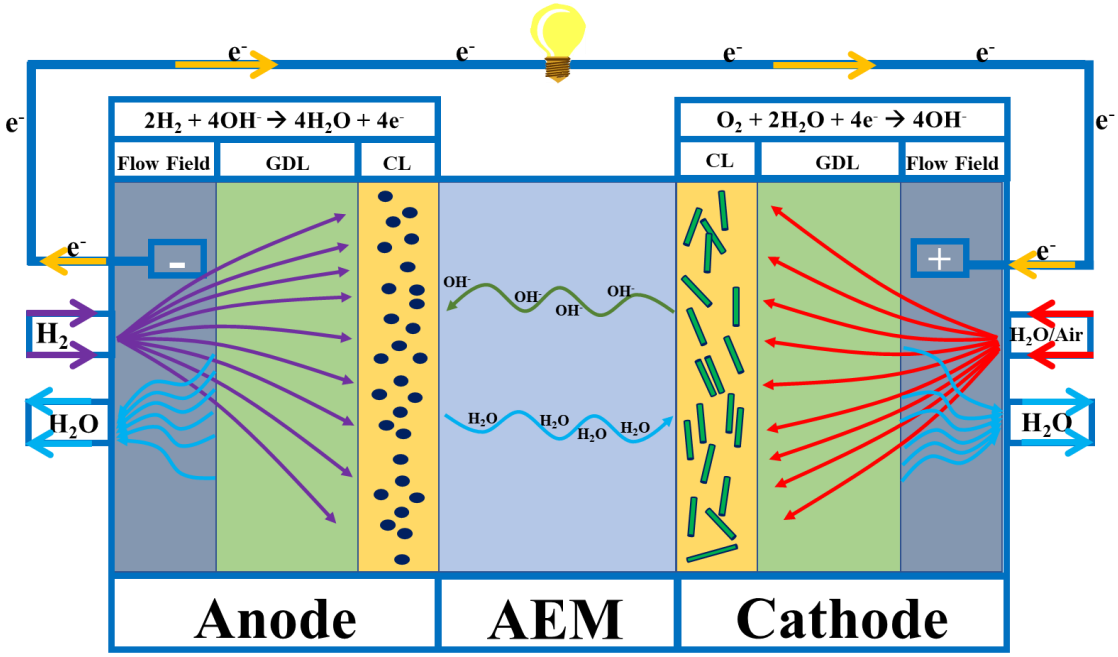

Figure 1.1 Representation of a hydrogen-based AEMFC with the main species being generated.

A FC is a galvanic cell that transforms chemical energy into electrical energy; this energy can be expressed as current via a spontaneous process. The chemical reactions at the FC are explained as follows.[12] At the anode compartment is where the HOR occurs,as shown in **Equation 1.1**.

$$2H_2 + 4OH^- \rightarrow 4H_2O + 4e^- \qquad \textbf{Eq. 1.1}$$

Then, e^- passes through a gas diffusion layer (GDL) and a catalyst layer (CL), where the catalyst of interest is placed. Water passes through the anion exchange membrane (AEM) and starts to behave as a reactant in the ORR. The ORR

reaction occurs at the cathode compartment and has a thermodynamic potential of 1.23 V vs. NHE. The overall reaction is stated in the diagram and **Equation 1.2**.

$$O_2 + 2H_2O + 4e^- \rightarrow 4OH^- \qquad \textbf{Eq. 1.2}$$

It is important to recall that the flow of e^- is from the anode to the cathode via the different layers and the AEM. The AEM helps keep the electroneutrality of all the FC by transferring water molecules and OH^-. The anions present in the FC, with OH^- being the most predominant species across the membrane, are generated via **Equation 1.3**.

$$O_2 + H_2O + 2e^- \rightarrow OH^- + HO_2^- \qquad \textbf{Eq. 1.3}$$

$$HO_2^- + H_2O + 2e^- \rightarrow 3OH^- \qquad \textbf{Eq. 1.4}$$

Then, the OH^- are transported to the anode, reacting with H_2 as the fuel source and carrying on with the HOR as shown in **Equation 1.1**. The essential factor here is to drive the ORR by the 4 e^- pathway. This pathway is related to the production of OH^- in the cathode and twice as much water in the anode compared with PEMFCs.[13]

FCs could replace the internal combustion engine and revolutionize the vehicle industry by reducing the abundance of gaseous emissions such as CO_2. Alternate vehicles powered by batteries are an option. However, hydrogen FCs have an advantage over batteries by having faster charging/fueling rates, higher energy efficiencies, and a more extended operating range (distance).[14–16] An ongoing challenge to extending FCs into a broader range of applications is to increase their performance while reducing the cost of manufacturing. Catalyst

materials can reduce the cost of the FC assembly; thus, researchers are attempting to improve their chemical constitution and structure without sacrificing performance activity.

1.3. Platinum group metal catalysts

Platinum group metal catalysts (PGM) are the most studied and used in FC applications because they can be used in both HER and ORR reactions.[17] PGM alloys, core shells and non-precious metals are the leading contenders to replace PGM catalysts.[18] Since an overpotential is commonly associated with FC catalysts, trends using O_2 and OH^- binding energy has been used to understand and gain insights to improve the electrochemical reduction of O_2.[19] In addition, the limiting potential and density functional theory (DFT) kinetic volcano computations with have been used to predict experimental activity trends for a variety of materials successfully, see **Figure 1.2**.[20]

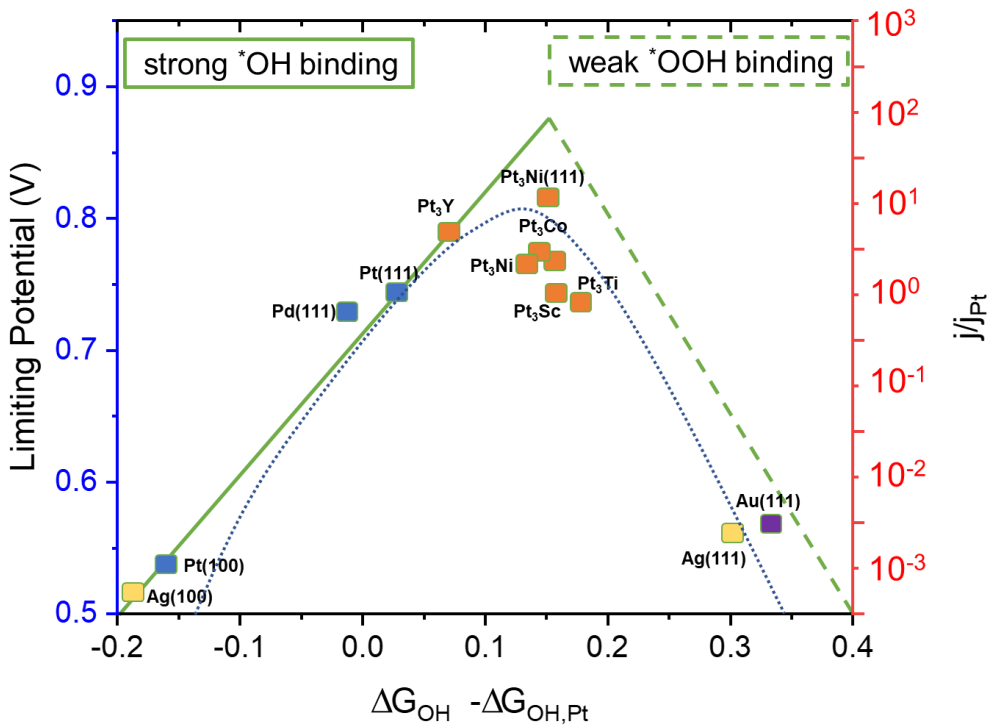

Figure 1.2 Kinetic volcano plot and limiting potential volcano plot based on computational modeling with some material used for the ORR.

The combination of a PGM with a non-precious metal has improved ORR performance by reducing the amount of PGM. In these Sabatier volcano plots, Pt alloys (Pt_3Y) with first-row transition metals are usually at the cuspid. Specifically, Pt alloyed with first-row transition metals are among the most active materials—the Fermi level of Pt 4d and 4f orbitals is lowered while Pt 5d orbital vacancies are increased—to promote Pt-O_2 interaction.[21] However, Pt establishes a challenge for mass-production FCs, and it is an expensive material. To use FC as daily drivers for automotive purposes and sustain all the industry demands, less expensive catalysts should be considered. To comply, researchers have adopted strategies by modifying the catalyst structure, morphology or incorporating less expensive foreign materials or metal oxides. Some of the approaches taken by several groups are: using Pt/C catalysts,[22]core-shell nanoparticles,[23–25] non-precious metals,[26,27] and nanowires[28–31]. The central importance is that these materials achieve high current densities and increase normalized mass activities for the ORR.[20]

More than a decade ago, Markovic *et al.* found that $Pt_3Ni(111)$ is 10 and 90 times more active for ORR than Pt(111) and Pt/C catalyst, respectively.[32] Improvements of PtNi catalysts are still under development. If Pt stays as the active material for ORR, researchers must minimize the amount of Pt used in their catalysts, but they need to maintain high activity, durability, and stability. Nanowires can meet these targets since they provide large surface areas and many active sites for the catalytic reaction while preventing: Ostwald ripening, aggregation and dissolution.[33,34] In addition, they are good conductors and can be used as templates for catalysts development.[35]

1.4. Monolayer Catalysts

The core-shell nanoparticle arrangement can also be implemented to obtain an active catalyst. Usually, the nanoparticle's core constitutes a non-noble metal, and the layer at the nanoparticle's surface is a noble metal. Implementing the monolayer (ML) concept has been proven to ease the optimal ultra-low loading of PGM core-shell nanoparticles without sacrificing performance.[36] The underpotential deposition (UPD) phenomenon has been used to obtain electrochemically ordered metal adlayers on a metallic substrate and then replace those metal adlayers with a more noble metal by electroless deposition—spontaneous galvanic displacement (SGD) process.[37] The use of Cu as the metal adlayer has been thoroughly explored by Adzic's group at Brookhaven National Laboratory (BNL).[38]

A turning approach is to incorporate abundant materials such as Cu catalysts as the actual substrate of the ML PGM nanoparticle—with ultra-low loading of atoms—to catalyze energy conversion reactions that could replace fossil fuel technologies.[39,40] For instance, this approach can help mitigate the economic, operational, and material abundance barriers that limit the proper commercialization of FCs.[18] The Pb electroless deposition method[41]—a self-terminating surfaces controlled process—has been implemented on Au, Cu, Pt and Ru disks.[42] The Pb e-less process leads to Pb being deposited on supports (in this case, a Cu catalyst) and then replacing the Pb with a more noble metal using the SGD process.

1.5. Operando X-ray absorption spectroscopy

The characterization of the materials is an essential step to improving and understanding energy conversion reactions. Specifically, X-ray absorption spectroscopy (XAS) experiments provide vital information regarding the electronic structure of the absorber atom. A common setup for XAS experiments is shown in **Figure 1.3.** The radiation commons from a synchrotron source and is tuned by a monochromator to select the specific energy of the sample. This radiation is passed along a series of detectors (I_0,I_T,I_{ref}). Between detectors I_0 and I_T we can collect data on transmission mode and then use the information obtained in detector I_T to acquire precise alignment of the results based on a reference sample (foil of the metal that's being analyzed). Transmission measurements tend to have better signal to noise ratio. However, sometimes the samples are not quite homogeneous or are diluted. This is when the fluorescent mode can be used by adding a detector located 90° from the sample.

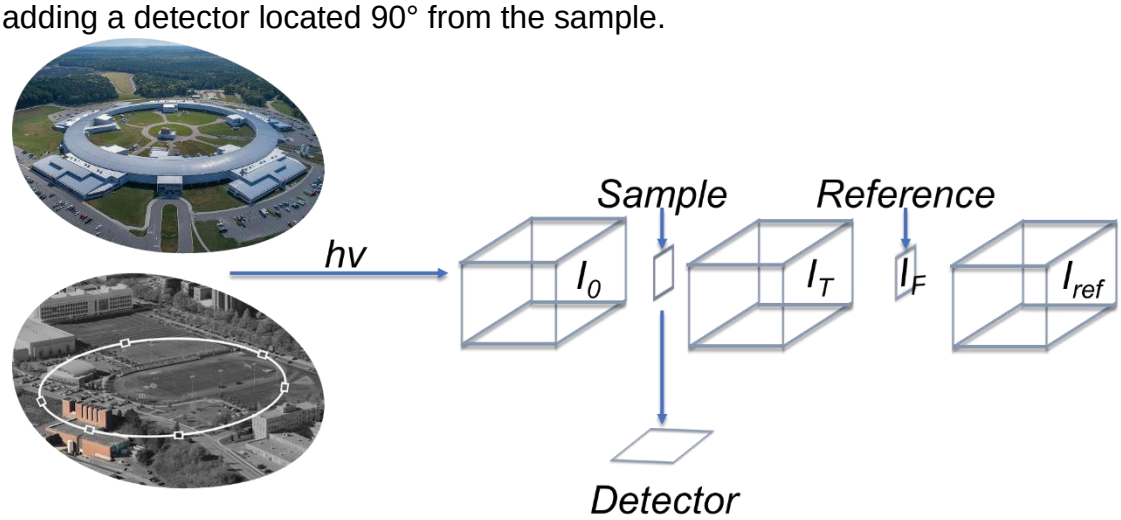

Figure 1.3 Schematic representation of a XAS setup based on a synchrotron source.

XAS spectrums could be divided into different regions as shown in **Figure 1.4**. The X-ray absorption fine structure (XAFS) acts as a sensitive probe of the material's electronic structure; we can gather information related to the oscillations of the absorption probability before and after the absorption edge.[43] If the incident beam hits an atom that does not have an inversion center, a forbidden transition (1s → 3d) is reflected as a pre-edge–this commonly happens to first-row transition metals.[44]

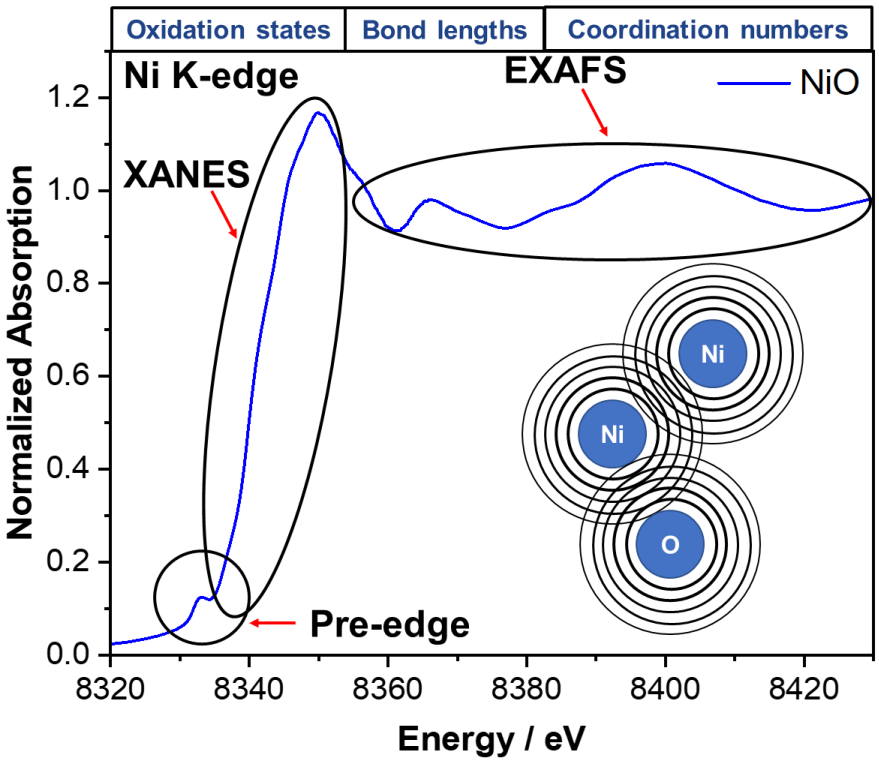

Figure 1.4 XAS spectrum of the Ni K-edge of an NiO standard with its photoelectron scattering process.

The X-ray absorption near edge structure (XANES) reveals characteristics of the absorber before and after the absorption edge translating to information about the oxidation states, local symmetry and chemical bonding.[45] The energy

oscillations above the XANES region stand for the extended X-ray absorption fine structure (EXAFS). EXAFS can be seen as an average of the constructive and destructive wave-like interactions between the absorber and its nearest neighbors—acting as a probe of the spatial arrangement of the nearest neighbors in the vicinity of the absorber.[46]

The ex-situ approach has been used to provide reaction intermediates and stepwise reaction kinetics.[47] However, there has been an increased urge to incorporate *in situ* and *operando* spectroscopical studies to reveal real-time information about specific electrocatalytic reactions. The *in situ* approach collects information on certain catalytic conditions (e.g., temperature, humidity, pressure) related to the catalytic reaction's factual circumstances. On the other hand, measurements under the same conditions as a catalytic reactor or a selected operating device are cataloged as *operando*.[48] *In situ*/*operando* methodologies have been incorporated into X-ray diffraction (XRD),[49] Raman spectroscopy,[50] Ultraviolet-visible spectroscopy (UV-vis)[51], Transmission electron spectroscopy (TEM)[52] and XAS[53].

The combination of electrochemistry and XAS provides real-time information on the catalytic behavior under an electrochemical environment. We can conclude that *in situ* and *operando* measurements act as powerful probes to reveal how materials catalyze specific electrocatalytic reactions under reaction conditions, the ORR. Considering the justifications above for FCs improvements, this thesis will focus on the research related to PGM catalysts alloyed with 1st-row transition metal for the catalysis of the ORR in an alkaline medium. The characterizations of these

materials will be centered on gaining real-time insights into the catalytic behavior for ORR under XAS electrochemical experiments.

1.6. References

(1) Banham, D.; Ye, S. Current Status and Future Development of Catalyst Materials and Catalyst Layers for Proton Exchange Membrane Fuel Cells: An Industrial Perspective. *ACS Energy Lett.* **2017**, *2*, 629–638.

(2) Chu, S.; Cui, Y.; Liu, N. The Path towards Sustainable Energy. *Nat. Mater.* **2016**, *16*, 16–22.

(3) Borup, R.; Krause, T.; Brouwer, J. Hydrogen Is Essential for Industry and Transportation Decarbonization. *Electrochem. Soc. Interface* **2021**, *30*, 79–83.

(4) Hydrogen Shot https://www.energy.gov/eere/fuelcells/hydrogen-shot. (accessed Dec 16, 2021).

(5) She, Z. W.; Kibsgaard, J.; Dickens, C. F.; Chorkendorff, I.; Nørskov, J. K.; Jaramillo, T. F. Combining Theory and Experiment in Electrocatalysis: Insights into Materials Design. *Science (80-.).* **2017**, *355*, eaad4998.

(6) Pivovar, B. S.; Ruth, M. F.; Myers, D. J.; Dinh, H. N. Hydrogen: Targeting $1/Kg in 1 Decade. *Electrochem. Soc. Interface* **2021**, *30*, 61–65.

(7) Edwards, P. P.; Kuznetsov, V. L.; David, W. I. F.; Brandon, N. P. Hydrogen and Fuel Cells: Towards a Sustainable Energy Future. *Energy Policy* **2008**, *36*, 4356–4362.

(8) Zhao, C.; Xu, G. L.; Yu, Z.; Zhang, L.; Hwang, I.; Mo, Y. X.; Ren, Y.; Cheng, L.; Sun, C. J.; Ren, Y.; Zuo, X.; Li, J. T.; Sun, S. G.; Amine, K.; Zhao, T. A High-Energy and Long-Cycling Lithium–Sulfur Pouch Cell via a Macroporous Catalytic Cathode with Double-End Binding Sites. *Nat. Nanotechnol.* **2020**, *16*, 166–173.

(9) Darling, R. M.; Meyers, J. P. Kinetic Model of Platinum Dissolution in PEMFCs. *J. Electrochem. Soc.* **2003**, *150*, A1523–A1527.

(10) Pham, C.; Britton, B.; Böhm, T.; Holdcroft, S.; Thiele, S. Doped, Defect-Enriched Carbon Nanotubes as an Efficient Oxygen Reduction Catalyst for Anion Exchange Membrane Fuel Cells. *Adv. Mater. Interfaces* **2018**, *5*, 1800184.

(11) Yang, Y.; Peltier, C. R.; Zeng, R.; Schimmenti, R.; Li, Q.; Huang, X.; Yan, Z.; Potsi, G.; Selhorst, R.; Lu, X.; Xu, W.; Tader, M.; Soudackov, A. V.; Zhang, H.; Krumov, M.; Murray, E.; Xu, P.; Hitt, J.; Xu, L.; Ko, H. Y.; Ernst, B. G.; Bundschu, C.; Luo, A.; Markovich, D.; Hu, M.; He, C.; Wang, H.; Fang, J.; Distasio, R. A.; Kourkoutis, L. F.; Singer, A.; Noonan, K. J. T.; Xiao, L.;

Zhuang, L.; Pivovar, B. S.; Zelenay, P.; Herrero, E.; Feliu, J. M.; Suntivich, J.; Giannelis, E. P.; Hammes-Schiffer, S.; Arias, T.; Mavrikakis, M.; Mallouk, T. E.; Brock, J. D.; Muller, D. A.; Disalvo, F. J.; Coates, G. W.; Abruña, H. D. Electrocatalysis in Alkaline Media and Alkaline Membrane-Based Energy Technologies. *Chem. Rev.* **2022**, *122*, 6117–6321.

(12) Song, C.; Zhang, J. Electrocatalytic Oxygen Reduction Reaction. In *PEM fuel cell electrocatalysts and catalyst layers*; Springer: London, 2008; pp 89–134.

(13) Dekel, D. R. Review of Cell Performance in Anion Exchange Membrane Fuel Cells. *J. Power Sources* **2018**, *375*, 158–169.

(14) Winter, M.; Brodd, R. J. What Are Batteries, Fuel Cells, and Supercapacitors? *Chem. Rev.* **2004**, *104*, 4245–4269.

(15) Cano, Z. P.; Banham, D.; Ye, S.; Hintennach, A.; Lu, J.; Fowler, M.; Chen, Z. Batteries and Fuel Cells for Emerging Electric Vehicle Markets. *Nat. Energy* **2018**, *3*, 279–289.

(16) Wang, Y.; Chu, F.; Zeng, J.; Wang, Q.; Naren, T.; Li, Y.; Cheng, Y.; Lei, Y.; Wu, F. Single Atom Catalysts for Fuel Cells and Rechargeable Batteries: Principles, Advances, and Opportunities. *ACS Nano* **2021**, *15*, 210–239.

(17) Ren, X.; Lv, Q.; Liu, L.; Liu, B.; Wang, Y.; Liu, A.; Wu, G. Current Progress of Pt and Pt-Based Electrocatalysts Used for Fuel Cells. *Sustain. Energy Fuels* **2020**, *4*, 15–30.

(18) Sasaki, K.; Kuttiyiel, K. A.; Adzic, R. R. Designing High Performance Pt Monolayer Core–Shell Electrocatalysts for Fuel Cells. *Curr. Opin. Electrochem.* **2020**, *21*, 368–375.

(19) Nørskov, J. K.; Rossmeisl, J.; Logadottir, A.; Lindqvist, L.; Kitchin, J. R.; Bligaard, T.; Jónsson, H. Origin of the Overpotential for Oxygen Reduction at a Fuel-Cell Cathode. *J. Phys. Chem. B* **2004**, *108*, 17886–17892.

(20) Kulkarni, A.; Siahrostami, S.; Patel, A.; Nørskov, J. K. Understanding Catalytic Activity Trends in the Oxygen Reduction Reaction. *Chem. Rev.* **2018**, *118*, 2302–2312.

(21) Toda, T.; Igarashi, H.; Uchida, H.; Watanabe, M. Enhancement of the Electroreduction of Oxygen on Pt Alloys with Fe, Ni, and Co. *J. Electrochem. Soc.* **1999**, *146*, 3750–3756.

(22) Demarconnay, L.; Coutanceau, C.; Léger, J.-M. Electroreduction of Dioxygen (ORR) in Alkaline Medium on Ag/C and Pt/C Nanostructured Catalysts—Effect of the Presence of Methanol. *Electrochim. Acta* **2004**, *49*, 4513–4521.

(23) Bu, L.; Zhang, N.; Guo, S.; Zhang, X.; Li, J.; Yao, J.; Wu, T.; Lu, G.; Ma, J.-Y.; Su, D. Biaxially Strained PtPb/Pt Core/Shell Nanoplate Boosts Oxygen Reduction Catalysis. *Science (80-.).* **2016**, *354*, 1410–1414.

(24) Wang, D.; Xin, H. L.; Hovden, R.; Wang, H.; Yu, Y.; Muller, D. A.; Disalvo, F. J.; Abruña, H. D. Structurally Ordered Intermetallic Platinum-Cobalt Core-Shell Nanoparticles with Enhanced Activity and Stability as Oxygen Reduction Electrocatalysts. *Nat. Mater.* **2013**, *12*, 81–87.

(25) Shen, L.-L.; Zhang, G.-R.; Miao, S.; Liu, J.; Xu, B.-Q. Core–Shell Nanostructured Au@ Ni m Pt2 Electrocatalysts with Enhanced Activity and Durability for Oxygen Reduction Reaction. *ACS Catal.* **2016**, *6*, 1680–1690.

(26) Ge, X.; Sumboja, A.; Wuu, D.; An, T.; Li, B.; Goh, F. W. T.; Hor, T. S. A.; Zong, Y.; Liu, Z. Oxygen Reduction in Alkaline Media: From Mechanisms to Recent Advances of Catalysts. *Acs Catal.* **2015**, *5*, 4643–4667.

(27) Liang, Y.; Li, Y.; Wang, H.; Zhou, J.; Wang, J.; Regier, T.; Dai, H. Co 3 O 4 Nanocrystals on Graphene as a Synergistic Catalyst for Oxygen Reduction Reaction. *Nat. Mater.* **2011**, *10*, 780–786.

(28) Yin, H.; Zhao, S.; Zhao, K.; Muqsit, A.; Tang, H.; Chang, L.; Zhao, H.; Gao, Y.; Tang, Z. Ultrathin Platinum Nanowires Grown on Single-Layered Nickel Hydroxide with High Hydrogen Evolution Activity. *Nat. Commun.* **2015**, *6*, 1–8.

(29) Shulda, S.; Weker, J. N.; Ngo, C.; Alia, S. M.; Mauger, S. A.; Neyerlin, K. C.; Pivovar, B. S.; Pylypenko, S. 2D and 3D Characterization of PtNi Nanowire Electrode Composition and Structure. *ACS Appl. Nano Mater.* **2019**, *2*, 525–534.

(30) Kim, M. J.; Cruz, M. A.; Yang, F.; Wiley, B. J. Accelerating Electrochemistry with Metal Nanowires. *Curr. Opin. Electrochem.* **2019**, *16*, 19–27.

(31) Wang, Z.; Cao, X.; Peng, D.; Lu, Y.; Zhang, B.; Huang, K.; Zhang, T.; Wu, J.; Huang, Y. Strained Ultralong Silver Nanowires for Enhanced Electrocatalytic Oxygen Reduction Reaction in Alkaline Medium. *J. Phys. Chem. Lett.* **2021**, 2029–2035.

(32) Stamenkovic, V. R.; Fowler, B.; Mun, B. S.; Wang, G.; Ross, P. N.; Lucas, C. A.; Markovic, N. M. Improved Oxygen Reduction Activity on Pt3Ni(111) via Increased Surface Site Availability. *Science (80-.).* **2007**, *315*, 493–497.

(33) Chen, Z.; Waje, M.; Li, W.; Yan, Y. Supportless Pt and PtPd Nanotubes as Electrocatalysts for Oxygen-reduction Reactions. *Angew. Chemie Int. Ed.* **2007**, *46*, 4060–4063.

(34) Mao, J.; Chen, W.; He, D.; Wan, J.; Pei, J.; Dong, J.; Wang, Y.; An, P.; Jin, Z.; Xing, W.; Tang, H.; Zhuang, Z.; Liang, X.; Huang, Y.; Zhou, G.; Wang, L.; Wang, D.; Li, Y. Design of Ultrathin Pt-Mo-Ni Nanowire Catalysts for Ethanol Electrooxidation. *Sci. Adv.* **2017**, *3*, 1–10.

(35) Shao, Q.; Lu, K.; Huang, X. Platinum Group Nanowires for Efficient Electrocatalysis. *Small Methods* **2019**, *3*, 1800545.

(36) Adzic, R. R.; Zhang, A. J.; Sasaki, A. K.; Vukmirovic, A. M. B.; Shao, A. M.; Wang, A. J. X.; Nilekar, A. A. U.; Mavrikakis, A. M.; Valerio, A. J. A.; Uribe, A. F. Platinum Monolayer Fuel Cell Electrocatalysts. *Top. Catal.* **2007**, *46*, 249–262.

(37) Brankovic, S. R.; Wang, J. X.; Adžić, R. R. Metal Monolayer Deposition by Replacement of Metal Adlayers on Electrode Surfaces. *Surf. Sci.* **2001**, *474*, L173–L179.

(38) Vukmirovic, M. B.; Bliznakov, S. T.; Sasaki, K.; Wang, J. X.; Adzic, R. R. Electrodeposition of Metals in Catalyst Synthesis: The Case of Platinum Monolayer Electrocatalysts. *Electrochem. Soc. Interface* **2011**, *20*, 33–40.

(39) Adzic, R. R.; Zhang, J.; Sasaki, K.; Vukmirovic, M. B.; Shao, M.; Wang, J. X.; Nilekar, A. U.; Mavrikakis, M.; Valerio, J. A.; Uribe, F. Platinum Monolayer Fuel Cell Electrocatalysts. *Top. Catal.* **2007**, *46*, 249–262.

(40) Zhang, J.; Vukmirovic, M. B.; Xu, Y.; Mavrikakis, M.; Adzic, R. R.; Xu, Y.; Mavrikakis, M.; Zhang, J.; Vukmirovic, M. B.; Adzic, R. R. Controlling the Catalytic Activity of Platinum-Monolayer Electrocatalysts for Oxygen Reduction with Different Substrates**. *Angew. Chem. Int. Ed* **2005**, *44*, 2132–2135.

(41) Wu, D.; Solanki, D. J.; Ramirez, J. L.; Yang, W.; Joi, A.; Dordi, Y.; Dole, N.; Brankovic, S. R. Electroless Deposition of Pb Monolayer : A New Process and Application to Surface Selective Atomic Layer Deposition. **2018**, *38*, 11384–11394.

(42) Ahmadi, K.; Dole, N.; Wu, D.; Salavati-Fard, T.; C. Grabow, L.; Carlos Robles Hernandez, F.; R. Brankovic, S. Electroless Pb Monolayer Deposition—Prelude for Further Advances in Catalyst Monolayer Synthesis via Surface Limited Redox Replacement Reaction. *ACS Catal.* **2021**, *11*, 4650–4659.

(43) Timoshenko, J.; Roldan Cuenya, B. In Situ/Operando Electrocatalyst Characterization by X-Ray Absorption Spectroscopy. *Chem. Rev.* **2021**, *121*, 882–961.

(44) Calvin, S. *XAFS for Everyone*; CRC Press: Boca Raton, 2013.

(45) Yano, J.; Yachandra, V. K. X-Ray Absorption Spectroscopy. *Photosynth. Res.* **2009**, *102*, 241–254.

(46) Rehr, J. J.; Albers, R. C. Theoretical Approaches to X-Ray Absorption Fine Structure. *Rev. Mod. Phys.* **2000**, *72*, 621–654.

(47) Zhu, Y.; Wang, J.; Chu, H.; Chu, Y. C.; Chen, H. M. In Situ/ Operando Studies for Designing Next-Generation Electrocatalysts. *ACS Energy Lett.* **2020**, *5*, 1281–1291.

(48) Yang, Y.; Xiong, Y.; Zeng, R.; Lu, X.; Krumov, M.; Huang, X.; Xu, W.; Wang, H.; Disalvo, F. J.; Brock, J. D.; Muller, D. A.; Abrunã, H. D. Operando

Methods in Electrocatalysis. *ACS Catal.* **2021**, *11*, 1136–1178.

(49) Kulisch, J.; Sommer, H.; Brezesinski, T.; Janek, J. Simple Cathode Design for Li–S Batteries: Cell Performance and Mechanistic Insights by in Operando X-Ray Diffraction. *Phys. Chem. Chem. Phys.* **2014**, *16*, 18765–18771.

(50) Shi, Y.; Du, W.; Zhou, W.; Wang, C.; Lu, S.; Lu, S.; Zhang, B. Unveiling the Promotion of Surface-Adsorbed Chalcogenate on the Electrocatalytic Oxygen Evolution Reaction. *Angew. Chemie Int. Ed.* **2020**, *59*, 22470–22474.

(51) Zhao, C.; Xu, G.-L.; Yu, Z.; Zhang, L.; Hwang, I.; Mo, Y.-X.; Ren, Y.; Cheng, L.; Sun, C.-J.; Ren, Y. A High-Energy and Long-Cycling Lithium–Sulfur Pouch Cell via a Macroporous Catalytic Cathode with Double-End Binding Sites. *Nat. Nanotechnol.* **2021**, *16*, 166–173.

(52) Yang, Y.; Shao, Y.-T.; DiSalvo, F. J.; Muller, D. A.; Abruña, H. D. Metal Monolayers on Command: Underpotential Deposition at Nanocrystal Surfaces: A Quantitative Operando Electrochemical Transmission Electron Microscopy Study. *ACS Energy Lett.* **2022**, *19*, 1292–1297.

(53) Huang, H.; Russell, A. E. Approaches to Achieve Surface Sensitivity in the in Situ XAS of Electrocatalysts. *Curr. Opin. Electrochem.* **2021**, *27*, 100681.

Chapter 2. **Significance and statement of the problem**

2.1. Hypothesis

The research held in this thesis encompasses the study of emerging nanomaterials as cathode catalysts—for the ORR in AEMFCs. Our **hypothesis** suggests that the incorporation of lower mass loadings of Pt or Pd precursor on Ni, Co and Cu catalysts will enhance the performance of the ORR in an alkaline medium. This will be proved firstly by using hydrothermal synthesis and SGD to provide a route for core-shell structured PtNi-nanowires (NWs). Secondly, with the electrodeposition of Ni, Co and Cu on Carbon Vulcan XC-72R (V) using the Rotating disk slurry electrodeposition (RoDSE) method followed by SGD to provide highly dispersed PtNi/V, PtCo/V and PtCu/V nanoparticles (NPs). Lastly, with the Pb electroless (e-less) deposition method to provide Pd monolayer catalysts using Cu (100) NPs as substrates.

2.2. Research goal and specific aims

The **main goal** of this thesis is to obtain highly dispersed nano-catalysts with low loadings of Platinum group metals (PGM), Pt and Pd, alloyed with first-row transition metals (Ni, Co and Cu) supported on V. These catalysts will be tested for their mass activities, current densities, and durability towards the ORR in an alkaline medium. Our **specific aims are:**

1. To obtain low PGM loading nano-catalysts for the ORR in an alkaline medium.
2. To characterize the chemical and physical properties of the catalysts.

3. To successfully implement the RoDSE methodology to Ni, Co and Cu catalysts.
4. To synthesize active Pd monolayer catalysts for the ORR with the Pb e-less deposition method.
5. To study the electronic structure of the catalysts under ORR in alkaline media using *in situ* electrochemical XAS.

2.3. Techniques

To fulfill our aims, we will mainly implement the use of electrochemical techniques, specifically cyclic voltammetry (CV), linear sweep voltammetry (LSV), chronoamperometry (CA) and impedance spectroscopy (IES). The materials' crystalline structure will be evaluated with powder X-ray diffraction (PXRD). The size, structure, and chemical composition with transmission electron microscopy (TEM), Scanning transmission electron microscopy (STEM), Energy dispersive spectroscopy (EDS) and Scanning electron microscopy (SEM). The chemical composition will also be obtained with inductively coupled plasma optical emission spectroscopy (ICS-OES), the surface composition with X-ray photoelectron spectroscopy (XPS), and the electronic structure of the catalyst with X-ray absorption (XAS)—X-ray absorption near edge structure (XANES) and Extended X-ray absorption fine structure (EXAFS)—and under electrochemical reactions (ORR) with *in situ* electrochemical XAS.

Chapter 3. **Analytical and electrochemical experimental protocols**

3.1. Reference electrode calibration

3.1.1. Electrode calibration using a millivoltmeter.

To compare our experiments with the most common results from ORR publications, we needed to convert the reference electrode (RE) electrode potential used in the experiments to the RHE scale. This is because most of ORR articles are in an acidic medium, where the reversible hydrogen electrode (RHE) is commonly used because of its stability at low pH. However, the RHE electrode is not recommended for use in alkaline solutions because the equilibrium of Pt/H_2 is disturbed by OH^-. In most of our experiments, we decided to use Ag/AgCl because it is reliable, easy to build, simple to maintain and the potential may be monitored. Nevertheless, the electrode's inner solution (KCl) is constantly changed and the potential should be monitored before each experiment. The HgO/Hg reference electrode was also used for alkaline ORR experiments considering its stability at high pH values.

The simplest way that we found to calibrate our electrode was by using a commercial RHE—Hydroflex™ RE from edaq. This calibration was done in 25 mL of 0.5 M H_2SO_4 using a millivoltmeter. The RE that needs to be calibrated is measured against the commercial RHE. The potential obtained from the millivoltmeter was used in the Nernst **equation 3.1** as follows.

$$\mathrm{E°(RHE)} = \mathrm{E(Ag/AgCl)}_{\mathrm{exp}} + \frac{pH((\ln(10)RT)}{nF} + \mathrm{E(Ag/AgCl)}_{\mathrm{calculated}} \qquad \textbf{Eq. 3.1}$$

Here, $E^{\circ}(RHE)$ is the RHE value that is obtained, $E(Ag/AgCl)_{exp}$ is the potential value from the experiments using the Ag/AgCl electrode and the *pH* must be considered because RHE is a pH-dependent reference. In this case, the pH was 13 because we used 0.1 M KOH, *R* is the gas constant with a value of 8.3145 J mol^{-1} K^{-1}, *F* is the Faraday constant with a value of 96,485 C/mol, *n* is the number of electrons transferred in the electrochemical reaction equal to 1 for ORR and $E(Ag/AgCl)_{calculated}$ is the value obtained from the calibration using the commercial RHE and the RE used in 0.5 M H_2SO_4 before each experiment.

The following derivation of the Nernst equation is done to obtain the final value of the RE electrode:

$$E°(RHE) = 0.000 - pH(0.0592)$$

With a solution of 0.5 M H_2SO_4:

$$E°(RHE) = 0.000 - (-log(0.5))(0.0592))$$

$$E°(RHE) = 0.000 - 0.30(0.0592)$$

$$E°(RHE) = -0.018\,V$$

This potential (0.018 V) was subtracted from the potential value from the multimeter when connecting the RHE and Ag/AgCl electrode in 0.5 M H_2SO_4 (**Figure 3.1**).

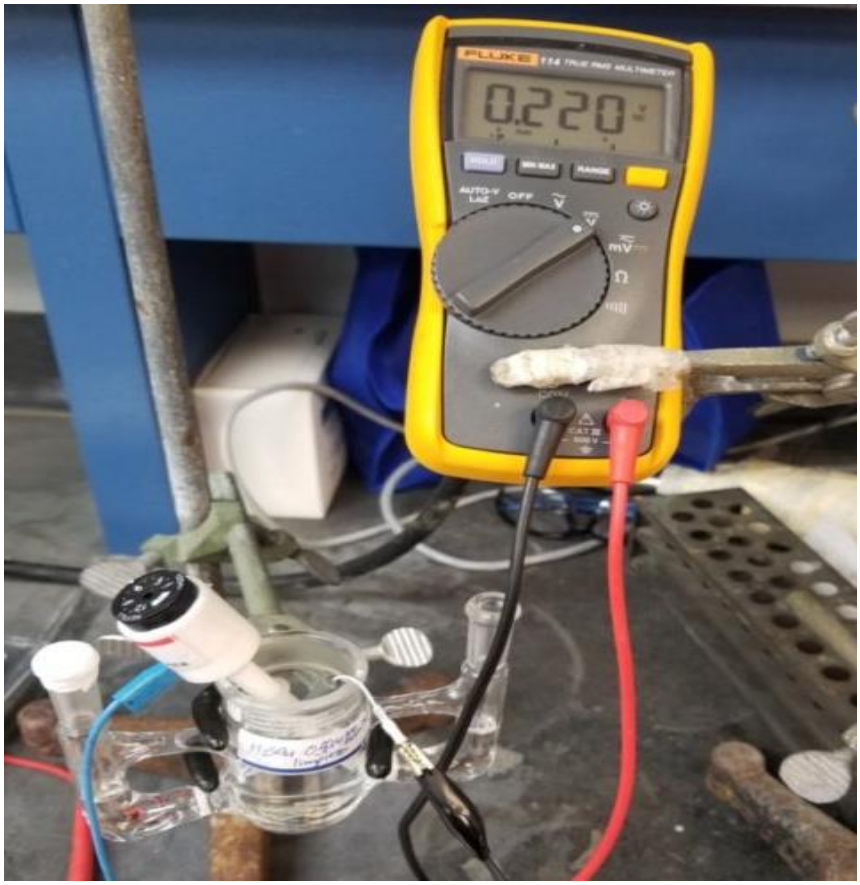

Figure 3.1 Multimeter value for reference electrodes difference in 0.5 M H_2SO_4.

$$E(Ag/AgCl)calculated = 0.220\,V - 0.018\,V$$

$$E(Ag/AgCl)calculated = 0.202\,V$$

This value is close to the actual reported value of Ag/AgCl sat. KCl electrode (0.197 V) suggesting a reliable and quantitative way of calibrating an Ag/AgCl reference electrode. Now the preferred potential window for the ORR reaction can be selected considering the RE potential from the calibration. The following derivation of the Nernst equation shows this procedure:

F= 96,485 C/mol

R=8.3145 J mol^{-1} K^{-1}

$$\mathrm{E°(RHE)} = \mathrm{E(Ag/AgCl)_{exp}} + \frac{pH((\ln(10)\,RT)}{nF} + \mathrm{E(Ag/AgCl)_{calculated}}$$

$$\mathrm{E°(RHE)} = \mathrm{E(Ag/AgCl)_{exp}} + \frac{pH((\ln(10)\,(8.3145\,J\,mol^{-1}K^{-1})(298.15\,K)}{(1)(96485\frac{C}{mol})}$$

$$+ \mathrm{E(Ag/AgCl)_{calculated}}$$

$$\mathrm{E°(RHE)} = \mathrm{E(Ag/AgCl)_{exp}} + 13(0.05916\,V) + \mathrm{E(0.220\,V)_{calculated}}$$

$$\mathrm{E°(RHE)} = \mathrm{E(Ag/AgCl)_{exp}} + 0.7691\ \mathrm{V} + 0.220\ \mathrm{V}$$

$$\mathrm{E°(RHE)} = \mathrm{E}\left(\frac{\mathrm{Ag}}{\mathrm{AgCl}}\right)_{\mathrm{exp}} + 0.9891\ \mathrm{V}$$

E°(RHE) = -0.90 V + 0.9946 V or E°(RHE) = 0.20 V + 0.9946 V

E°(RHE) = 0.10 V and 1.20 V vs RHE, this is the potential window for ORR

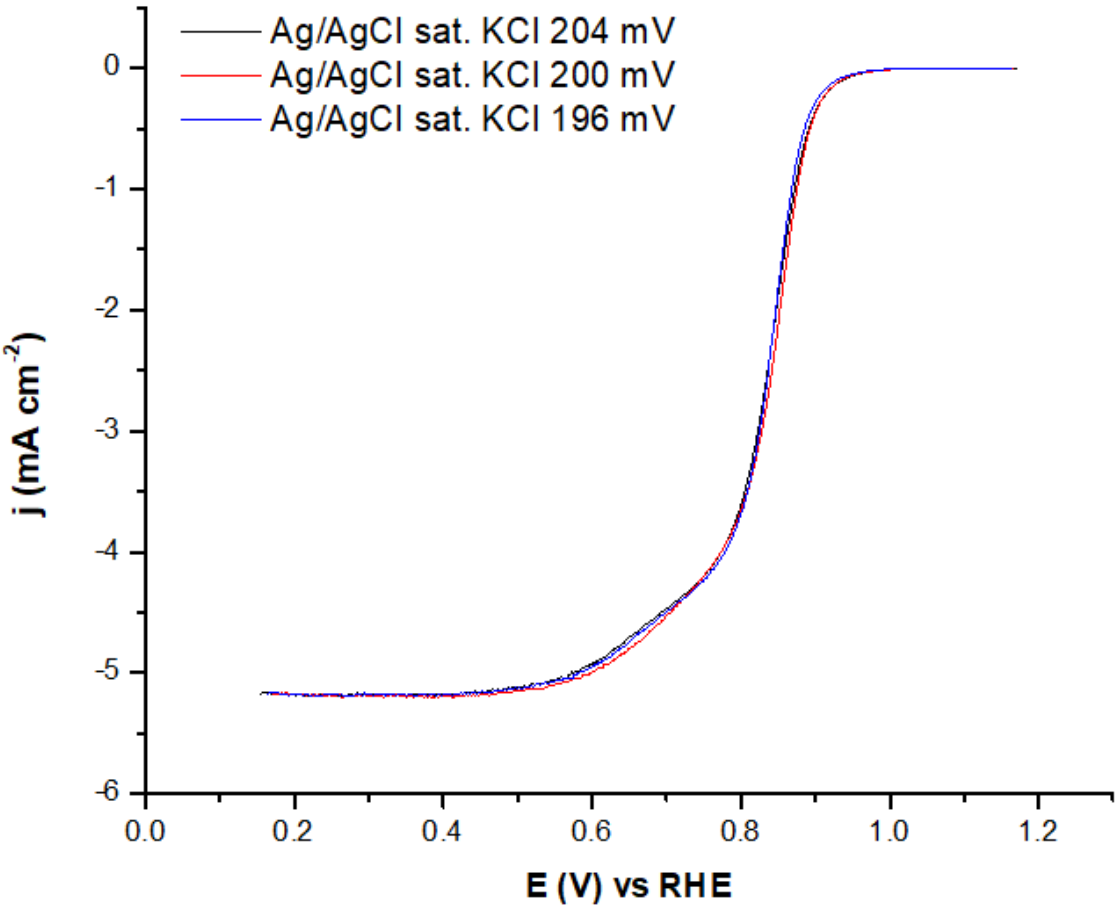

Figure 3.2 O_2 polarization curves for PtNi-NWs in 0.1 M KOH at 10 mV/s using different Ag/AgCl reference electrodes after the calibration. The solution was purged with oxygen for 15 minutes.

The calibration method was also proved using LSVs of the ORR. In **Figure 3.2** we demonstrate that three different electrodes with different potential differences with the RHE electrode are nearly at the same potential scale after the potential value conversion using the millivoltmeter calibration approach.

3.1.2. OCP

The open circuit potential (OCP) mode of a potentiostat can also be used to calibrate the RE potential value. A known potential of a calibrated reference electrode can be used as described in the previous section. However, the RHE electrode electrochemical reaction can be recreated in an electrochemical cell. Here, a Pt wire or a Pt mesh with high surface area is immersed in pure H_2 saturated 0.1 M $HClO_4$ solution. This Pt wire/mesh is now an RHE with a redox potential value of 0 V vs. RHE considering the H_2 redox reaction **equation 3**, which can be used to generate an OCP transient that monitors the actual RE potential to be calculate/calibrate.

$$2H^+ + 2e^- \leftrightarrow H_2(g) \qquad \textbf{Eq. 3}$$

The RHE simulated electrode is connected to the working and counter electrode cables of the potentiostat, and the RE cable is connected to the RE that we want to calibrate. The OCP transient for ca. 30 min is left until it stabilized while H_2 is purged in the solution, see **Figure 3.3**.

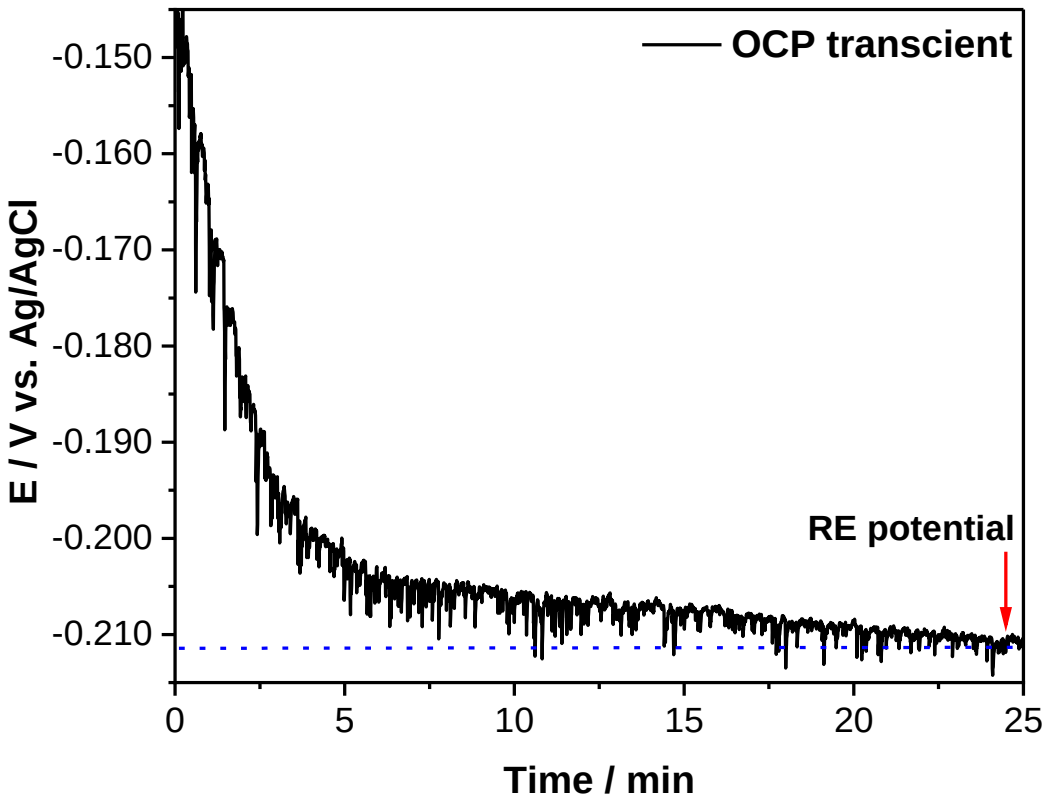

Figure 3.3 OCP transient calibration for an Ag/AgCl sat. KCl reference electrode versus the labmade RHE.

3.1.3. LSV zero net charge potential

For the LSV approach, a similar electrochemical setup was used as in section 3.1.2. However, an additional Pt wire/mesh was included to have a three-electrode setup and be able to do LSV experiments. The two Pt electrodes counted as a working electrode (WE) and a counter electrode (CE) simulating two RHE electrodes. Since they supposed to give the same potential value, in this case 0 V vs RHE, when we include a RE to the electrochemical setup the potential value at the zero current intercept is equal to the potential value of the RE.[1] These zero net

current values were extrapolated from the LSV plot as shown in **Figure 3.4**. The LSV experiments were performed using a scan rate of 1 mV/s.

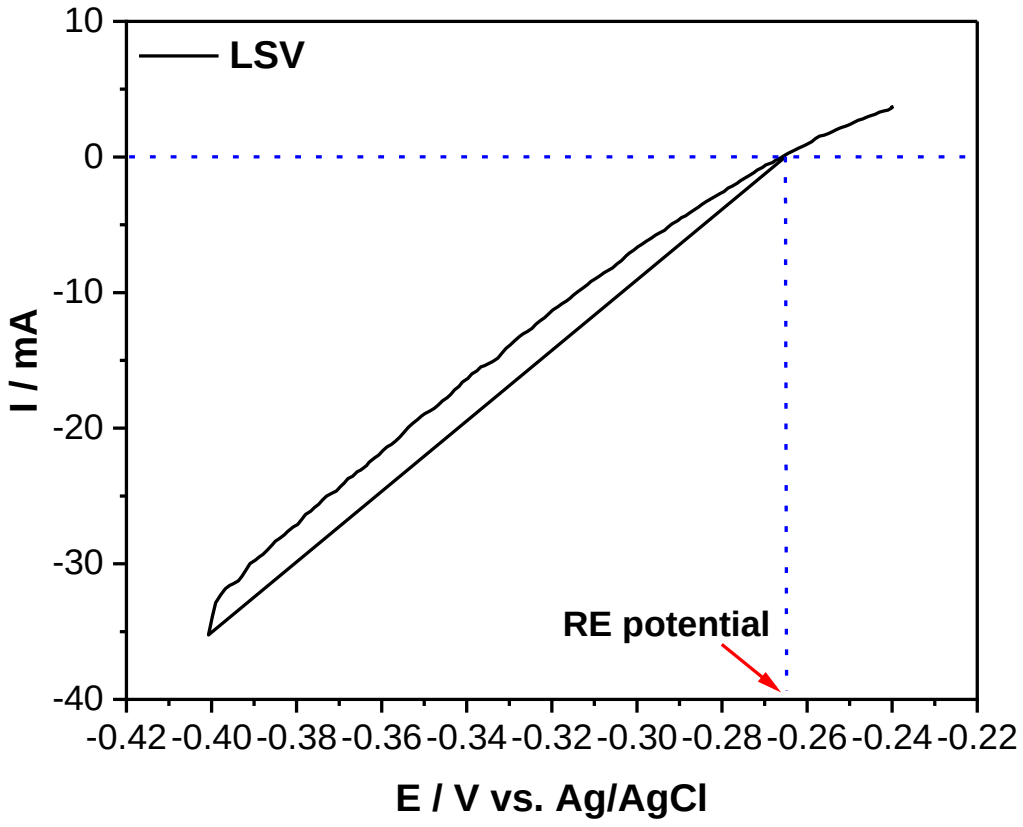

Figure 3.4 LSV plot at 1 mV/s for the calibration of an Ag/AgCl sat. KCl reference electrode versus RHE.

3.2. Temperature control electrochemical experiments

The first ORR experiments that we were doing at our laboratory in UPR-RP were not giving consistent results. After recognizing that the temperature at the laboratory was colder than 25°C and even colder after purging the solutions with nitrogen gas before the electrochemical experiments with temperatures reaching 19°C, we decided that we needed to design our experiments with a temperature control approach. This is because most of the equations used for our experiments assume that the system's temperature is 25°C. To control these temperature changes, we decided to incorporate a temperature control system used in conjunction with an electrochemical jacked cell **Figure 3.5.** The temperature control cell was set at (25.0 ±0.1) ºC using a Nestlab RTE-221 chiller and left for 10 minutes with the aqueous solution (0.1 M KOH) while its temperature reached 25.0 ºC. After this, we performed our experiments.

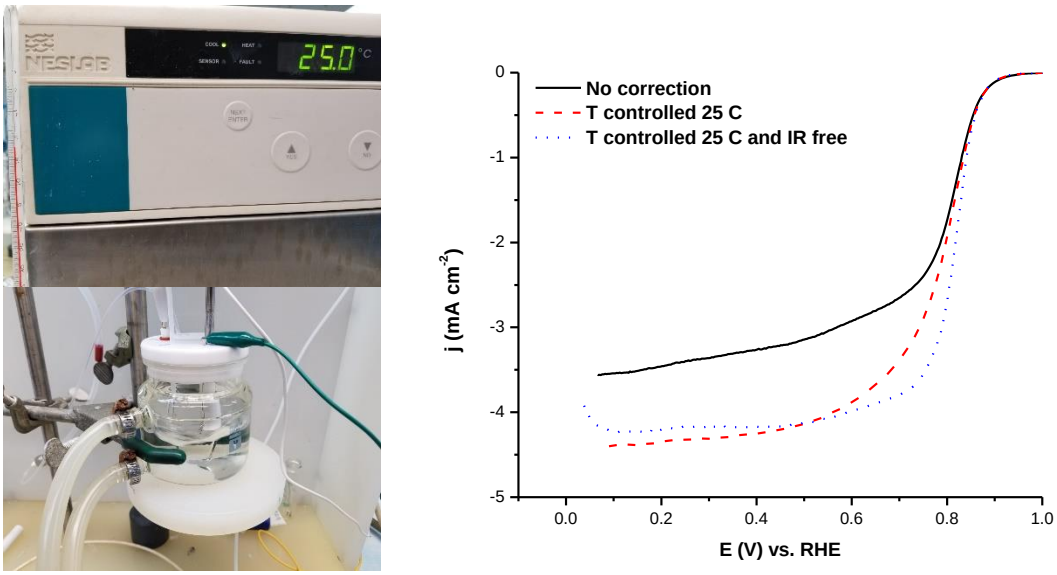

Figure 3.5 PtNiNWs O_2 polarization curves with temperature-controlled (25.00 ± 0.01) °C and correction by IR in KOH 0.1M at 5 mV/s and 1600 rpm.

3.3. Electrochemical surface area calculations

3.3.1. Platinum

The Pt catalyst electrochemical currents were normalized using the electrochemical surface area (ECSA) of the desorption peaks associated with H_2 in the Pt voltammograms region **Figure 3.6**. For Pt polycrystalline samples, a charge density of 210 μC/cm^2 considering a face-centered cubic structure (fcc) and the 100, 110 and 111 facets. The desorption region was integrated with Origin program, and the active surface area for Pt was calculated according to **Equation 3.3**

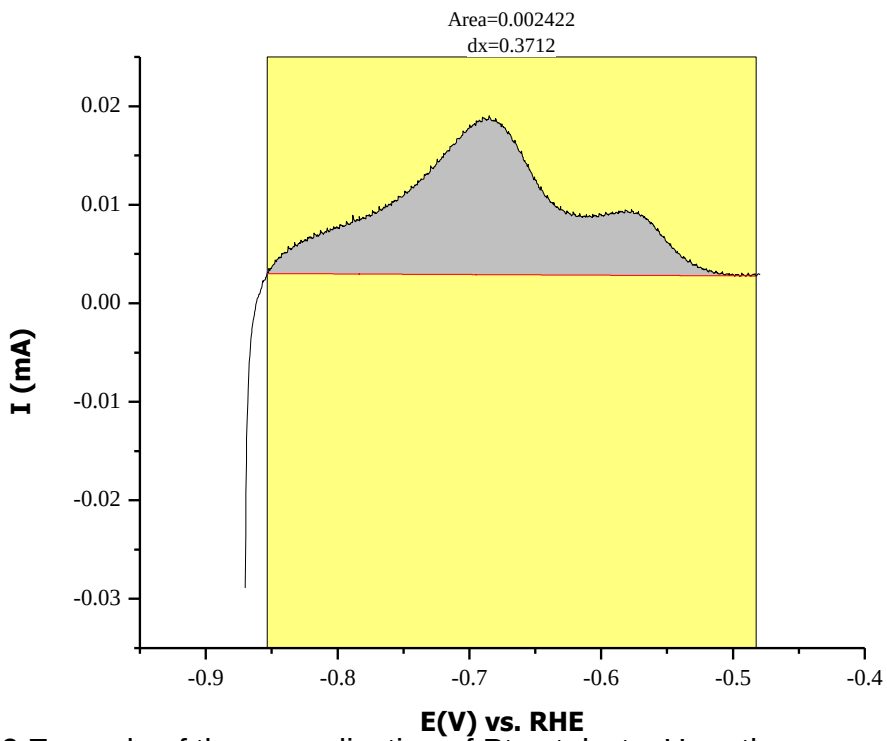

Figure 3.6 Example of the normalization of Pt catalysts. Here the area was calculated with the Origin program integrating the grey space of the graph.

$$ECSA\ (cm^2) = \frac{Integrated\ value(mA{\cdot}V)\ x\ 1000}{Charge\ of\ Pt\ (\mu C{\cdot}cm^{-2})\ x\ scan\ rate\ (V{\cdot}s^{-1})} \qquad \textbf{Eq. 3.3}$$

3.3.2. Palladium

For the Pd catalysts, the PdO oxidation peak was used as the peak reference to obtain the active surface area of Pd. A charge density of 420 μC/cm^2 is related to the reduction of a PdO monolayer on a Pd surface cathodic sweep **equation 3.4**.[2,3]

$$Pd - O + H_2O + 2e^- \leftrightarrow Pd + 2OH^- \qquad \textbf{Eq. 3.4}$$

The charge of the PdO peak was obtained using EC-Lab software and ECSA was calculated using **equation 3.5**.

$$ECSA\ (cm^2) = \frac{PdO\ peak\ charge(\mu C)}{Charge\ of\ PdO\ monolayer\ (\mu C \cdot cm^{-2})} \qquad \textbf{Eq. 3.5}$$

3.3.3. Gold

For the gold catalyst, the AuO monolayer was taken as a reference to calculate the ECSA of the Au catalysts. A charge density value of 390 μC/cm^2 is attributed to the AuO monolayer.[4] **Equation 3.3** was used to obtain the ECSA with the AuO peak charge and theoretical AuO charge density.

3.3.4. Copper

An oxide monolayer was also used to obtain the ECSA for the Cu catalysts. The Cu_2O peak charge from **Figure 3.1**. was calculated with the EC-Lab software. A charge density value of 352 μC/cm^2 is attributed to Cu_2O monolayer.[5] The ECSA of the copper catalyst was also calculated using **Equation 3.3** but using the respective values for Cu_2O charge and Cu_2O charge density factor.

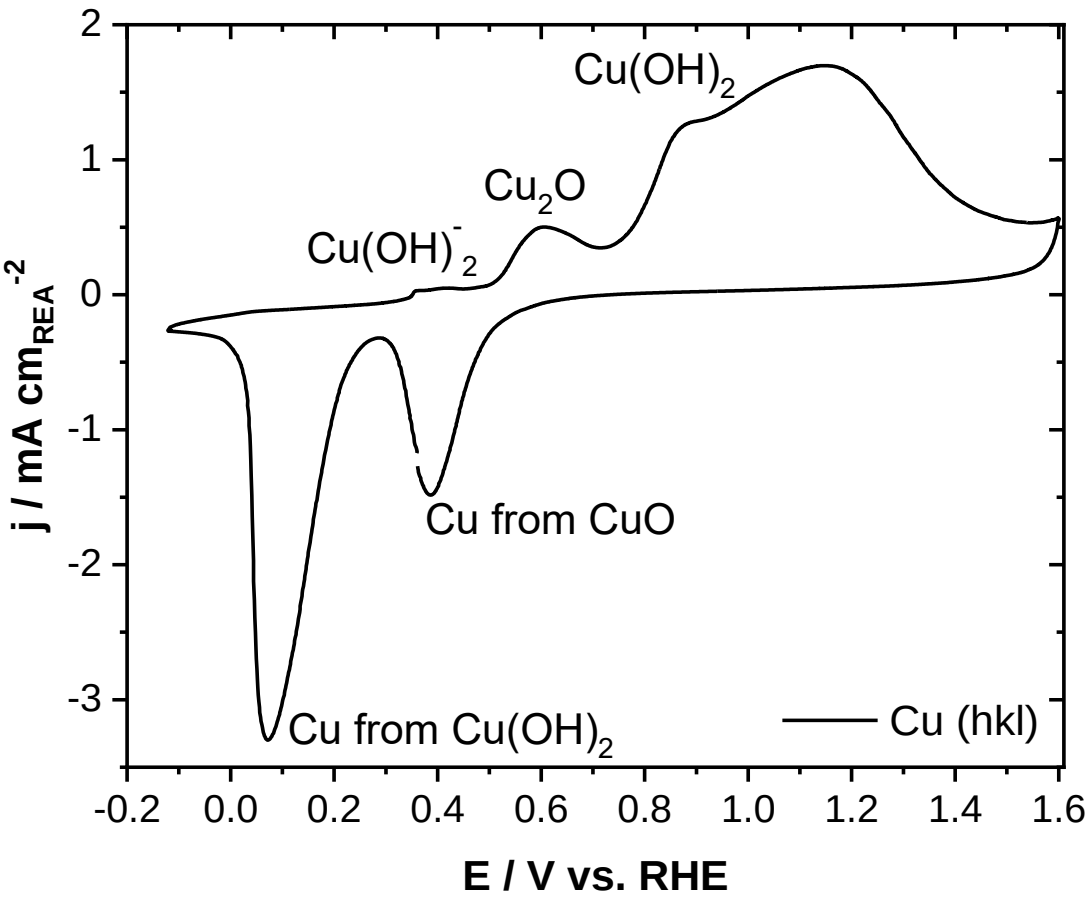

Figure 3.7 CV of bulk copper in Ar saturated 0.1 M KOH at 20 mV/s.

3.4. Electrochemical *in situ* XAS

We first started with preparing the electrochemical setup using a similar procedure to the one explained earlier with three electrodes and an electrochemical cell. The electrochemical setup consisted of an Ag/AgCl reference electrode, a platinum counter electrode, and a catalyst modified carbon cloth (190 μm thickness and ca. 10 mm x 100 mm the geometric area) working electrode. The carbon cloth electrode was obtained from the Fuel Cell Store (AvCarb MGL 190). The experiments were done with a previously published electrochemical *in situ* cell from Sasaki et al. see **Figure 3.8**.[33] We first sonicated for 0.1 M KOH for 1 hr minimum to ensure no interferences of bubbles with the XAS measurements.

The carbon cloth electrode was modified by preparing a similar catalyst ink solution mentioned earlier. This solution was made with 1 mg of the catalyst per 1 mL of stock solution (2:1:1:0.10 volume ratio of ethanol, pure water, isopropanol, and 5 µL of 5% of Nafion in alcohol, respectively). The ink solution was sonicated for 30 minutes and 200 µL were drop cast on 1 cm^2 of the carbon cloth paper. The catalyst on the carbon paper was exposed to a heat gun until dry. Before the *in situ* measurements, the incident energy was selected using a cryogenically-cooled Si (111) monochromator and calibrated to the first inflection point of Ni (8333.0 eV) and Pt (11564 eV) metal foils. Harmonic rejection was accomplished by using Rh-coated Si vertical and horizontal focusing mirrors inclined at 4 mrad. The electrochemical *in situ* cell, without solution and just the working electrode, was placed at 45° relative to the incident beam. To test for the proper signal of the

selected energy edges, 10 X-ray scans were run for each sample. The data were collected via fluorescence mode by using a four-element Vortex detector.

Subsequently, the *in situ* electrochemical cell was filled with 0.1 M KOH solution and the remaining electrodes, reference, and counter electrodes were placed in the cell. The electrochemical cell was purged with UHP N_2 for 15 minutes. Before the XAS measurements, CVs were done between -0.85 and 0.65 V vs. Ag/AgCl (sat. KCl) to test the electrochemical catalyst response in the *in situ* cell. This was followed by the XAS analyses via chronoamperometric measurements at 1.0, 0.9, 0.8, 0.5 and 0.3 V vs. RHE for 500 seconds at each potential. The XAS measurements were recorded simultaneously doing the electrochemical measurements. The same procedure was completed as the air was allowed inside the *in situ* cell with 0.1 M KOH solution, simulating an oxygen reduction under atmospheric conditions

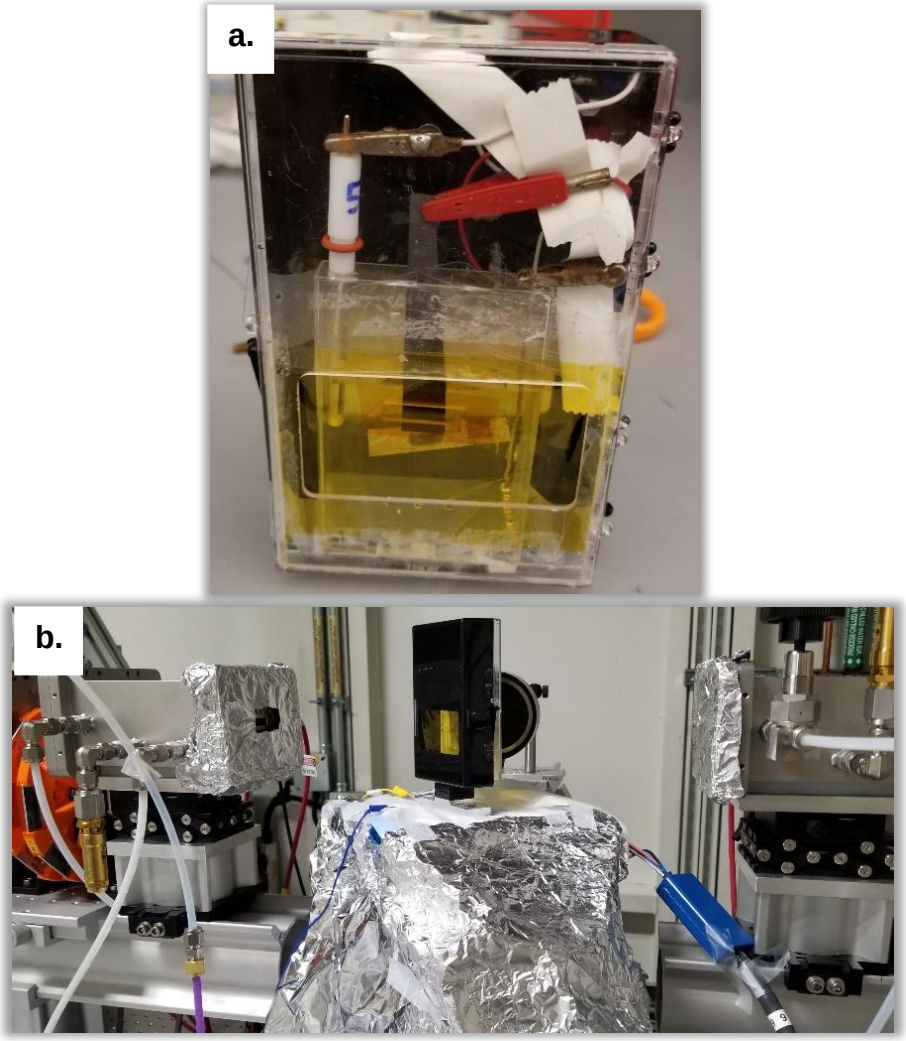

Figure 3.8 Electrochemical *in situ* cell setup (a) for the oxygen reduction reaction experiments in 0.1M KOH. (b) Beamline setup for the *in situ* experiments. This was the same electrochemical cell used in Sasaki et al. Adapted with permission from Sasaki, K.; Marinkovic, N.; Isaacs, H. S.; Adzic, R. R. Synchrotron-Based in Situ Characterization of Carbon-Supported Platinum and Platinum Monolayer Electrocatalysts. *ACS Catal.* **2016**, , 69–76. Copyright 2016 ACS.

3.5. References

(1) Niu, S.; Li, S.; Du, Y.; Han, X.; Xu, P. How to Reliably Report the Overpotential of an Electrocatalyst. *ACS Energy Lett.* **2020**, *5*, 1083–1087.

(2) Fang, L.; Tao, Q.; Li, M.; Liao, L.; Chen, D.; Chen, Y. Determination of the Real Surface Area of Palladium Electrode. *Chinese J. Chem. Phys.* **2010**, *23*, 543–548.

(3) Liang, Z. X.; Zhao, T. S.; Xu, J. B.; Zhu, L. D. Mechanism Study of the Ethanol Oxidation Reaction on Palladium in Alkaline Media. *Electrochim. Acta* **2009**, *54*, 2203–2208.

(4) Łukaszewski, M.; Soszko, M.; Czerwiński, A. Electrochemical Methods of Real Surface Area Determination of Noble Metal Electrodes-an Overview. *Int. J. Electrochem. Sci* **2016**, *11*, 4442–4469.

(5) Giri, S. D.; Sarkar, A. Electrochemical Study of Bulk and Monolayer Copper in Alkaline Solution. *J. Electrochem. Soc.* **2016**, *163*, H252–H259.

Chapter 4. ***In situ*** **X-ray Absorption Spectroscopy of PtNi-Nanowire/Vulcan XC-72R under Oxygen Reduction Reaction in Alkaline Media**

4.1. Abstract

Studying the ORR in the alkaline electrolyte has promoted better catalytic responses and accessibility to commercialization. Ni-Nanowires (NWs) were synthesized via the solvothermal method and modified with Pt using the SGD method to obtain PtNi-NWs. Carbon V was used as catalyst support, and they were doped with NH_3 to obtain PtNi-NWs/V and PtNi-NWs/V-NH_3. Their electrocatalytic response for the oxygen reduction reaction (ORR) was tested and PtNi-NWs/V provided the highest specific activity with logarithmic values of 0.707 and 1.01 (mA/cm^2_{Pt}) at 0.90 V and 0.85 V vs. RHE, respectively. PtNi-NWs showed the highest half-wave potential ($E_{1/2}$ = 0.89 V) at 1,600 rpm and 12 $\mu g_{Pt}/cm^2$ in 0.1 M KOH at (25.00 ± 0.01) °C. Additionally, the catalysts followed a 4-electron pathway according to the KL analysis. Moreover, durability experiments demonstrated that PtNi-NWs/V performance loss was like commercial Pt-V along 10,000 cycles. Electrochemical ORR *in situ* XAS results showed that the Pt L_3 edge whiteline in the PtNi-NWs catalysts changed while the electrochemical potential was lowered to negative values, from 1.0 V to 0.3 V vs. RHE. The Pt-O region in the *in situ* Fourier transforms (Ft) remained the same as the potentials were applied, suggesting an alloy formation between the Pt and Ni, and the Pt-Pt contracted in the presence of Ni. These results provide a better understanding of PtNi-NWs in alkaline electrolyte, suggesting that they are active catalysts for ORR and can be tuned for fuel cell studies.

4.2. Introduction

First-row transition metal NWs can be used as templates for PGM catalysts by applying the SGD method.[1] This thermodynamically favorable process occurs when a more noble metal interacts with a less noble metal. Here, the metal ion with a higher reduction potential will tend to reduce at the solid metal surface with a lower reduction potential.[2] Exciting results from NWs arrangement for ORR catalysis can be found. A few are ultrafine jagged Pt-Nanowires with impressive activity in acidic medium with a 13.6 A/mg_{Pt} at 0.90 V vs. RHE,[3] Alia *et al.* studied PtNi-Nanowire catalyst in acid medium resulting with 3 and 10 fold enhancement in specific and mass activity, respectively, compared with traditional Pt nanoparticles catalyst[4,5] and Shao *et al.* reported the different synthesis of platinum group metal (PGM) nanowires.[6]

In this work, we synthesized Ni NWs and modified them with Pt by SGD to obtain PtNi-NWs. The morphology, surface and crystallographic characterizations were studied. The specific and mass activities were evaluated with ORR polarization curves. Durability experiments were done to test the performance of the catalysts in an alkaline medium. Additionally, *in situ* XAS electrochemical studies were executed to evaluate the geometric and electronic structure of the catalyst while undergoing the ORR at a fixed electrochemical potential in 0.1 M KOH.

4.3. Research design and methods

4.3.1. Catalyst Synthesis

The synthesis of the Pt-Ni catalyst was divided into two steps: (1) the Nickel-NWs (Ni-NWs) were synthesized and (2) modified with H_2PtCl_6 (Sigma Aldrich)—a Pt precursor—to build the PtNi-NWs. For the synthesis of the Ni-NWs, a similar hydrothermal synthesis procedure was followed from Krishnadas *et al.*[7] Briefly, 7.5 mL of a total solution composed of an aqueous solution of 10 mM of $NiCl_2$ (Sigma Aldrich) and ethylene glycol (EG) (Sigma Aldrich) was heated up to 120 °C in an oil bath inside a round 50.00 mL flask with a magnetic stirrer. Then, when the 50.00 mL round flask reached 120 °C, 0.1 mL of hydrazine hydrate (Sigma Aldrich) was added slowly five times every 1 minute. In the end, a total of 0.5 mL of hydrazine hydrate was added to the solution (it went from a light blue to a black color). This solution was stirred for 10 minutes and cooled at ambient temperature for 1 hour. The solution was separated at 3,400 rpm using a centrifuge (Cole Palmer 17250-10). The solid was rinsed using ethanol (Sigma Aldrich), isopropanol (Sigma Aldrich) and nanopure water (18.2 MΩ·cm). Then, the catalyst was dried using an oven (Lindberg/Blue MO1450A-1) for 24 hours at 60 °C. Finally, the remaining catalyst was ground by hand—with light pressure—using a small quartz mortar to obtain a powder material.

PtNi-NWs were obtained with SGD considering Pt and Ni standard potentials (**Table 4.1**) following the procedure from Alia *et al.*[5] In a typical synthesis, 80 mg of lab-made Ni-NWs was added to a bottom of a 250 mL round flask with 160 mL of pure water and heated at 90˚C in an oil bath. A premade aqueous solution of 15

mL of 10 mM H_2PtCl_6 was added to the bottom round flask with the lab-made Ni-NWs in intervals of 15 minutes. The whole mixture was mixed with a magnetic stirrer and left for 2 hr at 90°C. The remaining solution was taken out (of the oil bath) and left to cool down to ambient temperature. The resulting PtNi-NWs were dried using the same procedure as the previously synthesized Ni-NWs. Carbon Vulcan XC-72R (V) and PtNi-NWs were added to a 150 mL beaker with 100 mL of ethanol. Then, the dispersion was sonicated for 1 hr and dried following the earlier procedure. The remaining catalyst (PtNi-NWs/V) was in a proportion of (80/20) % V and PtNi-NWs. PtNi-NWs/V samples were annealed at 250°C in N_2 stream followed by NH_3 gas up to 510°C at a heating rate of 4.8 °C/min.

Table 4.1. Standard reduction potentials for Pt and Ni.

Metal Reaction	*E°(V) vs. RHE*
$Pt^{2+} + 2e^- \leftrightarrow Pt^{\circ}$	**1.180**
$Ni^{2+} + 2e^- \leftrightarrow Ni^{\circ}$	**-0.257**

4.3.2. Electrochemical characterization

CV was used to certify the presence of metallic Ni in the product of the first synthesis and then the characterization of the PtNi-NWs. The electrochemical setup consisted of a three-electrode temperature-controlled cell. To reduce interferences, the electrochemical cell was cleaned with aqua regia before the experiments. This jacketed cell is composed of a glassy carbon (GC) WE, a Ag/AgCl sat. KCl RE and a Pt CE using an Autolab PGSTAT 30 with a rotating disk electrode (RDE) setup (Pine Instruments). The GC electrode was physically cleaned before every experiment by polishing the GC surface with alumina micro-

polish (Buehler) while decreasing the value of granular pore size (1.0, 0,5 and 0.03) µm and pure water, in an eight-shape pattern.

The temperature control cell was set at (25.0 ±0.1) ºC using a Nestlab RTE-221 chiller and left for 10 minutes with the aqueous solution (0.1 M KOH) while its temperature reached 25.0 ºC. Then, electrochemical cleaning was executed between 1.0 and 1.6) V vs. RHE at (100, 50 and 20) mV/s in 0.1 M KOH. After the surface of the GC electrode was physically and electrochemically cleaned, an ink dispersion of the catalyst was used to modify the surface of the GC electrode. A stock solution was prepared consisting of a ratio of 2:1:1:0.10 volume of ethanol (99.5% Sigma Aldrich), pure water, isopropanol (Sigma Aldrich) and 5 µL of Nafion (5% solution in alcohol, Sigma Aldrich), respectively. The mass addition of the catalyst was added considering the mass loading relationship **Equation 4.1**[8].

$$M_L = \frac{w \cdot V_{alq}}{V_{suspesion} \cdot A_{geo}} \qquad \textbf{Eq. 4.1}$$

Here, w is the catalyst powder mass in mg, V_{alq} is the volume (µL) dropped on the glassy carbon disk electrode, V_{sup} is the suspension volume (µL) and A_{geo} is the geometric electrode surface area, in cm^2, that was modified. We used a 0.1963 cm^2 GC electrode.

The catalyst ink dispersion was sonicated for 30 minutes and an aliquot of 5 µL was drop cast on the GC electrode surface. The electrode was left at ambient temperature (25 °C) for (15-20) minutes until the ink dried. Then, a CV was obtained at the Ni potential window from 1.0 to 1.7 V vs. RHE at a scan rate of 20 mV/s in 0.1 M KOH. Similarly to this procedure, PtNi-NWs catalysts were

characterized, but ultra-high pure (UHP) N_2 was purged before, for 15 minutes to prevent poisoning of the Pt surface while in solution. For PtNi-NWs, the potential window used was different, from 0.0 to 1.7 V vs. RHE.

4.3.3. Rotating disk electrode experiments

Before the rotating disk experiments, the solution (0.1 M KOH) was purged using UHP N_2 for 15 minutes. Later, a potential of 1.2 V vs. RHE was applied for 30 seconds and the LSV measurements, using the potential window between 1.2 and 0.0 V vs. RHE and at a scan rate of 10 mV/s, were done. This voltammetry was used to lower the capacitive currents. Subsequently, the catalysts were activated by cycling the potentials while the rotator was turned on at 1,600 rpm in the potential window between 0.0 and 1.2 V vs. RHE at 100 mV/s for 15 minutes while UHP O_2 was purged. An additional LSV was acquired at the potential window between 1.2 and 0.0 V vs. RHE at 10 mV/s. Nyquist plots were used to obtain the uncompensated resistance of the measurements. All the polarization curves were corrected by iR ($E(V)=E_{RHE}(V) - i(A)R(\Omega)$). The measurements were also normalized by the geometric area of the GC RDE (0.1963 cm^2) and the mass loading of the catalyst was used to calculate de mass activity at 0.90 V and 0.85 V vs. RHE. LSVs, under variable rpm were subsequently done. These revolutions were: 400, 600, 900, 1200, 1600 and 2000 rpm. The limiting currents of these curves were obtained and used to calculate the number of electrons transferred, applying the Koutecký-Levich (KL) equation and Levich equation **Equation 4.2**[9] and **Equation 4.3**[10]**,** respectively.

$$\frac{1}{j_L} = \frac{1}{j_k} + \frac{1}{\sqrt{B\omega}} \qquad \textbf{Eq. 4.2}$$

Here, j_L is the limiting diffusional current density, j_k is the activation controlled current density, ω is the rotation rate of the electrode, B represents 0.62nF C(O_2) $D_0^{2/3}v^{-1/6}$ (this is also the slope of Levich equation (**Eq. 1.**)

$$j_{dif} = 0.62nF\ D_0^{\frac{2}{3}} v_0^{-\frac{1}{6}}\ C_0 w^{\frac{1}{2}} \qquad \textbf{Eq. 4.3}$$

Here *n* is the number of transferred electrons through the reaction, F is the Faraday's constant (96,487 C mol^{-1}), D_0 is the oxygen diffusion coefficient, v_0 is the kinematic viscosity, C_0 is the solubility of the gas (O_2) in the electrolyte and w is the rotating rate in rpm. In 0.1 M KOH solutions, D_0 = 1.9 x 10^{-5} cm^2 s^{-1}, v_0 = 8.7 x 10^{-3} cm ^{2} s^{-1} and C_0 = 1.22 x 10^{-6} mol cm^{-3}.[54]

Durability experiments were done to test the stability of the catalyst for prolonged periods under reaction conditions (0.1 M KOH). The following sequence was followed: (1) A voltammogram was obtained under UHP N_2 environment using the PtNi potential window between 0.20 and 1.65 V vs. RHE at a scan rate of 50 mV/s. (2) Both N_2 and O_2 LSVs were recorded as in (1). (3) 5,000 CV cycles between 0.6 and 1.0 V vs. RHE were recorded at a scan rate of 100 mV/s. (4) Steps (1), (2) and (3) were repeated. (5) The experiment was finalized by recording a third and final CV as step (1) and LSVs as step (2). It is essential to clarify that the Ag/AgCl reference electrode used during these 10,000 voltammetric cycles differed from the one used to do the cyclic voltammograms and polarization curve experiments**.** The 0.1 M KOH solution was also changed after the first 5,000 cycles and after the 10,000 cycles to prevent solution contamination and shifts in the electrochemical potentials due to possible Ag/AgCl RE inner solution leaks.

The calibration of the RE was done daily to ensure a fixed potential. A commercial RHE electrode (edaq) was used to compare the potential of the Ag/AgCl sat. KCl electrode in an 0.5 M H_2SO_4 solution. All the potentials were converted to RHE using the Nernst equation considering the [H_3O^+] activity **Equation 3.1**.

The ORR electrocatalytic activity of the PtNi-NWs was evaluated using O_2 polarization curves. Initially, without using a temperature controller, the data gathered was not reproducible. Therefore, after implementing the temperature-controlled system, the reproducibility of the data was obtained. The use of a temperature-controlled electrochemical system is not widely discussed for the ORR reaction; however, there is an urge to use these systems when using the KL equation **Equations 4.2 and 4.3** since several equation constants are temperature-dependent, as well as the Ag/AgCl electrode potential.

4.3.4. Transmission electron microscopy

The structural morphology of the samples was confirmed with a 200 kV field emission FEI F20 high-resolution transmission electron microscope (HR-TEM) from the facilities at the Cornell Center for Materials Research (CCMR) at Cornell University. The samples were prepared on a lacey carbon film of 300 mesh Cu grid (electron microscopy sciences, EMS). The chemical composition of the samples was examined with energy dispersive spectroscopy (EDS) with the scanning transmission electron microscope (STEM) mode and using an Oxford instruments X-ray detector.

4.3.5. X-ray powder diffraction

PXRD was utilized to determine the diffraction pattern of the PtNi catalysts. A Rigaku SmartLab X-Ray diffractometer working with a Cu K_α radiation (λ = 1.54 Å) was used. The 2Θ range was scanned between 5-100° at a rate of 0.02°s^{-1}. The smart lab software was used for background correction. Origin software was used to finalize the peak processing with the smoothness of the signals using the Savitzky-Golay filter.

4.3.6. Inductively coupled plasma-optical emission spectroscopy

The metal concentrations were determined using ICP–OES Optima 8000 Perkin Elmer equipment with standard plasma parameters **Table 4.2**. The digestion procedure to dissolve the selected metals were done as follows: six samples of ~3 mg were digested with 10 mL aqua – regia solution and heated to simmering until 0.5 mL remained. After cooling down to room temperature, the dissolved metals were reconstituted with a 2% HNO_3 solution and analyzed immediately.

Table 4.2. ICP plasma parameters

Gas Flows (L/min)			*RF Power (Watts)*	*Pump Flow Rate (mL/min)*
Plasma	Auxiliary	Nebulizer		
1.5	0.2	0.55	1300	1.5

4.3.7. X-ray photoelectron spectroscopy

The surface structure of the catalysts was further analyzed using XPS. A PHI 5600ci spectrometer equipped with a polychromatic magnesium source (1253.6 eV) was used at 45° with a hemispherical electron energy analyzer. The resolution/pass energy was 58.7 eV. The powder samples were deposited using copper tape and the binding energy spectra of Ni and Pt species were studied using Casa XPS software—for peak deconvolutions and speciation attribution. The spectra were corrected with adventitious carbon C1s binding energy of 284.80 eV. A Shirley background was used for all the analysis. An asymmetrical line shape consisted of Lorentzian Asymmetric (LA) α, β, *m* (where α and β defined the spread of the tail on any side of the Lorentzian component and *m* specified the Gaussian width used to convolute the Lorentzian curvature) was implemented to the Pt ($4f_{7/2}$) and the Ni ($2p_{3/2}$) components.[11,12] The remaining components of the samples were analyzed with Gaussian (70%) and Lorentzian (30%) line shapes.

4.3.8. X-ray absorption spectroscopy

4.3.8.1.Ex situ XAS

XAFS measurements of the catalysts were done at beamline 7-BM for quick X-ray absorption (QAS) at the National Synchrotron Light Source II (NSLS-II) at Brookhaven National Laboratory (BNL). The Pt K-edge data was collected in fluorescence yield mode using a passivated implanted planar silicon (PIPS) detector. Data proceeding was done using the IFEFFIT package.[13]

4.3.8.2. *In situ* XAS

In situ XAS experiments were done at beamline 7-BM for QAS at NSLS-II at BNL and the PIPOXS beamline at Cornell High Energy Synchrotron Source (CHESS). See section 3.4 of chapter 3 for more details.

4.4. Results and discussion

4.4.1. Transmission electron microscopy

HR-TEM was used to examine the morphology of Ni and PtNi catalysts. The Ni particles obtained after solvothermal synthesis exhibited a nanowire structure **Figure 4.1** (**a,b**) with an average diameter of 96 ± 28 nm and an average length of 590 ± 212 nm **Figure 4.2**. These images exhibited ramifications of the Ni-NWs with different observed sizes. The synthesis of choice required the use of EG since it acts as a reducing agent, preventing particle agglomeration, thus acting as a stabilizing agent. The EG led to the formation of these ramifications while preventing the agglomeration of the Ni particles resulting in the wire morphology. A high-resolution TEM image of the Ni-NWs is seen in **Figure 4.1c** and in **Figure 4.1d,** the green, yellow, and brown rings in the FFT spots of the HR-TEM image of the Ni-NWs corresponded to the lattice spacing 2.4, 2.1 and 1.5 Å respectively. These spots are related to the planes 111, 002 and 022 of the crystalline structure of Ni oxide (NiO) (98-000-9861).

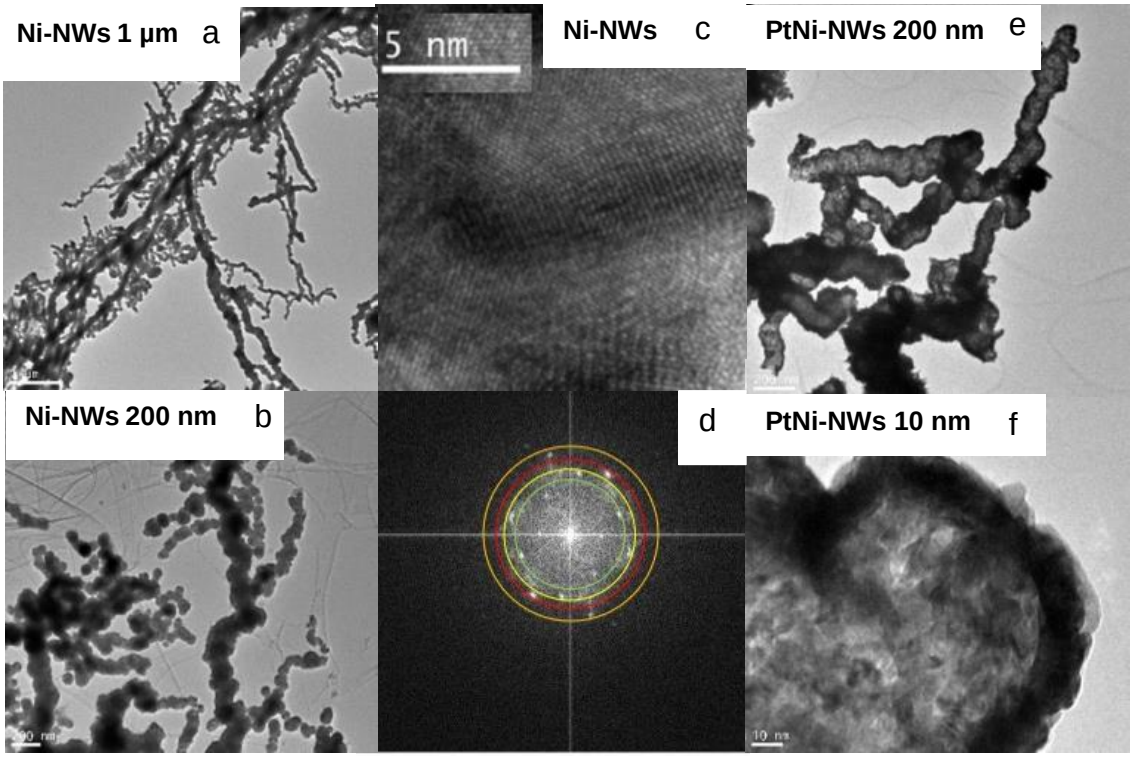

Figure 4.1 TEM images of Ni-NWs and PtNi-NWs. (**a, b**) Bright field (BF) images of Ni showing wire—like morphology. (**c**) High resolution image of the Ni-NWs. (**d**) FFT spots of the Ni-NWs(**e, f**) BF images of PtNi-NWs.

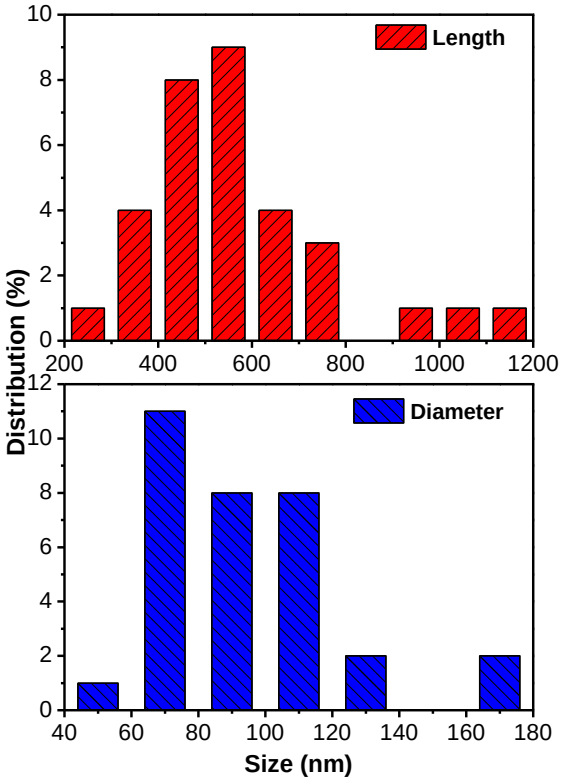

Figure 4.2 Histogram of the distribution of Ni-NWs length and diameter sizes.

The yellow and red ring corresponds to the lattice spacings 2.1 and 1.8 Å, respectively, related to the 111 and 002 planes of metallic Ni (Ni°) of the Ni-NWs **Figure 4.3**. The crystallographic parameters for Nickel are shown to justify the presence of the *hkl* planes related to NiO and Ni°. In addition, in **Figure 4.4** we demonstrated another spot of the FFT in the Ni-NWs showing similar planes associated with the NiO and Ni° crystalline structures. The yellow and red rings in the FFT spots corresponded to the lattice spacing 2.1 and 1.8 Å, respectively, related to the 111 and 002 planes of the crystalline structure of Ni° (98-004-3397). Additionally, the yellow ring corresponded to the lattice spacing 2.1 Å related to the 002 planes of NiO (98-000-9861). This indicates that some Ni-NWs were reduced, eventually serving as a template to form the PtNi-NWs.

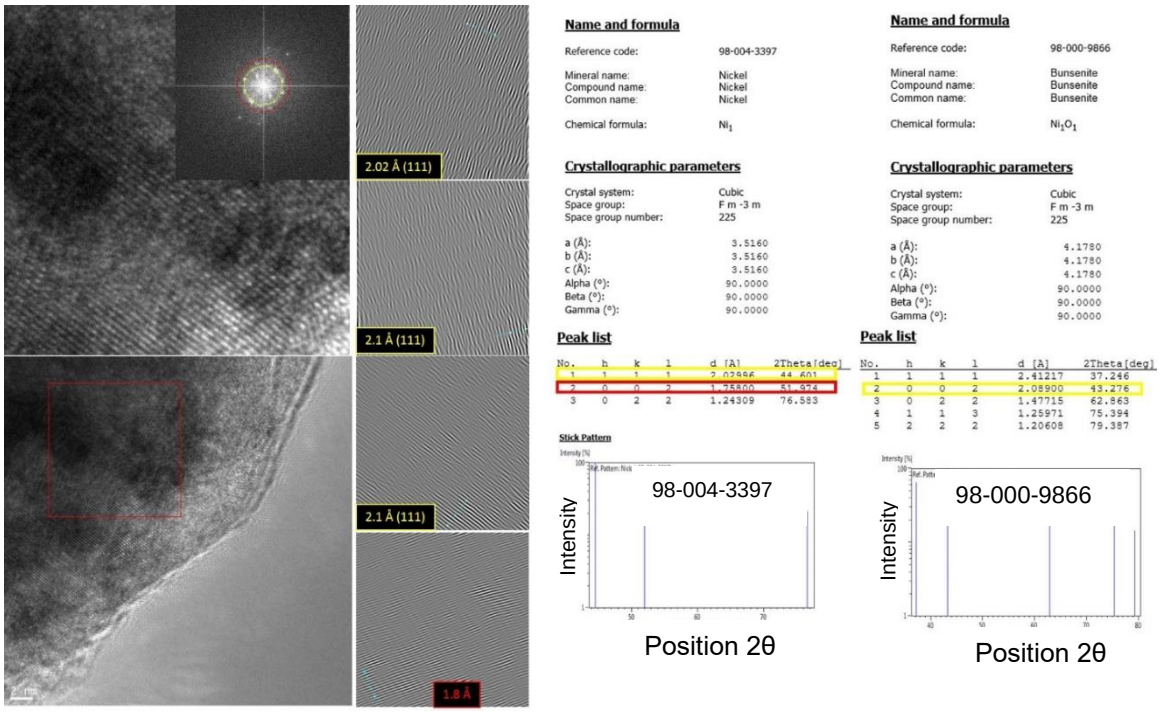

Figure 4.3 High-resolution TEM images of Ni-NWs with FFT spots.

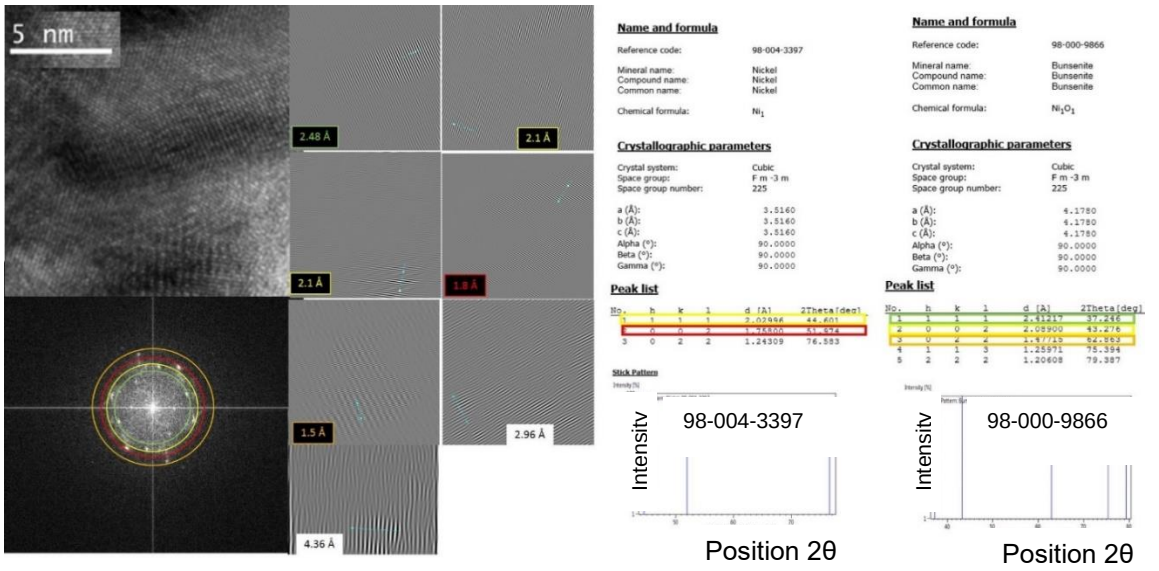

Figure 4.4 High-resolution TEM images of Ni-NWs with FFT spots.

The Pt deposition on the Ni-NWs was done using the SGD. TEM measurements on the PtNi-NWs provided evidence of its formation through the SGD (**Figure 4.1 e** and **f**). These images showed a difference in contrast between the brighter inner cores and darker outer layers of the NWs, suggesting that the cores comprise Ni (lower mass) while the shell layers consist of Pt (higher mass).

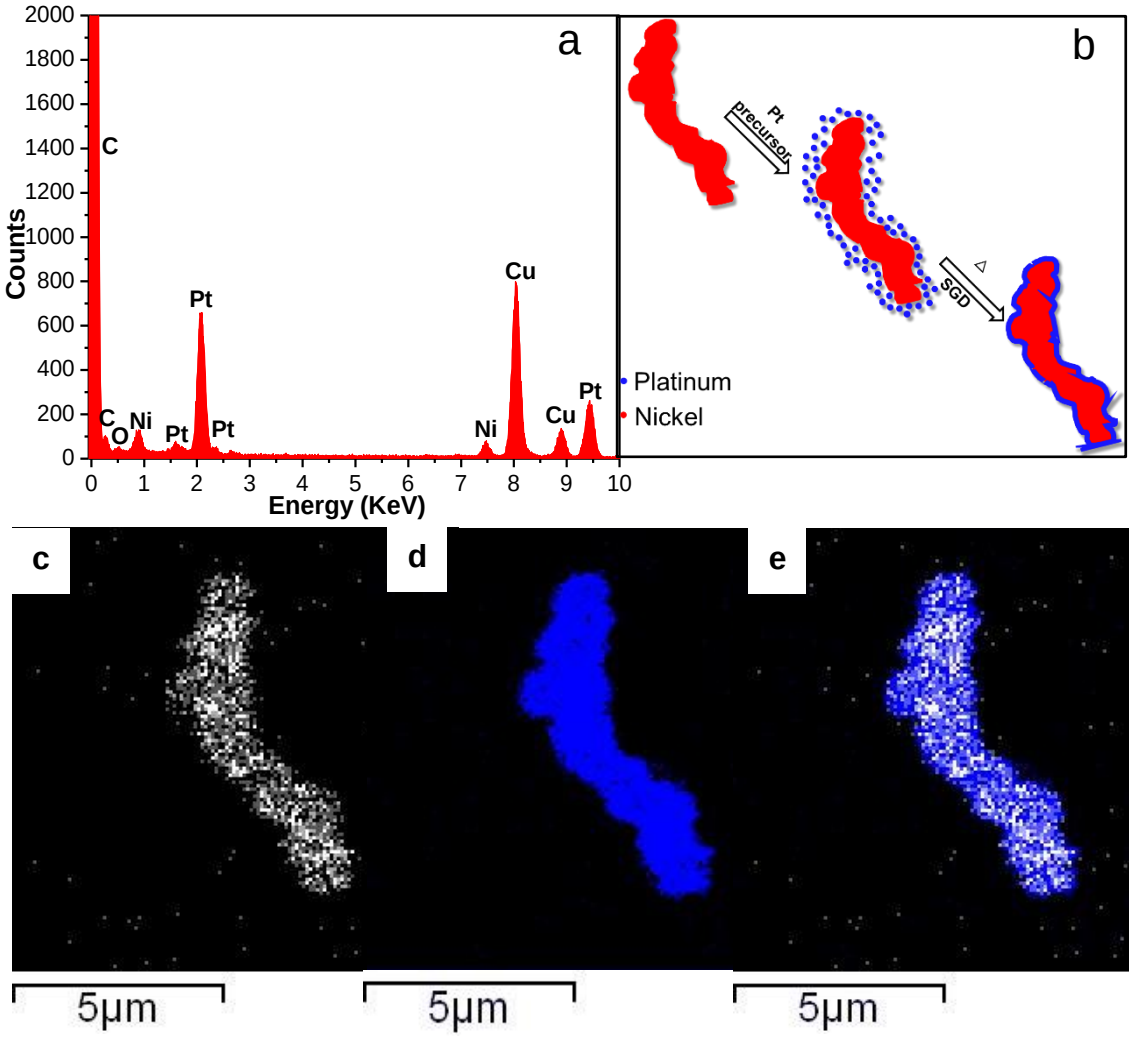

Figure 4.5 EDS spectrum of the PtNi-NWs (**a**). Suggested diagram for the atom positioning in the nanowire (**b**).X-ray map of the PtNi-NWs sample, Nickel (**c**), Platinum (**d**) and overlay of PtNi (**e**).

This structure is also confirmed with the EDS spectrum (**Figure 4.5a**) and the EDS mapping (**Figure 4.5 c,d** and **e**). In the spectrum, we see the presence of Pt and Ni, and when we overlay the EDS map of Ni and Pt, Ni is on the inside of the NW and Pt on the outside. According to the EDS data, the atomic composition of the PtNi-NWs catalyst was 3:1 Pt:Ni (**Table 4.3**).

Table 4.3 Energy dispersive X-ray (EDS) data for the PtNi-NWs using STEM.

Element	***Peak Area***	***Area Sigma***	***k factor***	***Abs Corr.***	***Weight%***	***Weight% Sigma***	***Atomic%***
C K	2158	169	1.000	1.000	6.55	0.48	32.0
O K	444	88	0.747	1.000	1.01	0.20	3.7
Ni K	2267	108	0.506	1.000	3.48	0.16	3.5
Cu K	32512	305	0.556	1.000	54.82	0.55	50.6
Pt L	10476	214	1.074	1.000	34.14	0.53	10.3
Totals	100						

4.4.2. Inductively coupled plasma-optical emission spectroscopy

Furthermore, ICP-OES was used to confirm the Pt:Ni ratio and weight concentration (**Table 4.4**). ICP showed a relationship of 1:2 Pt:Ni and the *wt%* concentrations were 60.9 ± 0.9 and 39.1 ± 1, for Pt and Ni, respectively. These ICP values were used for all the experimental procedures.

Table 4.4 Metal concentration with ICP-OES

Metal	***concentration (% wt ± Std)***	***Atomic ratio (Pt:Ni)***
Pt	60.9 ± 0.9	1:2
Ni	39 ± 1	

4.4.3. X-ray powder diffraction

PXRD was used to corroborate the presence of the reduced crystalline patterns of Ni from the Ni-NWs synthesis and the presence of Pt and Ni after the galvanic displacement. For the Ni-NWs, diffraction peaks of 2θ values at 44.5°, 51.8°, 76.4°, 92.9°, and 98.5° were found (**Figure 4.6a**). These reflections correspond to the fcc lattice structure assigned to the (111), (200), (220), (311) and (222) Miller indexes of Ni, respectively.[14] For the PtNi-NWs, the Pt diffraction patterns are assigned to the fcc lattice of Pt. Bragg's reflection signals of 2θ value (**Figure 4.6b**) at 39.9° (111), 46.5° (200), 67.9° (220), 81.8° (311), 86.4° (222) attributed to fcc Pt.[15–18] This may be due to an alloy formation between Pt and Ni.[16] Because the reduction of Pt on Ni was carried out in the aqueous solution at 90°C, the Ni species present in the PtNi-NWs may be oxidized or in an amorphous nature. This result will be reflected in the presence of just the crystalline structure of Pt in the PtNi-NWs pattern.[19]

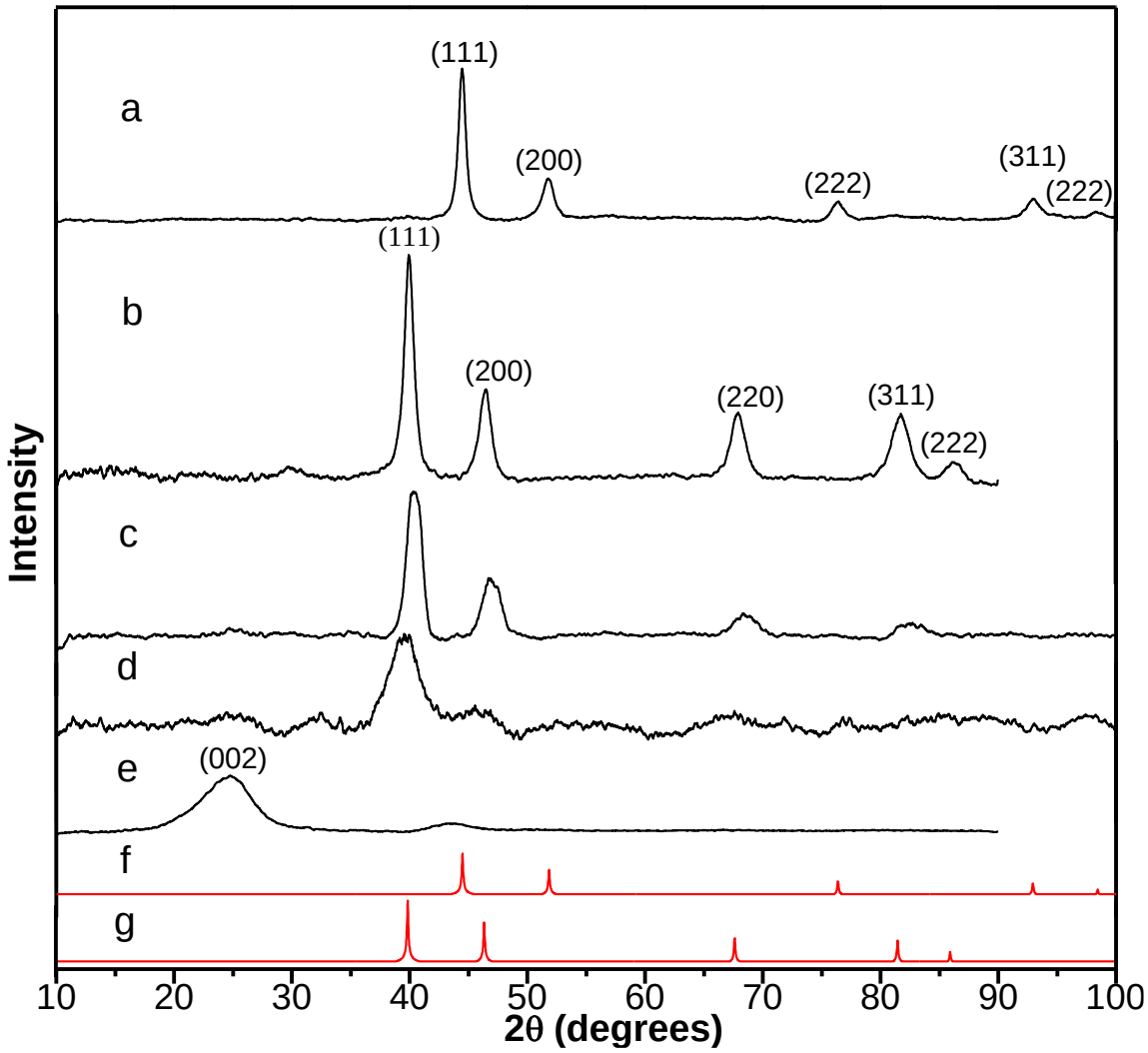

Figure 4.6 XRD patterns for Ni-NWs (**a**), PtNi-NWs (**b**), PtNi-NWs/V (**c**), together with commercial Pt/V (**d**) and commercial V (**e**). Standard peak of Ni from 64989 Inorganic crystalline structure database (ICSD) (**f**) and Pt from 0018004 American mineralogist crystal structure database (AMCSD) are also shown for comparison (**g**).

4.4.4. X-ray photoelectron spectroscopy

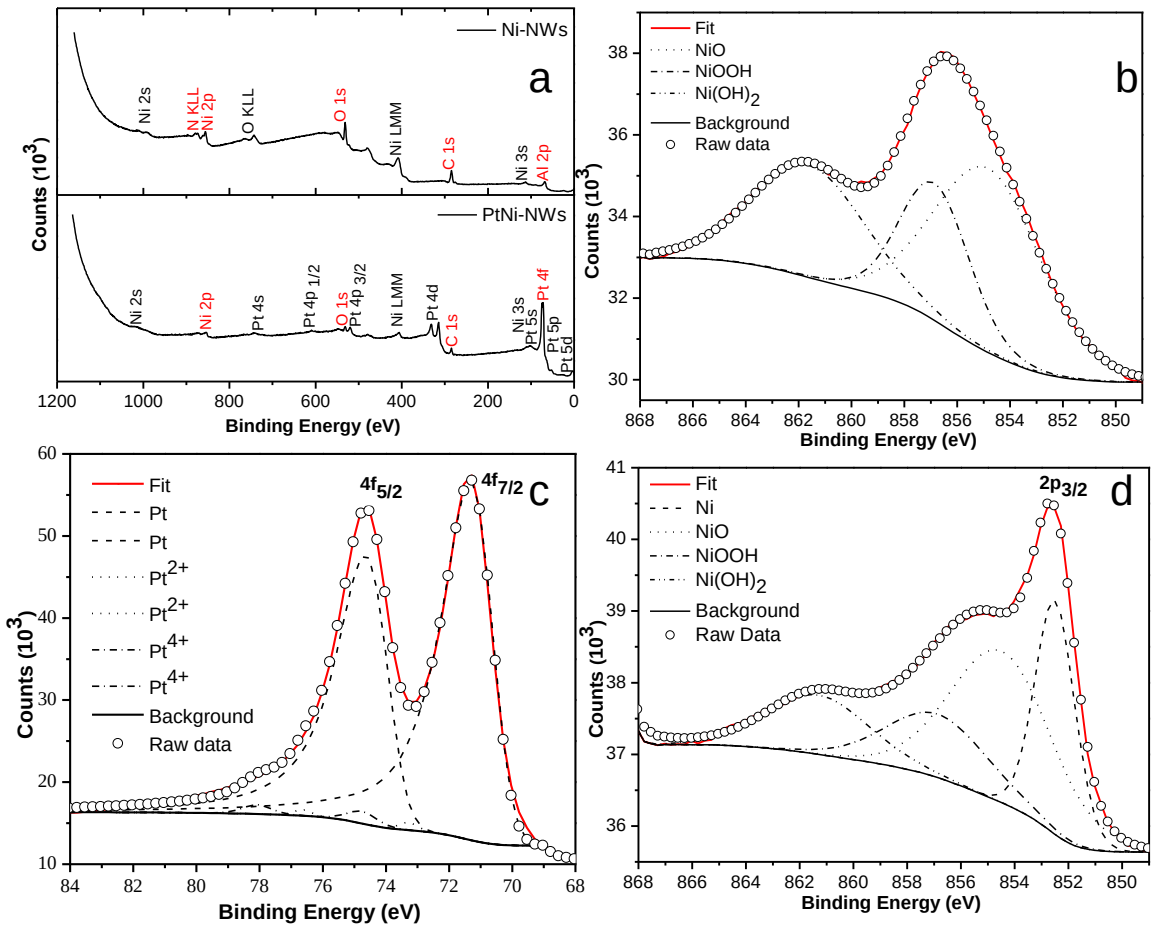

Figure 4.7 Peak deconvolutions for Pt 4f and Ni 2p bind energy region. (**a**) Survey data of Ni-NWs and PtNi-NWs. (**b**) Peak deconvolutions of Ni-NWs. Peak deconvolutions of Pt (**c**) and Ni (**d**) of the PtNi-NWs sample.

XPS was done to examine the Pt and Ni oxidation states at the material's surface. **Figure 4.7a** reveals the survey data obtained for both, Ni-NWs and PtNi-NWs samples. **Figure 4.7b**, is a deconvoluted spectrum of Ni-NWs using the Ni 2p region. The spectrum showed speciation of Ni atoms in different oxidation states as oxides and hydroxides species. The atomic percentage (*At%)* was calculated according to the deconvoluted relative peak areas (**Table 4.5**), resulting with *At%* of 23.0%, 30.4% and 46.6% for NiOOH, $Ni(OH)_2$ and NiO, respectively.[11]

Table 4.5 Physico-chemical properties for Pt $4f_{7/2}$ and Ni $2p_{3/2}$ binding energy regions

Sample	PtNi-NWs							Ni-NWs		
Chemical composition	Pt	Pt^{2+}	Pt^{4+}	Ni	NiO	NiOOH	$Ni(OH)_2$	NiO	NiOOH	$Ni(OH)_2$
Position (B.E) eV	70.8	73.3	74.8	852.5	854.5	856.9	861.3	854.8	856.9	861.6
FWHM	1.6	0.6	1.1	1.7	4.5	4.5	4.5	4.7	3.1	5.0
At.%	97.8	0.6	1.6	25.1	41.4	17.4	14.2	46.6	23.0	30.4

4.4.5. Ex situ X-ray absorption spectroscopy

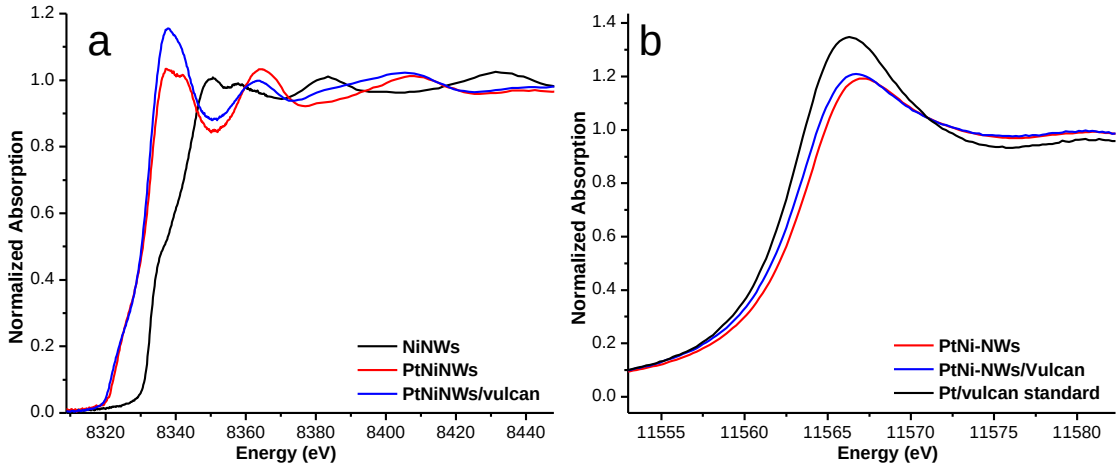

Figure 4.8. Ex situ XANES energy region spectra of (**a**) Ni-K and (**b**) Pt-L3 edges of PtNi-NWs/V.

According to the high-resolution TEM FFT and the XRD patterns on the Ni-NWs, there is Ni° (see **Figure 4.1c** and **d**, **Figure 4.3** and **4.4** and **Figure 4.6a**), allowing the SGD with Pt. However, in the XPS spectrums, the Ni° peak is missing on the Ni-NWs sample, suggesting that the sample surface was oxidized, a phenomenon previously observed when Ni is exposed to air at room temperature.[20,21] The Ni-NWs width is ca. 100 nm and the XPS signal may come from less than ca. 5 nm of the surface. **Figure 4.7d** shows the XPS spectrum of the Ni 2p binding energy region of PtNi-NWs. The spectrum was deconvoluted into

four different peak regions. In this sample, Ni° is found at 852.51 eV and other oxides and hydroxide species are attributed to the other peaks. In agreement with TEM data, the SGD was successfully observed using EDS mapping, corroborating that Ni is inside the PtNi-NWs and Pt is outside the NW (**Figure 4.5**). The atomic % (At%) were also calculated according to the deconvoluted relative peak areas (see **Table 4.5**), resulting in 14.2%, 17.4%, 25.1% and 41.4% for $Ni(OH)_2$, NiOOH, Ni°, and NiO, respectively. The Pt 4f binding energy region was deconvoluted and three peaks were obtained, see **Figure 4.7c**. Predominantly, Pt° is observed with an At% of 97.8% at 70.83 eV. Other Pt oxide species were assigned at 73.29 eV (Pt^{2+}) and 74.76 eV (Pt^{4+}). These XPS results confirm this assumption since Pt was expected to be reduced during the SGD procedure. It is also essential to consider that Pt may be donating electronic density to Ni, because at first, in the Ni-NWs sample, Ni° was not present and after the SGD (PtNi-NWs) Ni° was found. To further corroborate this premise, ex situ XAS analysis was used.

XAS experiments were done first to compare the chemical properties of the ORR catalyst with previous ex situ characterizations. Mainly, the ex situ XAS data (see **Figure 4.8**) can be related to the XPS results. Previously, the XPS results raise the following question regarding why the Ni° is missing in the linear combination analysis of the 2p peak: (i) only the Ni surface of the Ni-NWs sample was oxidized in the air or chemically (see **Figure 4.7b**) or (ii) Ni obtained electron density from Pt deposited on the Ni-NWs surfaces by the SGD, resulting in Ni° in the Ni XPS from the PtNi-NWs sample (see **Figure 4.7d**). The ex situ XANES data goes in accordance with the statement that Pt is donating electrons to Ni. In **Figure**

4.8a, the order of white line peak intensity in Ni K edge spectra is PtNi-NWs/V > PtNi-NWs > Ni-NWs. In the spectra, a shift towards lower energies for the PtNi-NWs/V and PtNi-NWs samples, when compared to the Ni-NWs, is observed. As shown in the Pt L_3 edge spectra in **Figure 4.8b**, the order of the white line peak intensity is commercial Pt-V > PtNi-NWs/V > PtNi-NWs and in the PtNi-NWs and PtNi-NWs/V samples, Pt has a lower white line intensity than commercial Pt-V catalyst. Our following approach focused on evaluating if these trends, in both Pt and Ni edges, remains the same undergoing electrochemical *in situ* experiments in alkaline electrolyte.

4.4.6. ORR catalytic activity

As shown in **Figure 4.9** a mass loading study was considered to follow the optimal loading ratio for the catalysts using **Equation 4.1**.

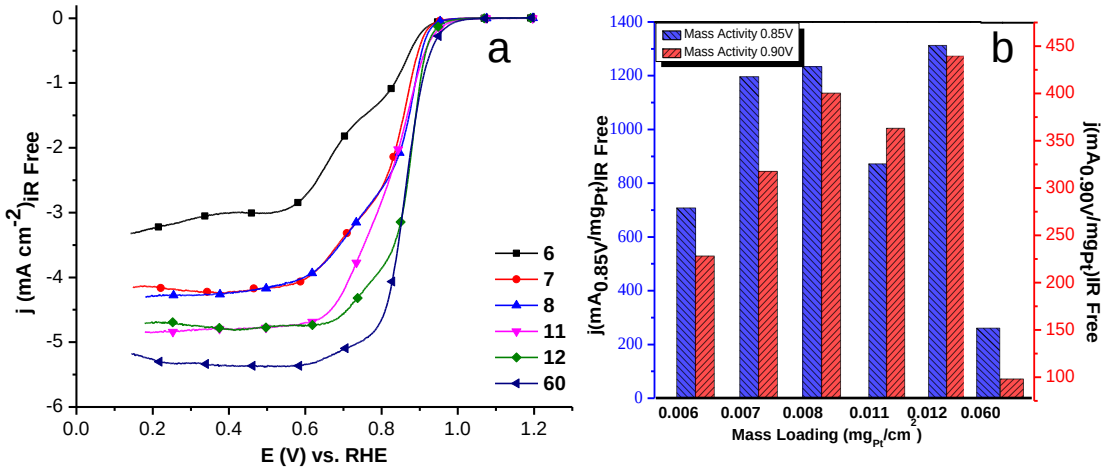

Figure 4.9 (**a**) O_2 polarization curves of the PtNi-NWs/V catalyst at 1,600 rpm with a scan rate of 10 mV/s in 0.1 M KOH, and 25°C, (**b**) the mass activity at 0.85 V and 0.90 V. The mass loading $\mu g_{Pt}/cm^2$ of Pt varied (6, 7, 8, 11, 12 and 60 $\mu g_{Pt}/cm^2$).

ICP-OES was used to calculate the w/w% of the metals in the catalyst material. The values were added to the numerator of the equation to calculate the metal loading factor in the samples. The optimal loading of Platinum resulted in 12 $\mu g_{Pt}/cm^2$ with an $E_{1/2}$= 0.87 V. The mass activities for the different mass loadings at 0.85 V and 0.90 V are presented in **Figure 4.9b** as well as **Table 4.6 and 4.7**. The PtNi-NWs/V with 12 $\mu g_{Pt}/cm^2$ resulted with 446 mA/mg_{Pt} at 0.90 V, complying with the DOE 2020 targets for membrane electrode assembly (MEA) of PGM catalysts.[22] For the sample with 0.060 mg_{Pt}/cm^2 loading, 98 mA/mg_{Pt} was obtained at 0.90 $V_{iR\text{-}Free}$. This is a significant difference in terms of activity. Thus, the mass

loading of 12 $\mu g_{Pt}/cm^2$ was used for the remaining experiments. If we compare this mass loading to DOE 2020 target (125 $\mu g_{PGM}/cm^2_{Electrode\ area}$) for MEA our loadings are lower and are still able to achieve the mass activity suggested by their standards, suggesting a promising activity for our ORR electrocatalyst.

Table 4.6 Mass loading corrected experimental values at 0.90 V vs. RHE

Specific activity at 0.90 V of PtNi-NWs/C 20% vulcan XC-72R									
I(A)	I(A)	ML(μg/cm^2)	ML(mg/cm^2) Pt and Ni	ML(mg/cm^2) Pt	mg(Pt and Ni)	mg(Pt)	(A/mg) Pt and Ni	(A/mg) Pt	(mA/mg)pt
0.27	0.00027	50	0.010	0.006	0.0020	0.00118	0.135	0.226	226
0.45	0.00045	60	0.012	0.007	0.0024	0.00141	0.190	0.316	316
0.66	0.00066	70	0.014	0.008	0.0027	0.00165	0.239	0.399	399
0.78	0.00078	90	0.018	0.011	0.0035	0.00212	0.221	0.368	368
1.05	0.00105	100	0.020	0.012	0.0039	0.00236	0.267	0.446	446
1.15	0.00115	500	0.100	0.060	0.0196	0.01178	0.059	0.098	98

Table 4.7 Mass loading corrected experimental values at 0.85 V vs. RHE

Specific activity at 0.85 V of PtNi-NWs/C 20% vulcan XC-72R									
I(mA)	I(A)	ML(μg/cm^2)	ML(mg/cm^2) Pt and Ni	ML(mg/cm^2) Pt	mg(Pt and Ni)	mg(Pt)	(A/mg) Pt and Ni	(A/mg) Pt	(mA/mg)pt
0.83	0.00083	50	0.010	0.006	0.0020	0.00118	0.425	0.708	708
1.69	0.00169	60	0.012	0.007	0.0024	0.00141	0.717	1.196	1196
2.03	0.00203	70	0.014	0.008	0.0027	0.00165	0.739	1.231	1231
1.88	0.00188	90	0.018	0.011	0.0035	0.00212	0.532	0.887	887
3.14	0.00314	100	0.020	0.012	0.0039	0.00236	0.801	1.335	1335
3.23	0.00323	500	0.100	0.060	0.0196	0.01178	0.165	0.274	274

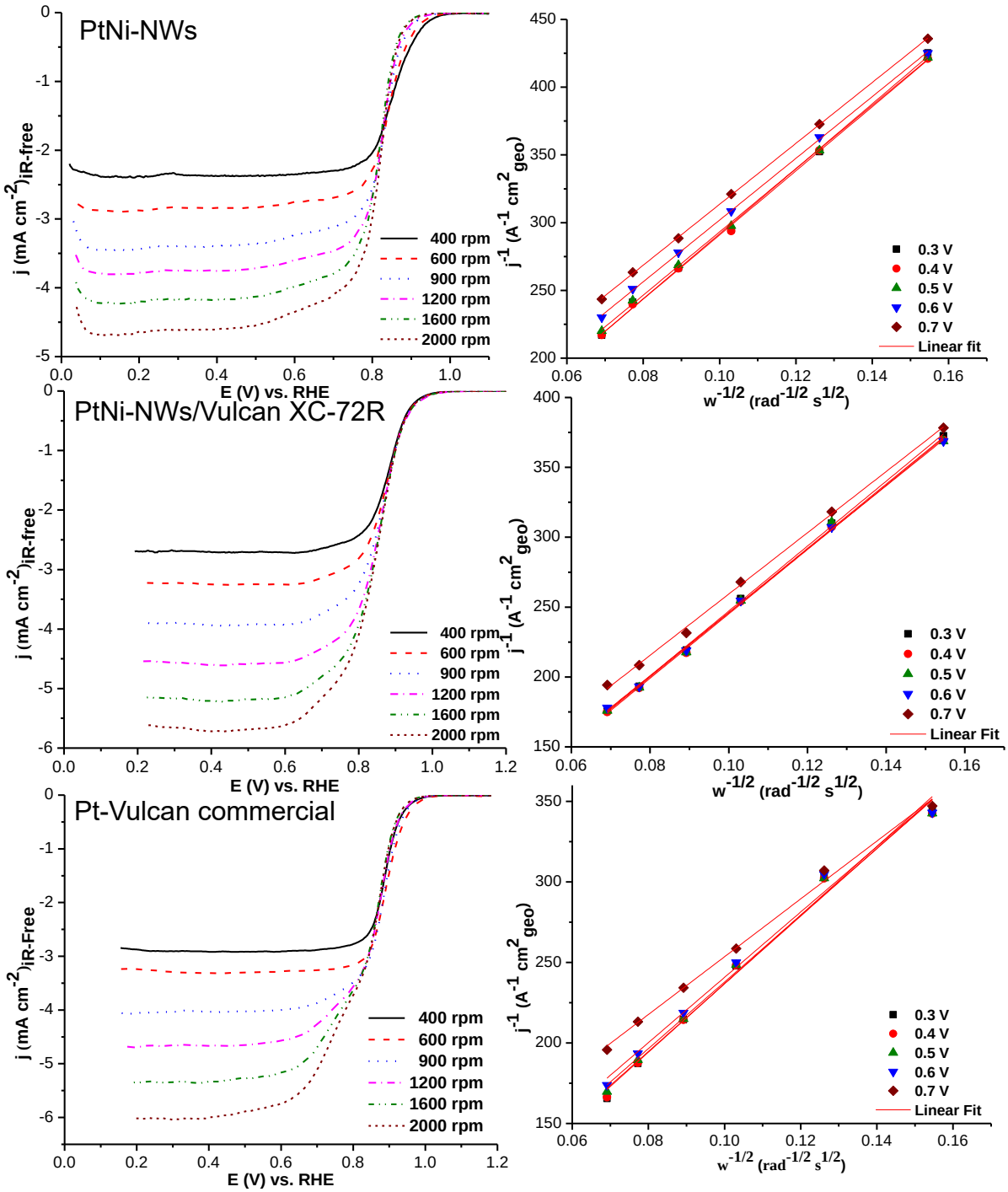

Figure 4.10 Left, oxygen polarization curves using a GC electrode modified with lab-made PtNi-NWs, PtNi-NWs/V and Pt-V commercial at 10 mV/s in 0.1 M KOH. Right**,** Koutecký-Levich plots for the catalysts at different potentials in the Levich analysis region. All plots were obtained controlling the temperature at (25.0 ± 0.1)°C.

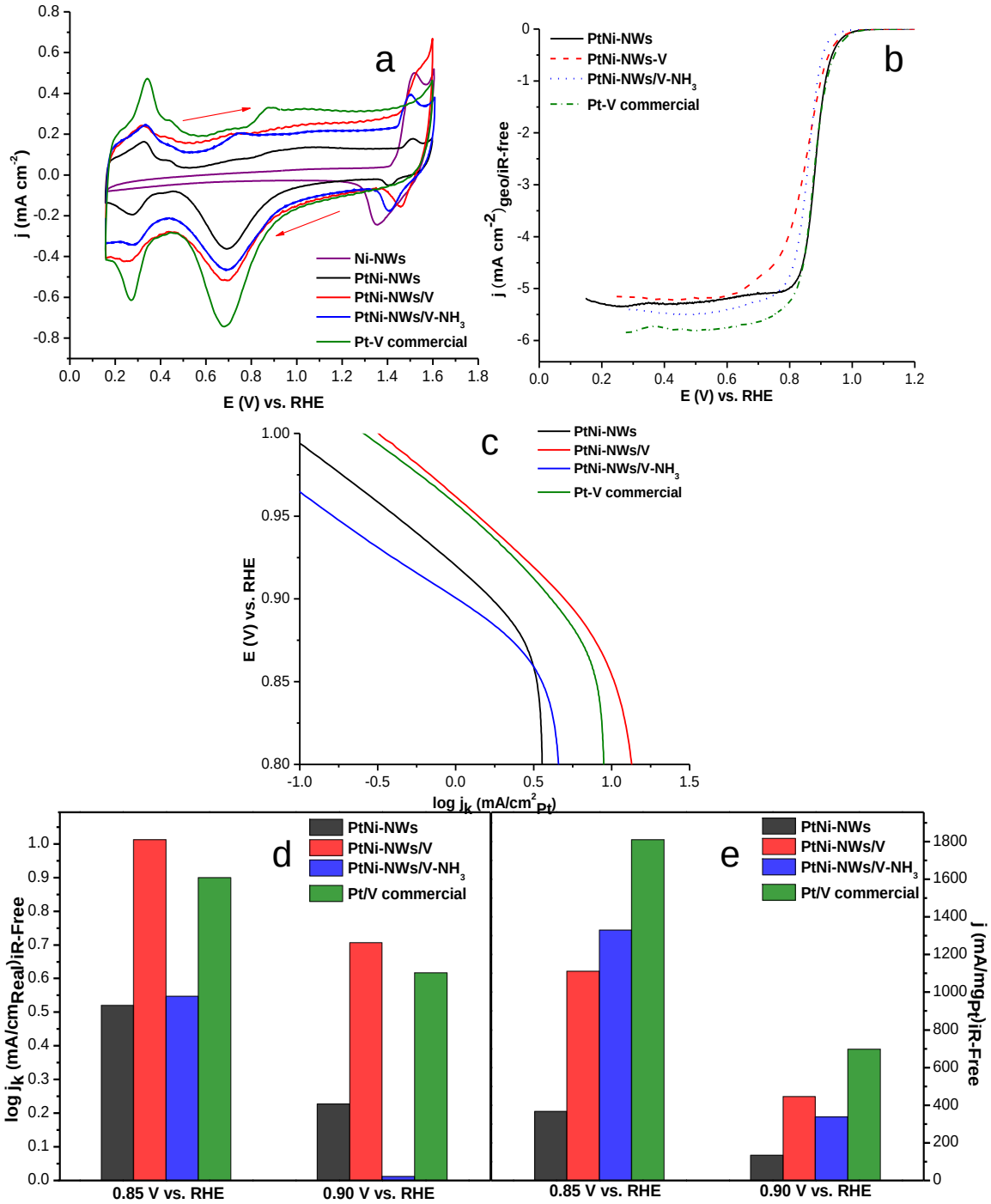

Figure 4.11 (**a**) Cyclic voltammograms of Ni-NWs, PtNi-NWs, PtNi-NWs/V, PtNi-NWs/V-NH_3 and Pt-V commercial at 50 mV/s (**b**) ORR polarization curves of the PtNi-NWs, PtNi-NWs/V, PtNi-NWs/V-NH_3 and commercial Pt-Vulcan at a sweep rate of 10 mV/s and at a rotation rate of 1600 rpm. Both experiments were done in 0.1 M KOH at (25.0 ± 0.1). (**c**) Tafel plots for ORR curves (**b**), (**d**) specific activities for the catalyst tested and (**e**) mass activities for the catalysts tested.

To confirm that our catalyst followed a 4-electron pathway, KL plots **Figure 4.10** were used on the PtNi-NWs and PtNi-NWs/V catalysts, which exhibited 3.8 ± 0.1 electrons and 3.83 ± 0.09 electrons transferred in the ORR, respectively. These results demonstrate that the reaction proceeds through the 4-electron pathway with or without the presence of V. In **Figure 4.11**, CVs of the PtNi-NWs and PtNi-NWs/V CVs show similar peaks and potential regions. The main difference was an increment in the double layer current observed for the PtNi-NWs/V, which could be caused by an increase in the catalyst's surface area due to carbon. These CVs also justify that both Pt and Ni are electrochemically active on the surface because the signal of the electrochemical behavior of the Ni redox process[23,24] ($Ni(OH)_2 \rightarrow NiOOH + H^+ + e^-$) is seen for the oxidation at 1.45 V and reduction at 1.40 V **Figure 4.12** and the shape of the voltammogram in the more negative potentials represents the CV patterns of Pt for hydrogen adsorption-desorption processes (see **Figure S7**).

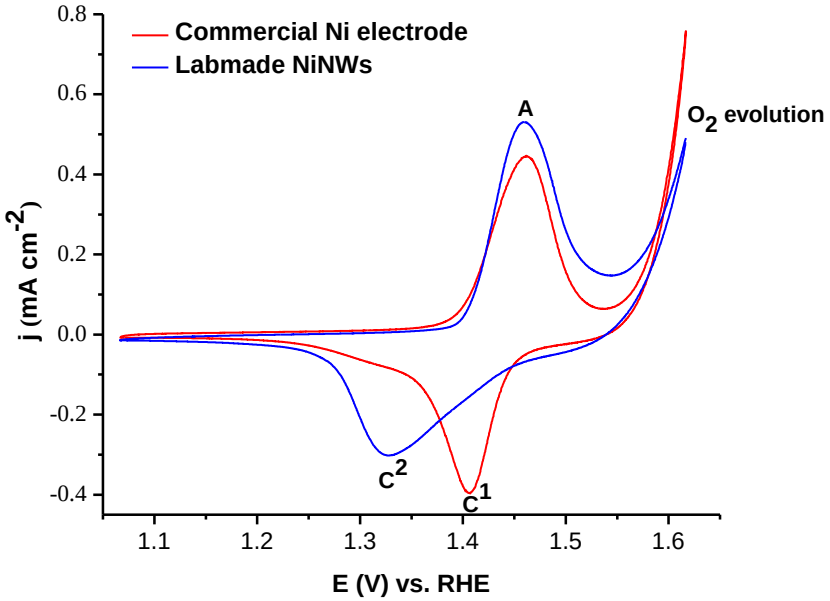

Figure 4.12 Cyclic voltammogram of a commercial Ni electrode (red line) and a lab-made Ni-NWs (blue line) in 0.1 M KOH at 20 mV/s.

Figure 4.12 shows the oxyhydroxide region of Ni in KOH. The anodic peak (A) corresponds to the oxidation of $Ni^{2+}(Ni(OH)_2)$ to $Ni^{3+}(NiOOH)$ via the following reaction:

$$Ni(OH)_2 \rightarrow NiOOH + H^+ + e^-$$

Subsequently, after the O_2 peak, the evolution of H_2O happens at (potentials > 1.55 V vs. RHE). On the backward sweep, the cathodic peaks (C^1 and C^2) correspond to the reduction of Ni oxides.[36,37] The electrochemical behavior of each catalyst varied depending on its composition. CV was studied before any other characterization method in our experiments. To confirm the presence of the Ni-NWs in our final product post-synthesis, the lab-made catalyst was compared with a commercial metallic Ni electrode. **Figure 4.12** shows this comparison, confirming the presence of Ni in the cyclic voltammograms.[37,38]

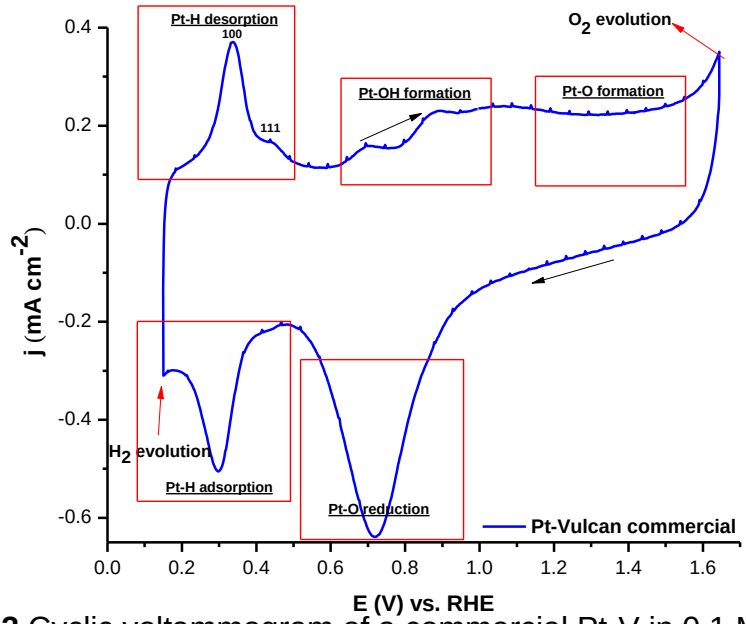

Figure 4.13 Cyclic voltammogram of a commercial Pt-V in 0.1 M KOH at 20 mV/s.

The CVs from Pt-containing catalysts (see **Figure 4.11a**) were normalized by the Pt electrochemical ECSAs calculated from the hydrogen desorption (H_{UPD}) region as it is characterized in **Figure 4.13**.[25] **Figure 4.11b** shows ORR polarization curves for the PtNi catalysts and commercial Pt/V. The limiting diffusion current from each ORR curve in **Figure 4.11b** was used to obtain the Tafel plot shown in **Figure 4.11c** using the kinetic current **Equation 4.4**.

$$j_k = \frac{j_{dif}\ x\ j}{j_{dif} - j}\ x\ \left(\frac{1}{r_f\ x\ A_{geo}}\right) \qquad \textbf{Eq 4.4}$$

Here j_k is the kinetic current density, j_{dif} is the diffusion-limited current density, j is the experimental current density by normalized by the RDE geometric area (A_{geo}) (0.1963 cm^2), r_f is the roughness factor (= Platinum surface area/geometric area).[26]

The metal loadings of each catalyst were adjusted by considering their mass. The Pt loadings were always 12 ug_{Pt}/cm^2 normalized to have 0.0024 mg_{Pt} on GC RDE electrode with a geometric area of 0.1963 cm^2 in each experiment for the PtNi-NWs/V (with and without NH_3) and commercial Pt-V catalysts. For the PtNi-NWs, the Pt loading was 0.0118 mg_{Pt} and, for the Ni-NWs the Ni loading was 0.090 mg_{Ni}. However, when comparing the LSV experiment, shown in **Figure 4.11b**, the PtNi-NWs, Pt-V commercial, PtNi-NWs/V, and PtNi-NWs/V-NH_3 catalysts showed $E_{1/2}$ at 0.89 V, 0.88 V, 0.87 V, and 0.86 V, respectively. Our catalysts have closer ORR current densities to the Pt-V commercial catalyst and a higher $E_{1/2}$ value, see **Table 4.8** for a summary of the results.

Table 4.8 Summary of all catalyst oxygen reduction properties in alkaline

Catalyst	*Mass Loading* $(\mu g/cm^2)_{geo}$	$E_{1/2}$ *(V) vs. RHE*	*Specific activity* $(mA/cm^2)_{Pt}$		*Mass activity* (mA/mg_{Pt})	
			0.90 V	0.85V	0.90 V	0.85V
PtNi-NWs	100	0.89 V	0.23	0.52	133	365
PtNi-NWs/V	100	0.87 V	0.71	1.01	446	1110
PtNi-NWs/V-NH_3	100	0.86 V	0.01	0.55	337	1329
Pt-V commercial	60	0.88 V	0.62	0.90	696	1810

Specific activity, mA/cm^2, values at 0.90 and 0.85 V were estimated by extrapolating the logarithmic values of the Tafel-plot. PtNi-NWs/V was the most active catalyst with 0.707 and 1.01 mA/cm^2_{Real} at 0.90 V and 0.85 V, respectively. Nevertheless, if the results are compared in mass activity, the Pt-V commercial is more active, showing values of 696 and 1,810 mA/mg_{Pt} at 0.90 V and 0.85 V, respectively, compared with the PtNi-NWs/V with 446 and 1110 mA/mg_{Pt}. It seems that in the PtNi-NWs/V catalyst, the Pt is not entirely exposed to the surface. This could be due to the large Pt layer on the NW that was seen in the TEM studies (ca. 10 nm) (see **Figure 4.1f).** When compared with the commercial catalyst that has smaller particle sizes, this translates to better Pt surface interaction in the ORR process for our PtNi-NWs samples. An approach to reduce the Pt layer of the PtNi-NWs catalyst to a smaller thickness could enhance its mass activity and half-wave potential.

4.4.7. Durability experiments

The performance of the PtNi-NWs was evaluated with a durability test where the potential was cycled between 0.60 and 1.00V (see **Figure 4.14**). **Figure 4.15** shows the cyclic voltammograms and O_2 polarization curves for both the PtNi-NWs/V and Pt-V commercial at different steps of the durability test. The cyclic voltammogram of the PtNi-NWs/V before performing the durability test shows the presence of Ni; however, after 5,000 cycles, the region where the Ni oxides cathodic and anodic peaks (ca. 1.55 V and 1.50 V, respectively) are seen exhibits a decrease in current. This may be associated with having less presence of Ni in the middle CV. Similarly, the performance of the catalysts decreases in its $E_{1/2}$ (by 50 mV) after 5,000 cycle testing, as shown in **Figure 4.15b**. After the 10,000 cycles, the Ni oxides cathodic and anodic peaks (ca. 1.55 V and 1.50 V, respectively) are not seen. Similarly, the performance of the catalysts is lost, showing a decrease in its $E_{1/2}$ (by 120 mV) after 10,000 cycles.

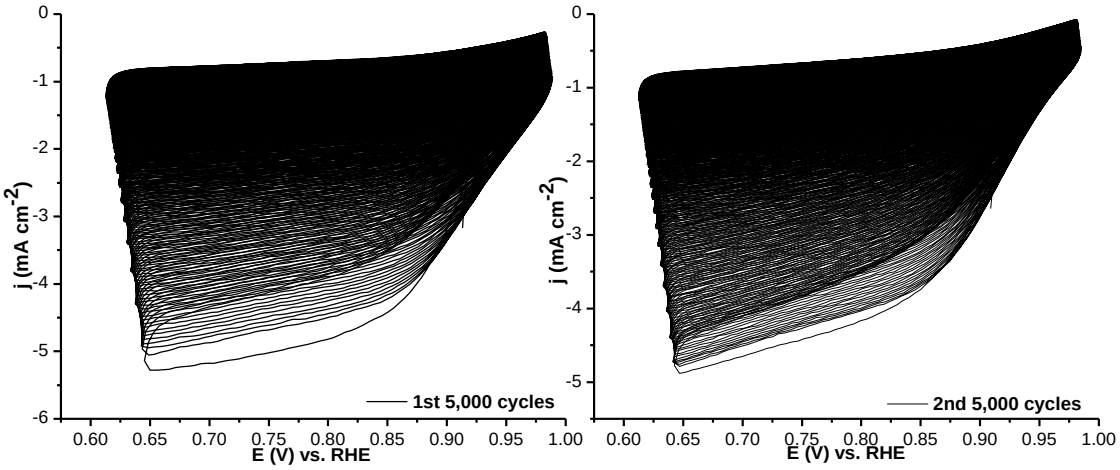

Figure 4.14 Voltammograms of PtNi-NWs/V in the potential window between 0.60 and 1.00 V vs. RHE in 0.1 M KOH for the durability experiments. (**a**) Initially, the solution was purged with oxygen for 15 minutes and then the RDE cycles were done up to cycle 5,000. (**b**) This process was repeated for 5,000 additional potential cycles.

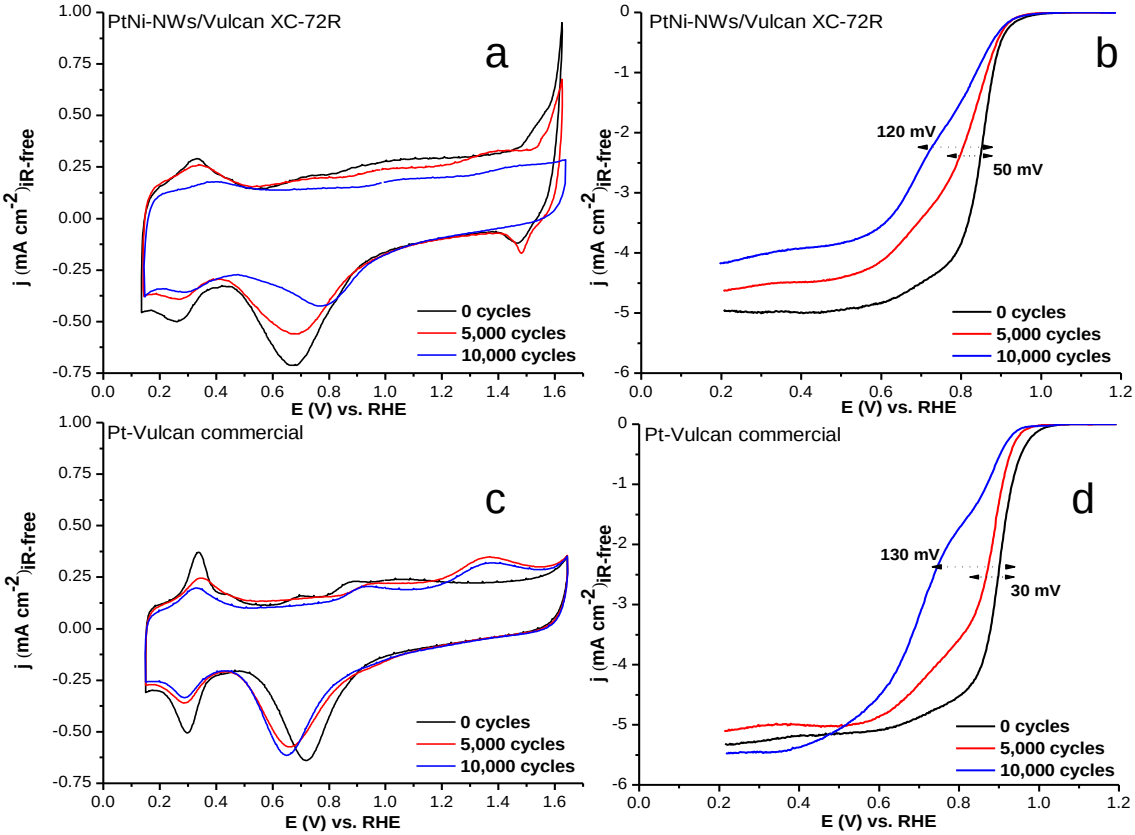

Figure 4.15 Cyclic voltammetry (**a** and **c**) and O_2 polarization curves (**b** and **d**) of PtNi-NWs/V before and after 5,000 and 10,000 cycles in 0.1 M KOH at 100 mV/s with the controlled temperature at 25.0 ± 0.1 °C.

This could happen due to the dissolution of PtNi in KOH.[27,28] This is seen in the CVs of the lab-made catalysts, specifically in the double layer region where it decreases in current as more cycles are performed and the Ni oxides region. When the CV was recorded before the final LSV (10,000 cycles), the peaks associated with Ni oxides were missing (**Figure 6a**). Since the CV shows the process happening at the surface of the working electrode, we could expect that by not seeing Ni oxide peaks and obtaining a decrease of current in the double layer region,[29] PtNi is dissolving in the KOH; alternatively, a portion of the catalyst layer was lost in solution after 10,000 cycles due to a poor ink composition.[30] The

absence of PtNi material in the WE surface will be translated to lower performance in the LSV experiments, which is proven in **Figure 6b**. When our lab-made catalyst was compared with the commercial Pt/V catalyst, the CV also changed along with the experiment and the O_2 polarization curves. The performance of the commercial Pt/V catalyst is lost through cycles (time) by 130 mV (**Figure 4.15d**). The loss in activity is consistent with both materials suggesting that our catalyst behaves similarly to a commercial fuel cell grade Pt-V catalyst in an alkaline medium.

4.4.8. *In situ* X-ray absorption spectroscopy

To understand the local environment of the PtNi catalyst, we performed *in situ* XAS under electrochemical controls. **Figure 4.16** shows XANES spectra for the Ni K-edge and Pt L_3 edge of the Ni-NWs, Pt/V commercial, PtNi-NWs, PtNi-NWs/V and PtNi-NWs/V-NH_3 catalysts, where different potentials (from 1.0 V to 0.3 V) were applied using chronoamperometry (see **Figure 4.17**). Changes in the applied potentials to the electrochemical system were closely monitored with their respective spectroscopic response in the form of changes in the white line intensity of the Ni K and Pt L_3 edges. A trend was observed where at positive applied potentials, the white line intensity peak of Pt L_3 edge increased. In contrast, when more negative potentials were applied (associated with absorption of oxygenated species in Pt 5d band)[31], the white line intensity decreased for all the catalysts examined (see **Figure 4.16 b**, **d**, **f**, and **h**). The Pt/V commercial data in **Figure 4.16b** showed changes in the whiteline intensity similar to our PtNi-NWs catalysts (**Figure 4.16d** and **f**). However, for the PtNi-NWs/V-NH_3 (**Figure 4.16h**) the changes were minor in the white line intensity (<2%). This may be due to a less

active material as seen in the LSV results (see **Figure 4.11b**). This white line changes were also observed when evaluating the Pt L_3 edge catalyst *in situ* XANES response simultaneously at each applied ORR potential (see **Figure 4.18**). As the potential was more negative, the Pt L_3 white line intensity peak of all the catalysts decreased, this is associated to less affinities to OH^- absorbed species in the Pt layer previously seen for Pt catalysts in acidic medium.[32]

This could be related to changes in oxidation states associated with Pt (Pt L_3 edge). These results are expected since negative potentials are associated with the reduction of PtO. If the peak of the Pt L_3 edge white line decreases in the same trend as negative potentials are applied, the system responds to the applied potential. Therefore, Pt actively participates in the O_2 reduction process because the air was purged in the solution as potentials were changed. This experiment was also done using the Ni K edge (see **Figure 4.19 a**, **c**, **e**, and **g**). However, no trend was found between the electrochemical potentials and the white line peak for either catalyst. Similarly, when evaluating the catalyst *in situ* response simultaneously at each potential, there are no changes in the white line peak intensity for the PtNi catalysts in the Ni K edge (see **Figure 4.19**). This reveals that according to the used method, Ni electronic properties are not influenced as potentials are applied while air is purged in the *in situ* cell alkaline medium.

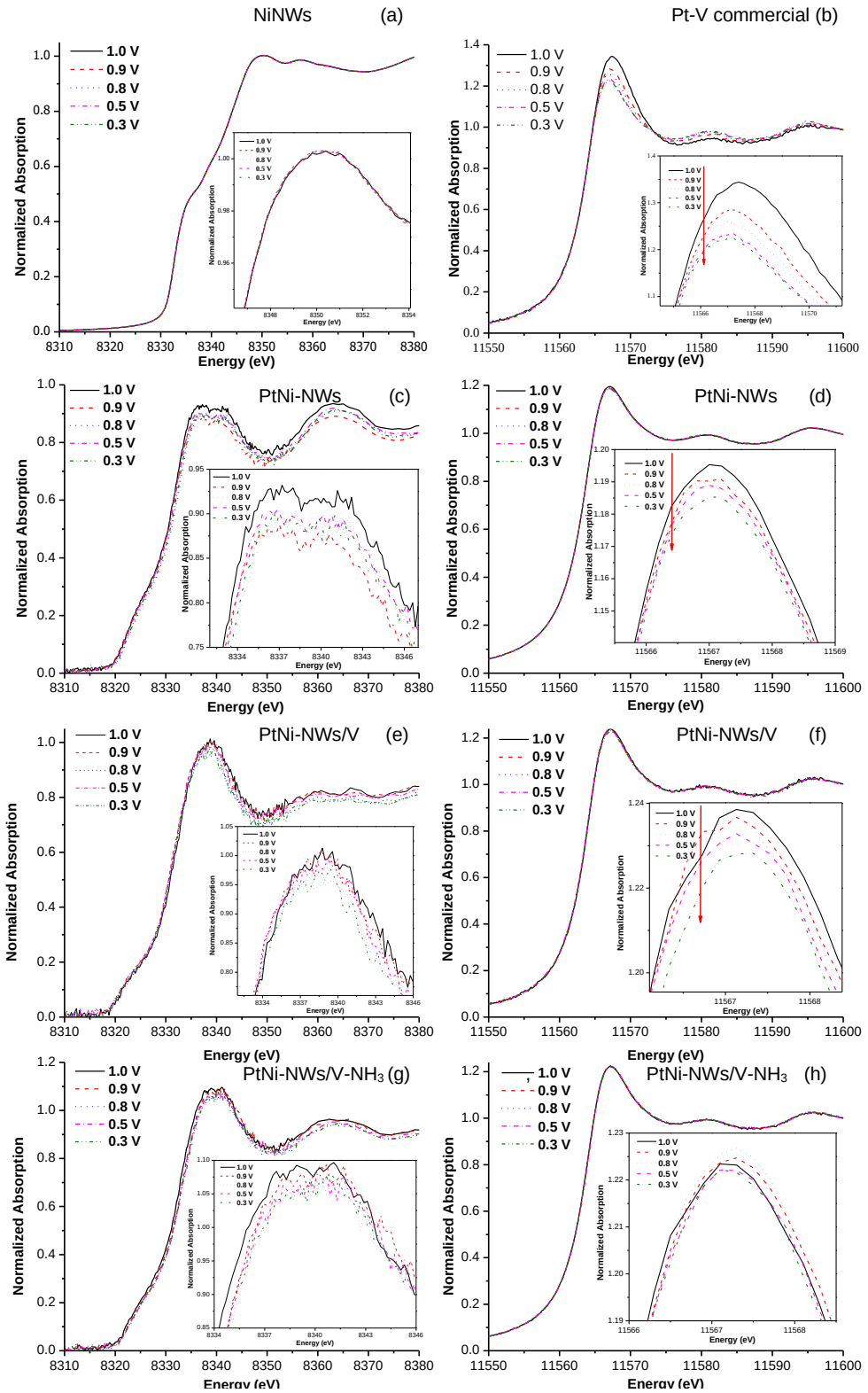

Figure 4.16 *In situ* XANES region of (**a**,**c**,**e**, and **g**) Ni-K energy edge and (**b**, **d**, **f**, and **h**) Pt-L_3 energy edge with different electrochemical applied potentials: (**a** and **b**) Ni-NWs and Pt/V commercial, respectively, (**c** and **d**) PtNi-NWs, (**e** and **f**) PtNi-NWs/V, and (**g** and **h**) PtNi-NWs/V-N.

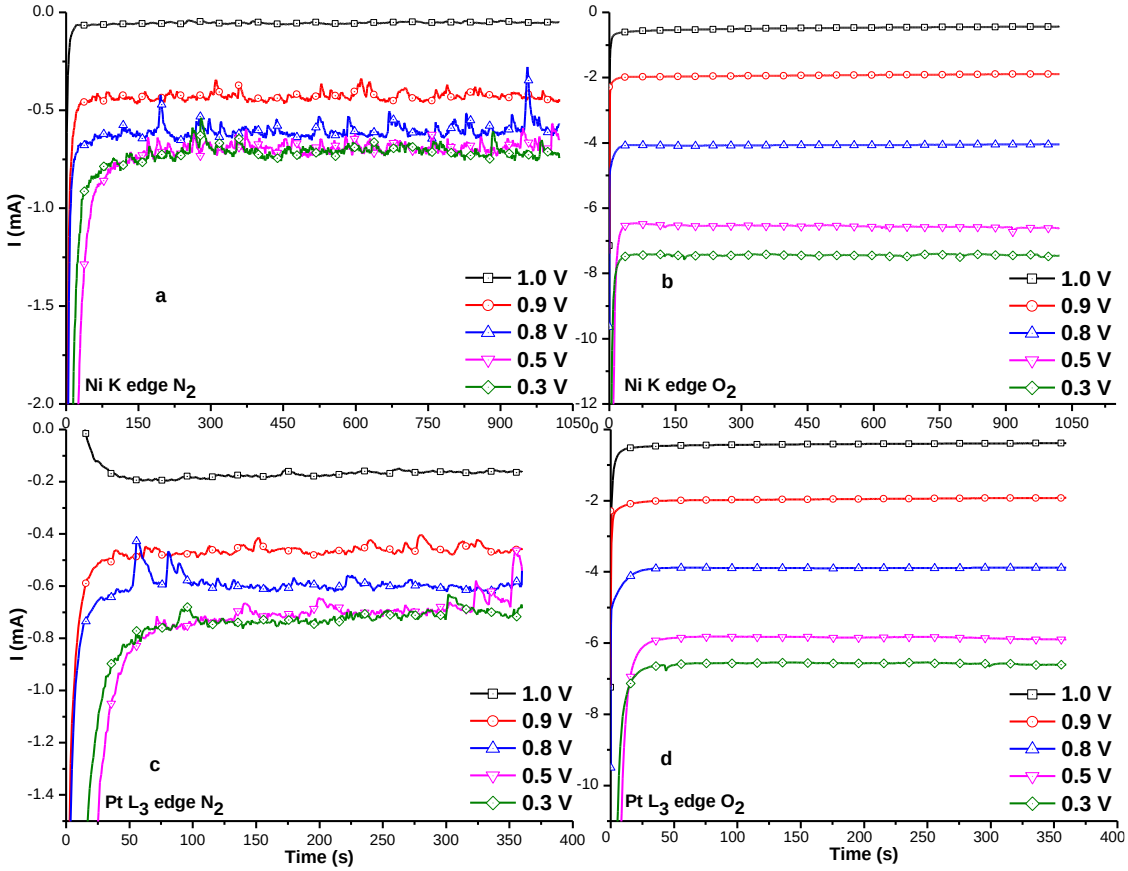

Figure 4.17 Example of chronoamperometries of PtNi-NWs/V in N_2 and O_2, while the *in situ* cell was running XAS experiments. (**a**, **b**) plots while at Ni K energy edge and (**c**, **d**) while at Pt L_3 energy edge. (**a**, **c**) with N_2 purge and (**b**, **d**) with air purge.

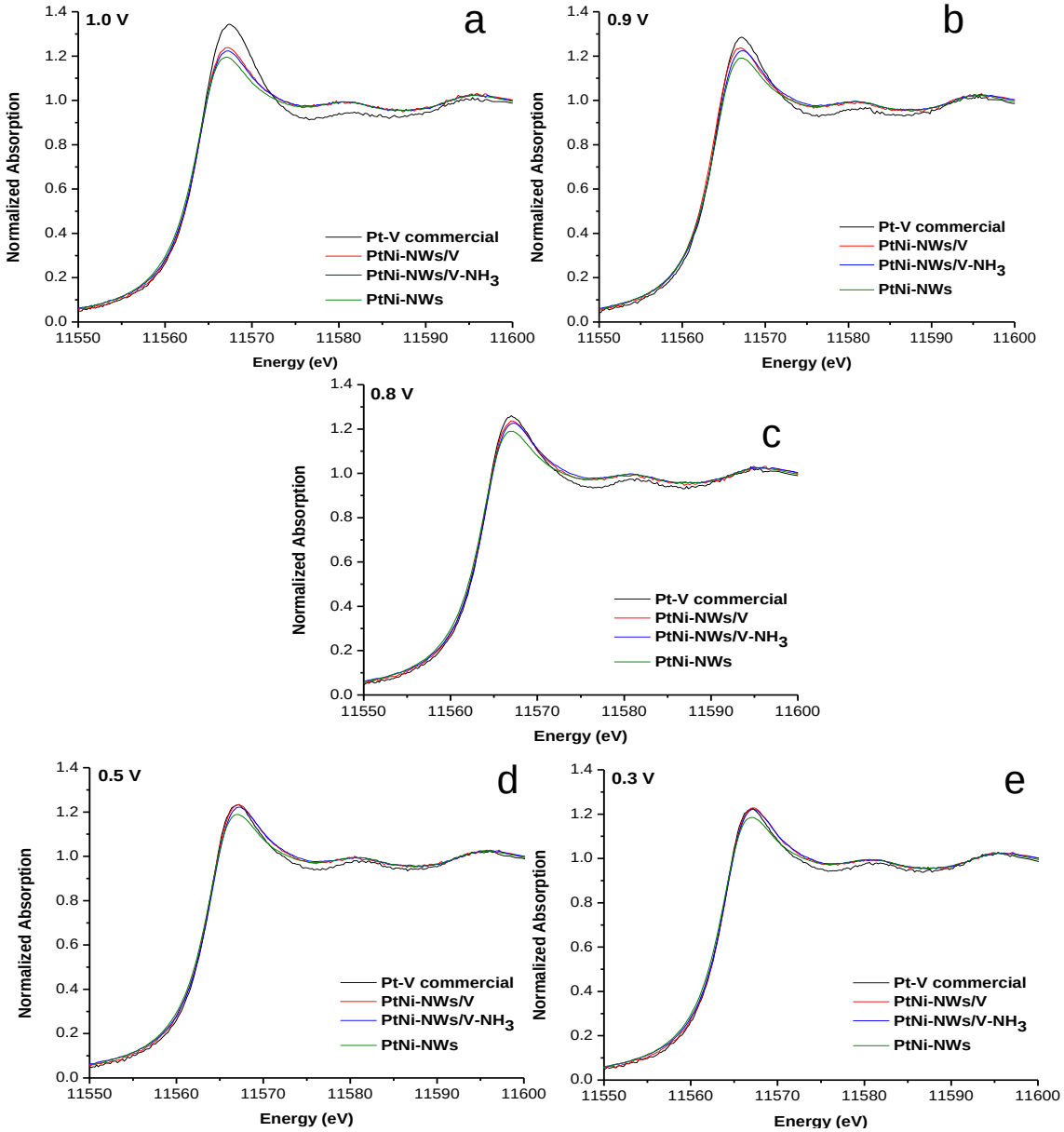

Figure 4.18 *In situ* XANES of PtNi catalysts at the Pt L_3 energy edge while electrochemical potentials were applied to the *in situ* cell setup: (**a**) 1.0 V, (**b**) 0.9 V, (**c**) 0.8 V, (**d**) 0.5 V, and (**e**) 0.3 V vs. RHE.

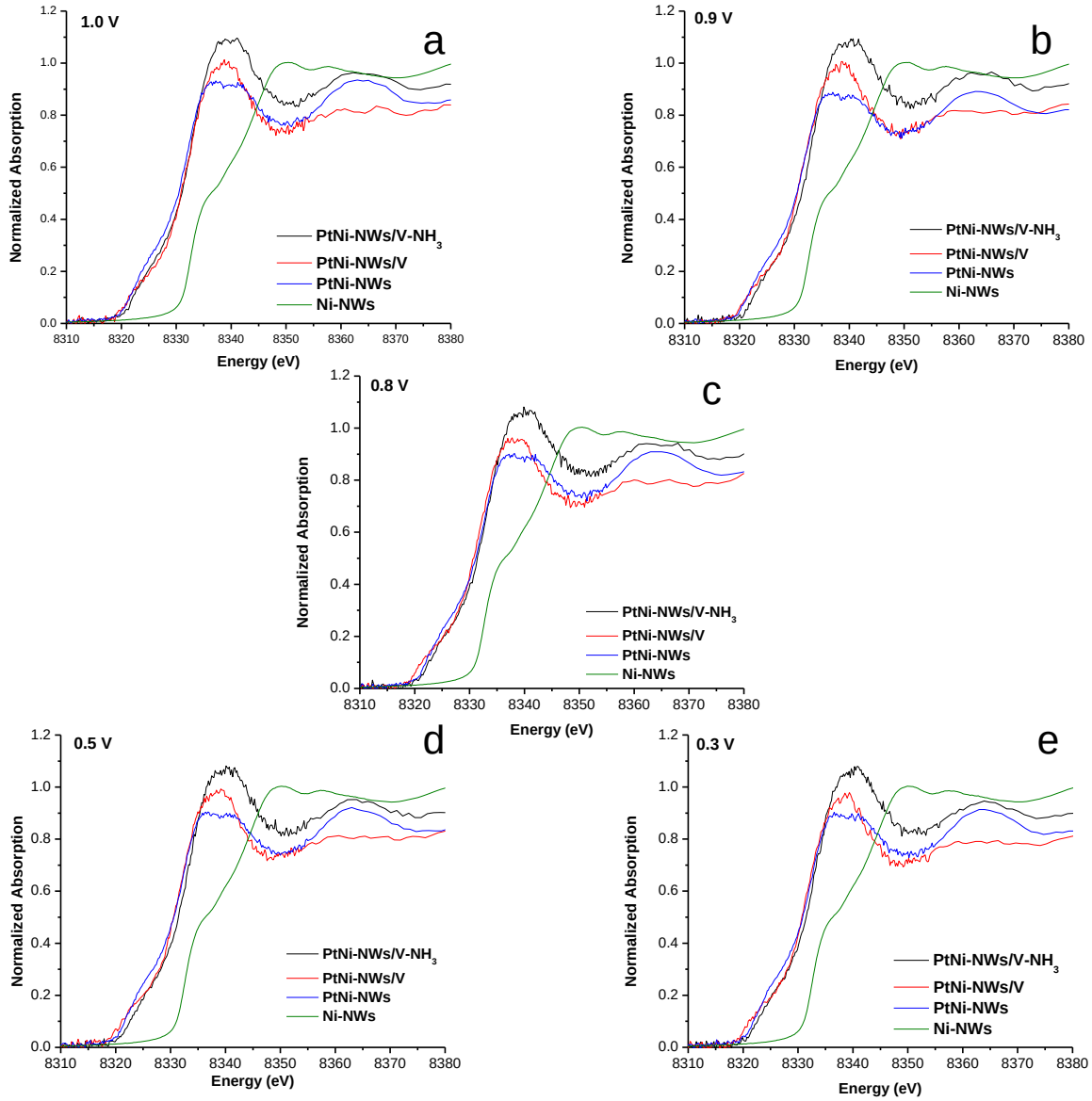

Figure 4.19 *In situ* XANES of PtNi catalysts at the Ni K edge while electrochemical potentials were applied to the *in situ* cell setup: (**a**) 1.0 V, (**b**) 0.9 V, (**c**) 0.8 V, (**d**) 0.5 V, and (**e**) 0.3 V vs. RHE.

The ORR active element in our catalyst is Pt. However, when Pt is alloyed to first-row transition metals (M=Co, Fe or Ni), the Pt-M 5d vacancies are increased compared with having Pt or M alone because M has additional holes in their 5d shell compared with Pt.[33] This effect reduces the interactions of Pt with oxygenated

species (OH^-), providing more actives sites for the interaction of Pt with O_2.[34] *In situ* Extended X-ray Absorption Fine Structure (EXAFS) region Fourier transforms (FT) of the Pt-V commercial and PtNi-NWs/V are presented in **Figure 4.20**. The FT EXAFS of Pt-V commercial has evident changes in the Pt-O distance (ca. 1.6 Å) as potentials were applied to the electrochemical system. The distances read off the FT may have a phase shift, so an apparent value of 1.6 Å may be a distance of 0.2 – 0.5 A longer. However, the PtNi-NWs catalyst showed minimal changes in the Pt-O region. This could be related to no Pt-O interaction, suggesting an alloy interaction of Pt-Ni with O_2.[31] The interaction of Pt-O in PtNi-NWs/V is weaker in all applied potentials with applied 1.0 V, 0.9 V and 0.8 V to Pt-V commercial. This can be associated with Pt oxidation/dissolution inhibition from the PtNi-NWs catalyst.[35]

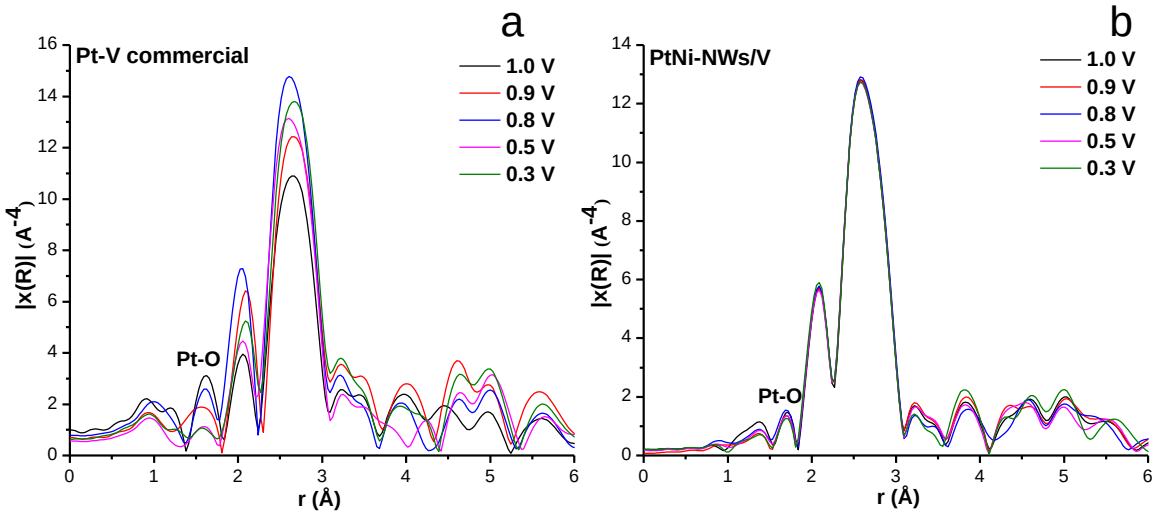

Figure 4.20 Fourier transform of *in situ* electrochemical X-ray absorption spectroscopy (XAS) EXAFS region of (**a**) Pt-V commercial and (**b**) PtNi-NWs/V at applied potentials of 1.0, 0.9, 0.8, 0.5, and 0.3 V vs. RHE in 0.1 M KOH.

Table 4.9 Structural parameters derived from the Pt L_3 edge XANES and EXAFS studying the PtNi-NWs/V

Sample	*Edge*	*Near Neighbor species*	*N*	*R (Å)*	*σ (Å²)*	*E_0 (eV)*
Pt foil	Pt L_3	Pt	12	2.764 ± 0.003	0.0055 ± 0.0002	8.0 ± 0.5
Pt 1.0 V_Air	Pt L_3	Ni	6	2.66 ± 0.03	0.006 ±0.003	7.8 ± 0.3
		Pt	8.05	2.74 ± 0.03	0.0054 ±0.0003	
Pt 0.9 V_Air	Pt L_3	Ni	6	2.66 ± 0.03	0.005 ± 0.003	7.7 ± 0.7
		Pt	8.15	2.74 ± 0.03	0.0054 ± 0.0003	
Pt 0.8 V_Air	Pt L_3	Ni	6	2.65 ± 0.03	0.003 ± 0.003	7.5 ± 0.4
		Pt	8.5	2.75 ± 0.03	0.0054 ± 0.0003	
Pt 0.5 V_Air	Pt L_3	Ni	6	2.66 ± 0.03	0.005 ± 0.003	7.4 ± 0.4
		Pt	8.35	2.74 ± 0.03	0.0055 ± 0.0003	
Pt 0.3 V_Air	Pt L_3	Ni	6	2.66 ± 0.03	0.006 ± 0.004	7.0 ± 0.4
		Pt	8.2	2.75 ± 0.03	0.0054 ± 0.0003	

± = uncertainty

Additionally, when we evaluated the Pt-Pt distances at the Pt L_3 edge, there were no changes with the applied potentials (see **Table 4.9**). However, when we compare the Pt-Pt distance of the *in situ* samples with the Pt foil ex situ samples, the radial distances varied from 2.764 *Å* to 2.744 *Å* (see **Table 4.9**). A lower Pt-Pt bond length (Pt-Pt contraction) is associated with better ORR activity,[36] indicating that PtNi-NWs/V can be further enhanced to provide better catalytic performance and response alkaline medium.

4.5. Conclusions

Thermal reduction and SGD methods were used to synthesize Ni-NWs and PtNi-NWs. The ORR performance of PtNi-NWs/V was examined in 0.1 M KOH by CVs and O_2 polarization curves. The Pt mass loading was lower than DOE MEA guidelines (125 $\mu g_{PGM}/cm^2$) and we still complied with DOE mass activity targets for 2020 (440 mA/mg_{PGM}) with 446 mA/mg_{Pt} at 0.90 V vs. RHE. The use of a temperature-controlled electrochemical cell improved the O_2 polarization curves of our catalyst by ensuring a constant temperature of 25.0 ± 0. 1 °C throughout the experiments. The PtNi-NWs catalyst exhibited a 4-e^- pathway with a value of 3.83 ± 0.09 of electrons calculated according to the KL equation. The specific activity of PtNi-NWs/V was superior to all the catalysts, including the commercial Pt-V. Improvements in the mass activities and $E_{1/2}$ potentials suggest a potential for future use of the PtNi-NW catalysts in AEMFCs. However, the Pt layer thickness at the PtNi-NWs needs to be optimized and the N_2/NH_3 annealing process may enhance the ORR performance as shown in previous publications.[37]

Studies evaluating the relationship of Pt mass loading and the ORR performance (e.g. durability experiments) should be done to guarantee the durability of the catalyst while using less Pt mass in the cathode electrode. *In situ* electrochemical XAS was used to evaluate the electronic properties of Ni and Pt. The studies showed that Pt electronic properties changed when employing electrochemical potentials associated with ORR in alkaline media. As more negative potentials were applied, the Pt L_3 XAS whiteline decreased, indicating a less oxidized catalytic material as previously seen in acid media, suggesting that

in situ Pt electronic properties are similar in alkaline and acid media. The EXAFS data reveal that PtNi is an alloy because the Pt-O peak stayed constant as the electrochemical potentials were applied, suggesting that the interaction with O_2 while ORR is with the whole material (PtNi), not just Pt.

4.6. References

(1) Chang, Y. H.; Lin, T. J.; Wu, Y. C.; Fan, S. W.; Lee, Y. H.; Lai, Y. R. Surfactant-Assisted Galvanic Synthesis and Growth Characteristics of Copper Nanowires. *Inorg. Chem. Front.* **2019**, *6*, 57–62.

(2) Carraro, C.; Maboudian, R.; Magagnin, L. Metallization and Nanostructuring of Semiconductor Surfaces by Galvanic Displacement Processes. *Surf. Sci. Rep.* **2007**, *62*, 499–525.

(3) Li, M.; Zhao, Z.; Cheng, T.; Fortunelli, A.; Chen, C.-Y.; Yu, R.; Zhang, Q.; Gu, L.; Merinov, B. V; Lin, Z. Ultrafine Jagged Platinum Nanowires Enable Ultrahigh Mass Activity for the Oxygen Reduction Reaction. *Science (80-.).* **2016**, *354*, 1414–1419.

(4) Alia, S. M.; Larsen, B. A.; Pylypenko, S.; Cullen, D. A.; Diercks, D. R.; Neyerlin, K. C.; Kocha, S. S.; Pivovar, B. S. Platinum-Coated Nickel Nanowires as Oxygen-Reducing Electrocatalysts. *Acs Catal.* **2014**, *4*, 1114–1119.

(5) Alia, S. M.; Ngo, C.; Shulda, S.; Ha, M.-A.; Dameron, A. A.; Weker, J. N.; Neyerlin, K. C.; Kocha, S. S.; Pylypenko, S.; Pivovar, B. S. Exceptional Oxygen Reduction Reaction Activity and Durability of Platinum–Nickel Nanowires through Synthesis and Post-Treatment Optimization. *ACS Omega* **2017**, *2*, 1408–1418.

(6) Shao, Q.; Lu, K.; Huang, X. Platinum Group Nanowires for Efficient Electrocatalysis. *Small Methods* **2019**, *3*, 1800545.

(7) Krishnadas, K. R.; Sajanlal, P. R.; Pradeep, T. Pristine and Hybrid Nickel Nanowires: Template-, Magnetic Field-, and Surfactant-Free Wet Chemical Synthesis and Raman Studies. *J. Phys. Chem. C* **2011**, *115*, 4483–4490.

(8) Campos-Roldán, C. A.; González-Huerta, R. G.; Alonso-Vante, N. Experimental Protocol for HOR and ORR in Alkaline Electrochemical Measurements. *J. Electrochem. Soc.* **2018**, *165*, J3001–J3007.

(9) Elezović, N. R.; Babić, B. M.; Vračar, L. J. M.; Krstajić, N. V. Oxygen Reduction at Platinum Nanoparticles Supported on Carbon Cryogel in Alkaline Solution. *J. Serbian Chem. Soc.* **2007**, *72*, 699–708.

(10) Campos-Roldán, C. A.; González-Huerta, R. G.; Alonso-Vante, N.

Experimental Protocol for HOR and ORR in Alkaline Electrochemical Measurements. *J. Electrochem. Soc.* **2018**, *165*, J3001–J3007.

(11) Biesinger, M. C.; Payne, B. P.; Lau, L. W. M.; Gerson, A.; Smart, R. S. C. X-Ray Photoelectron Spectroscopic Chemical State Quantification of Mixed Nickel Metal, Oxide and Hydroxide Systems. *Surf. Interface Anal.* **2009**, *41*, 324–332.

(12) Zhang, G.; Yang, D.; Sacher, E. X-Ray Photoelectron Spectroscopic Analysis of Pt Nanoparticles on Highly Oriented Pyrolytic Graphite, Using Symmetric Component Line Shapes. *J. Phys. Chem. C* **2007**, *111*, 565–570.

(13) Ravel, B.; Newville, M. ATHENA, ARTEMIS, HEPHAESTUS: Data Analysis for X-Ray Absorption Spectroscopy Using IFEFFIT. *J. Synchrotron Radiat.* **2005**, *12*, 537–541.

(14) Jia, F. L.; Zhang, L. Z.; Shang, X. Y.; Yang, Y. Non-Aqueous Sol–Gel Approach towards the Controllable Synthesis of Nickel Nanospheres, Nanowires, and Nanoflowers. *Adv. Mater.* **2008**, *20*, 1050–1054.

(15) Park, K.-W.; Choi, J.-H.; Kwon, B.-K.; Lee, S.-A.; Sung, Y.-E.; Ha, H.-Y.; Hong, S.-A.; Kim, H.; Wieckowski, A. Chemical and Electronic Effects of Ni in Pt/Ni and Pt/Ru/Ni Alloy Nanoparticles in Methanol Electrooxidation. *J. Phys. Chem. B* **2002**, *106*, 1869–1877.

(16) Deivaraj, T. C.; Chen, W.; Lee, J. Y. Preparation of PtNi Nanoparticles for the Electrocatalytic Oxidation of Methanol. *J. Mater. Chem.* **2003**, *13*, 2555–2560.

(17) Jiang, Q.; Jiang, L.; Wang, S.; Qi, J.; Sun, G. A Highly Active PtNi/C Electrocatalyst for Methanol Electro-Oxidation in Alkaline Media. *Catal. Commun.* **2010**, *12*, 67–70.

(18) Jia, Q.; Zhao, Z.; Cao, L.; Li, J.; Ghoshal, S.; Davies, V.; Stavitski, E.; Attenkofer, K.; Liu, Z.; Li, M.; Duan, X.; Mukerjee, S.; Mueller, T.; Huang, Y. Roles of Mo Surface Dopants in Enhancing the ORR Performance of Octahedral PtNi Nanoparticles. *Nano Lett.* **2018**, *18*, 798–804.

(19) Fu, X.-Z.; Liang, Y.; Chen, S.-P.; Lin, J.-D.; Liao, D.-W. Pt-Rich Shell Coated Ni Nanoparticles as Catalysts for Methanol Electro-Oxidation in Alkaline Media. *Catal. Commun.* **2009**, *10*, 1893–1897.

(20) Holloway, P. H. Chemisorption and Oxide Formation on Metals: Oxygen-Nickel Reaction. *J. Vac. Sci. Technol.* **1980**, *18*, 653–659.

(21) Lambers, E. S.; Dykstal, C. N.; Seo, J. M.; Rowe, J. E.; Holloway, P. H. Room-Temperature Oxidation of Ni(110) at Low and Atmospheric Oxygen Pressures. *Oxid. Met.* **1996**, *45*, 301–321.

(22) Thompson, S. T.; Wilson, A. R.; Zelenay, P.; Myers, D. J.; More, K. L.; Neyerlin, K. C.; Papageorgopoulos, D. ElectroCat: DOE's Approach to PGM-Free Catalyst and Electrode R&D. *Solid State Ionics* **2018**, *319*, 68–76.

(23) Grdeń, M.; Klimek, K. EQCM Studies on Oxidation of Metallic Nickel Electrode in Basic Solutions. *J. Electroanal. Chem.* **2005**, *581*, 122–131.

(24) Medway, S. L.; Lucas, C. A.; Kowal, A.; Nichols, R. J.; Johnson, D. In Situ Studies of the Oxidation of Nickel Electrodes in Alkaline Solution. *J. Electroanal. Chem.* **2006**, *587*, 172–181.

(25) Garsany, Y.; Baturina, O. A.; Swider-Lyons, K. E.; Kocha, S. S. Experimental Methods for Quantifying the Activity of Platinum Electrocatalysts for the Oxygen Reduction Reaction. *Anal. Chem.* **2010**, *82*, 6321–6328.

(26) Mayrhofer, K. J. J.; Strmcnik, D.; Blizanac, B. B.; Stamenkovic, V.; Arenz, M.; Markovic, N. M. Measurement of Oxygen Reduction Activities via the Rotating Disc Electrode Method: From Pt Model Surfaces to Carbon-Supported High Surface Area Catalysts. *Electrochim. Acta* **2008**, *53*, 3181–3188.

(27) Shokhen, V.; Zysler, M.; Shviro, M.; Zitoun, D.; Chatenet, M. Carbon-Supported PtNi Nanocrystals for Alkaline Oxygen Reduction and Evolution Reactions: Electrochemical Activity and Durability upon Accelerated Stress Tests. *ACS Appl. Energy Mater.* **2020**, *3*, 8858–8870.

(28) Schalenbach, M.; Kasian, O.; Ledendecker, M.; Speck, F. D.; Mingers, A. M.; Mayrhofer, K. J. J.; Cherevko, S. The Electrochemical Dissolution of Noble Metals in Alkaline Media. *Electrocatalysis* **2018**, *9*, 153–161.

(29) Labata, M. F.; Li, G.; Ocon, J.; Chuang, P.-Y. A. Insights on Platinum-Carbon Catalyst Degradation Mechanism for Oxygen Reduction Reaction in Acidic and Alkaline Media. *J. Power Sources* **2021**, *487*, 229356.

(30) Shinozaki, K.; Zack, J. W.; Pylypenko, S.; Pivovar, B. S.; Kocha, S. S. Oxygen Reduction Reaction Measurements on Platinum Electrocatalysts Utilizing Rotating Disk Electrode Technique: II. Influence of Ink Formulation, Catalyst Layer Uniformity and Thickness. *J. Electrochem. Soc.* **2015**, *162*, F1384–F1396.

(31) Mukerjee, S. Role of Structural and Electronic Properties of Pt and Pt Alloys on Electrocatalysis of Oxygen Reduction. *J. Electrochem. Soc.* **1995**, *142*, 1409–1422.

(32) Antolini, E.; Salgado, J. R. C.; Giz, M. J.; Gonzalez, E. R. Effects of Geometric and Electronic Factors on ORR Activity of Carbon Supported Pt–Co Electrocatalysts in PEM Fuel Cells. *Int. J. Hydrogen Energy* **2005**, *30*, 1213–1220.

(33) Toda, T.; Igarashi, H.; Uchida, H.; Watanabe, M. Enhancement of the Electroreduction of Oxygen on Pt Alloys with Fe, Ni, and Co. *J. Electrochem. Soc.* **1999**, *146*, 3750–3756.

(34) García-Contreras, M. A.; Fernández-Valverde, S. M.; Basurto-Sánchez, R. Investigation of Oxygen Reduction in Alkaline Media on Electrocatalysts

Prepared by the Mechanical Alloying of Pt, Co, and Ni. *J. Appl. Electrochem.* **2015**, *45*, 1101–1112.

(35) Song, L.; Liang, Z.; Nagamori, K.; Igarashi, H.; Vukmirovic, M. B.; Adzic, R. R.; Sasaki, K. Enhancing Oxygen Reduction Performance of Pt Monolayer Catalysts by Pd (111) Nanosheets on WNi Substrates. *ACS Catal.* **2020**, *10*, 4290–4298.

(36) Kaito, T.; Tanaka, H.; Mitsumoto, H.; Sugawara, S.; Shinohara, K.; Ariga, H.; Uehara, H.; Takakusagi, S.; Asakura, K. In Situ X-Ray Absorption Fine Structure Analysis of PtCo, PtCu, and PtNi Alloy Electrocatalysts: The Correlation of Enhanced Oxygen Reduction Reaction Activity and Structure. *J. Phys. Chem. C* **2016**, *120*, 11519–11527.

(37) Kuttiyiel, K. A.; Sasaki, K.; Choi, Y.; Su, D.; Liu, P.; Adzic, R. R. Nitride Stabilized PtNi Core–Shell Nanocatalyst for High Oxygen Reduction Activity. *Nano Lett.* **2012**, *12*, 6266–6271.

Chapter 5. **Exploring the RoDSE methodology: Co, Ni and Cu Synthesis as Catalysts precursors for the Oxygen Reduction Reaction in Alkaline Medium**

5.1. Abstract

In this study, we synthesized first-row transition metal catalysts (M= Ni,Co and Cu)—with the RoDSE technique—supported on V. We were able to electrodeposit Ni and Co on V using an electrochemical potential of -0.75V vs. RHE and -0.80V vs. RHE to electrodeposit Cu on V applying the RoDSE methodology in 0.1 M $KClO_4$. These M/V catalysts were modified with a Pt precursor via spontaneous SGD and we obtained Pt-M/Vulcan XC-72R to catalyze the ORR in an alkaline medium. First, we tested the M/V for the OER and Ni/V provided the lowest overpotential with 450 mV vs. RHE at 10 mA/cm^2_{disk} in 0.1 M KOH. We also performed oxygen polarization to characterize the electrochemical activity towards oxygen reduction in an alkaline medium. Our results indicated that under controlled temperature (25.0°C), a mass loading of 100 mg/cm^2 on a GC rotating electrode and at 1,600 rpm the electrocatalysts revealed good performance. The PtCo-V showed higher mass activity with 8 (A/mg^{-1}_{Pt}) vs. RHE, compared with commercial Pt/Vulcan XC-72R.

5.2. Introduction

Cabrera's group has deeply studied the RoDSE methodology. One of the benefits of this method is that scale-up synthesis could be obtained, providing a fluent transition from RDE to the membrane electrode assembly (MEA). Cabrera's group has successfully synthesized Pt[1], Pd[2,3], Au[4], Ag[5] and Fe[6] nanoparticles supported on different carbon supports for energy conversion applications. However, first-row transition metals have not been thoroughly explored. We recognize that the synthesis of first-row transition metals and the addition of a low Pt loading precursor can provide an accessible commercialization path while maintaining performance and activity. This work aimed to study the bulk electrodeposition of M (Ni, Co and Cu) NPs on carbon V support in an acidic medium. We tested their activity for OER, then for ORR after they were modified by a low amount of Pt precursor using the spontaneous SGD. The resulting PtM/V nanoparticles had a ca. 2-3 % Pt w/w%—low loading—and demonstrated superior mass activity than a Pt/V 20% commercial catalyst.

5.3. Research design and methods

5.3.1. Catalyst Synthesis

The synthesis of the PtM/V was divided into two steps (1) The M were electrodeposited on a dispersion consisting of 50 mg of V and 20 mL of 0.1 M $KClO_4$ (GFS Chemicals), using the RoDSE technique—where an electrochemical potential is applied to a carbon support dispersion while being rotated— applying -0.75 V versus RHE for Ni and Co and -0.80 V versus RHE for Cu using a RDE setup at 1,200 rpm in 0.1 M $KClO_4$.[1] (2) Modified the M/V with H_2PtCl_6 to obtain the PtM/V electrocatalysts.

5.3.1.1.Preparation of the Ni, Co and Cu electrocatalysts

For the (1) step, the V dispersion was sonicated for 1 hour to get a highly dispersed slurry. Then, the slurry was transferred to the center of a closed three-compartment electrochemical cell using a RDE (Pine Research Instruments) setup. In the middle compartment, a GC rotating electrode was used as a WE, at the right compartment, an RHE as a RE and in the left compartment, a high surface area platinum as the counter electrode CE **Figure 5.1.** Subsequently, each M synthesis was done individually using an aqueous 5 mM solution, depending on the M precursor ($NiCl_2$, $CoCl_2{\cdot}6H_2O$ and $CuCl_2$). A 2.00 mL aliquot of the 5 mM M precursor solution was added to the middle compartment of the cell and then purged with UHP N_2 while rotating the glassy carbon RDE at 1,200 rpm. A constant purge was maintained inside the cell and the desired electrochemical potential was applied for 1 hour (-0.75 V versus RHE for the Ni and Co and -0.80 V versus RHE for Cu). This step was repeated three additional times in intervals of one hour, for

four hours total and 8 mL of M precursor. The remaining slurry was filtered using a vacuum pump filter system (0.45µm Nylon Membrane) and washed vigorously with deionized water. The resulting material was vacuum dried at 40°C for 24 hours. Then, the product was recovered and grounded by hand using a quartz mortar to obtain the final powder material.

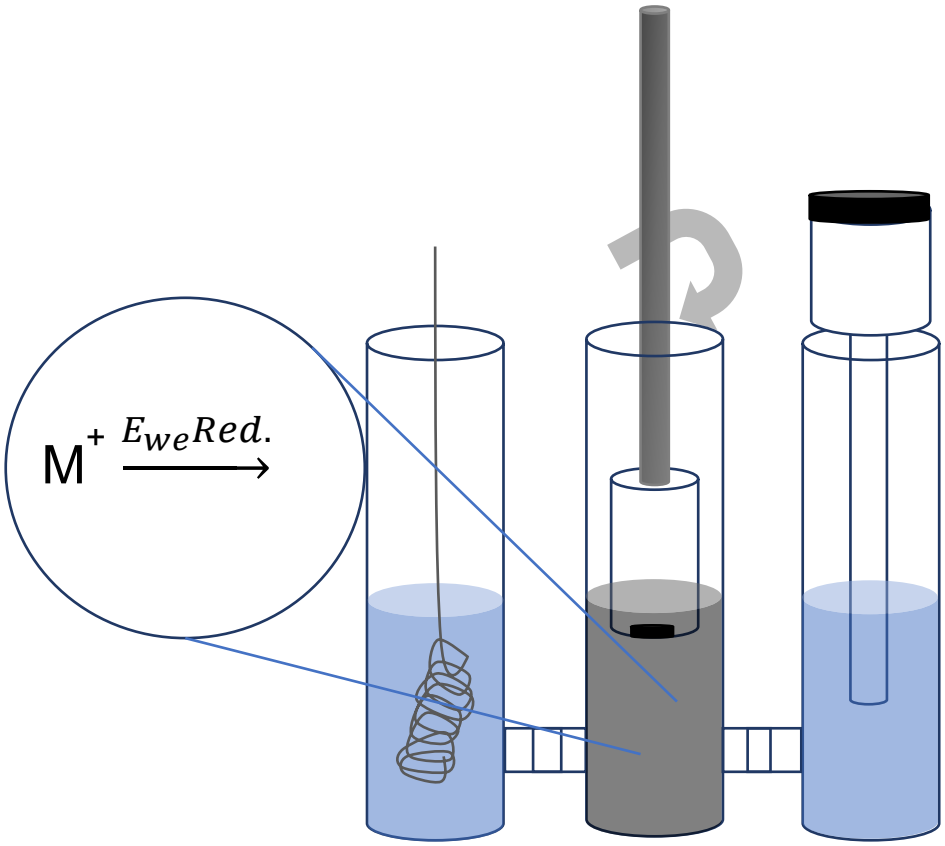

Figure 5.1 RoDSE methodology scheme using a three-electrode electrochemical setup.

5.3.1.2. Preparation of the PtNi, PtCo and PtCu electrocatalysts

For the second step (2), the M/V powders were used to obtain the Pt-M/V electrocatalysts. 20 mg of M/V was placed inside a round bottom flask of 50 mL with 20 mL of deionized water. This flask was heated at 95°C using an oil bath and a reflux setup. A mass stoichiometric 3:1 Pt to M addition was done using a 10 mM H_2PtCl_6. The calculated Pt amount was divided by a factor of ten and added ten times in intervals of 1 minute to the bottom flask to start the SGD and stirred for 2 hours. The resulting Pt-M/V electrocatalysts were recovered following step (1) until obtained in powder form.

5.3.2. Physical characterization

First, the electrocatalysts' crystalline structure was characterized with XRD. A Rigaku SmartLab X-Ray diffractometer assembled with a Cu K_α radiation (λ = 1.54 Å) was used. The 2Θ range was scanned between 10 and 100° at a rate of 0.02°s^{-1}. The smart lab software was used to acquire the data and background correction. Origin software was used for further peak processing and smoothness of the signals using the Savitzky-Golay filter.

The structural morphology of the as-prepared samples was confirmed using HR-TEM with a 200 kV JEOL JEM 2100F instrument of the Center for Functional Nanomaterials (CFN) at Brookhaven National Laboratory (BNL).

The metal concentration was determined using an Optima 8000 Perkin Elmer ICP – OES with standard plasma parameters, shown in **Table 4.2** The

metals were dissolved following a digestion procedure. Six samples of ca. 3 mg were digested with 10 mL aqua regia and heated to simmering until ca. 0.5 mL remained. After cooling down to room temperature, the dissolved metals were reconstituted with 2% HNO_3 solution using a quartz filter.

5.3.3. Electrochemical characterizations

The use of CV characterized the electrocatalysts after the RoDSE methodology and the SGD. We used a typical electrochemical setup consisting of a three-electrode assembly. The setup was composed of GC WE—cleaned before every experiment by polishing the GC surface with alumina micro-polish (Buehler) (1.0, 0,5 and 0.03) µm and pure water, in an eight-shape pattern—Ag/AgCl sat. KCl or a mercury oxide (HgO/Hg) RE, and a platinum wire as AE using a biologic V30 potentiostat and a RDE setup.

For the electrochemical cleaning, the GC electrode was cycled at the potential window of 1.0 - 1.6 V vs. RHE at (100, 50 and 20) mV/s in 0.1 M KOH. Then, an ink dispersion— 8:2:0.2 volume ratio of pure water, isopropanol (Sigma Aldrich) and Nafion (10% solution in alcohol, Sigma Aldrich) respectively— of the electrocatalyst was sonicated for a minimum of 30 minutes. An aliquot of 10 µL was drop cast on the GC electrode and dried using an IR lamp. Then, the electrode was left at ambient temperature. To finish, a CV was obtained at the Pt potential window from 0.1 to 1.2 V vs. RHE at a scan rate of 25 mV/s in argon saturated 0.1 M KOH.

5.3.4. Rotating disk experiments

Before RDE, the solution (0.1 M KOH) was saturated using argon. Later, LSV measurements were done to lower the capacitive currents, starting at 1.2 V and finishing at 0 V vs. RHE at a scan rate of 10 mV/s and 1,600 rpm. An additional LSV was acquired at the same potential window, scan rate and rpm, while O_2 saturated the 0.1 M KOH. The KL plots were acquired at: 400, 625, 900, 1225, 1600 and 2025 rpm. Then, the limiting currents of these curves were obtained and used to calculate the number of electrons transferred by applying the KL and Levich equations **Equations 4.2** and **4.3**.

Accelerated durability experiments were done to test the performance of the electrocatalysts for 30 K CV cycles under reaction conditions. The following procedure was followed: (1) A CV was obtained under an argon environment using the Pt potential window at a scan rate of 25 mV/s. (2) Both argon and O_2 LSVs were recorded as described in the RDE section. (3) 10,000 CV cycles between 0.6 and 0.95 V vs. RHE were recorded at a scan rate of 100 mV/s. (4) Steps (1), (2) and (3) were repeated two additional times.

To do the OER experiments, a LSV was run starting at 1.1 V and finishing at 1.7 V vs RHE while O_2 saturated the 0.1 M KOH solution at 10 mV/s and 1,600 rpm. The overpotential was calculated considering the ORR redox potential (1.23 V vs. SHE) and the potential obtained at 10 mA/cm^2 considering the geometric area of the GC RDE electrode (0.1963 cm^2).

5.3.5. Ex situ XAS electrochemical experiments

XAS experiments were done at beamline 7-BM QAS at BNL's NSLS-II. The Pt L_3 edge data were collected in fluorescence mode using a PIPS detector. Further data processing—calibration, normalization, fittings— was done using the IFEFFIT package (ATHENA and ARTEMIS).[7]

5.3.6. *In situ* XAS electrochemical experiments

The PtCo/V and the commercial Pt/V electrocatalysts were tested for *in situ* XAS electrochemical experiments. The same beamline described in the ex situ XAS procedure and data processing were used. A three-electrode *in situ* electrochemical cell was used and we followed the same procedure described in chapter 3 section 3.4.

5.4. Results and discussion

5.4.1. RoDSE synthesis parameters

The reduction potential of the electrocatalysts was found using homogeneous electrochemical experiments. The electrolyte plays a crucial part when doing electrodeposition experiments. This is mainly related to the pH and electrochemical potential relationship. Under applied electrochemical potentials, different electroactive species are more stable at different pH conditions. The reduction of Ni at the pH range of 0-14 occurs between ca. -0.5 and -3.0 V versus SHE.[8] However, there is competition with the hydrogen reduction reaction at these low potentials. Nickel gets precipitates at pH values higher than 6.8 and it has been found that pH 4 is an optimal value for its electrodeposition.[9] The nickel precursor was dissolved in 0.1 M $KClO_4$ and a CV at 10 mV/s was run between the potential range of -1.0 V and 1.7 V versus RHE to find a reduction process associated with Ni **Figure 5.2a**. In this CV the evolution of oxygen is seen at ca. 1.2 V and when reversing the scan, a reduction process starts to occur at ca. -0.75 V, ultimately resulting in a significant drop in current associated with the reduction of hydrogen. The reduction of hydrogen can be associated with the reduction of Ni[10]. Similarly, we employed the same experimental procedure to find the reduction potential of the Co and Cu **Figure 5.2b** and **Figure 5.2c** resulting in -0.75V for Co and -0.80 V for Cu. These reduction potentials were used to electrodeposit the electrocatalysts on a high surface are V support with the RoDSE methodology **Figure 5.3**. Then, using SGD we obtained the final electrocatalysts consisting of PtM/V.

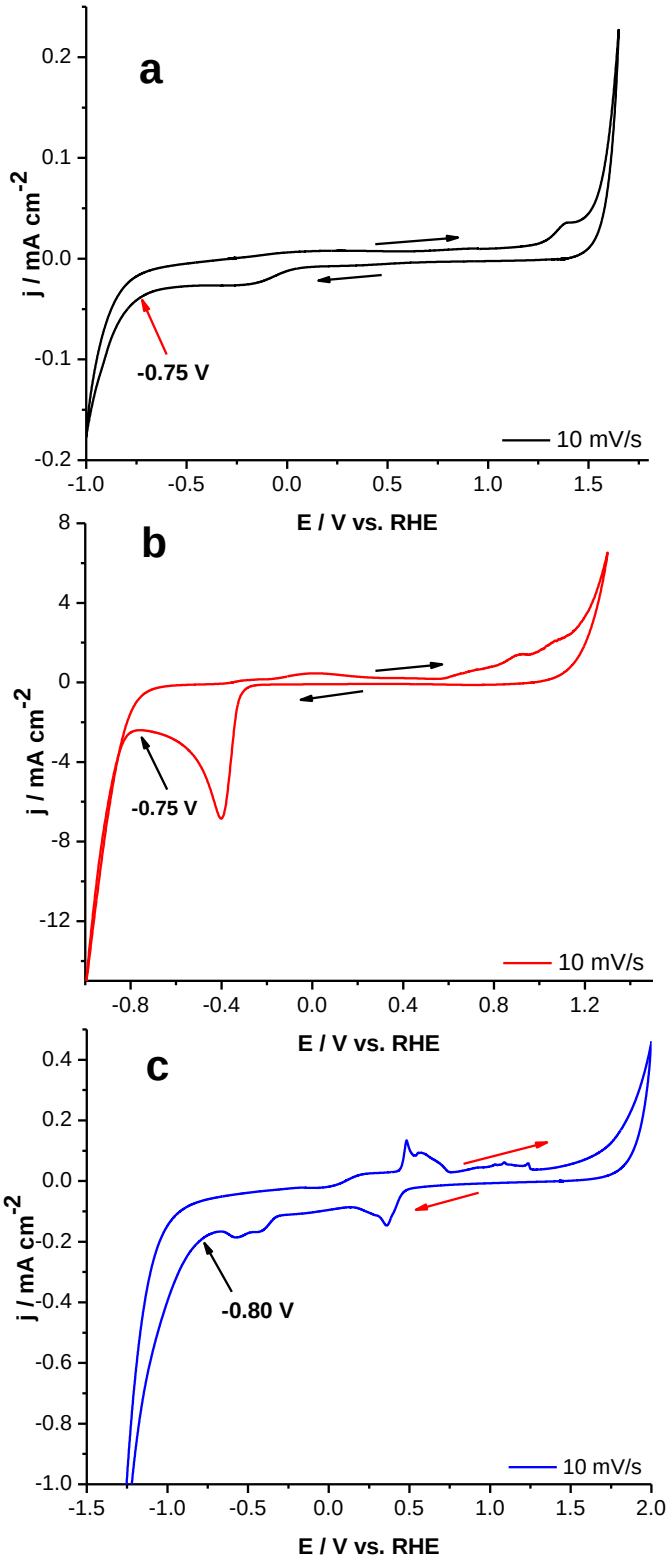

Figure 5.2 Cyclic voltammograms to determine the reduction potentials of (a) Ni using $NiCl_2$ (b) Co using $CoCl_2$ and (c) Cu using $CuCl_2$ all in 0.1M $KClO_4$.

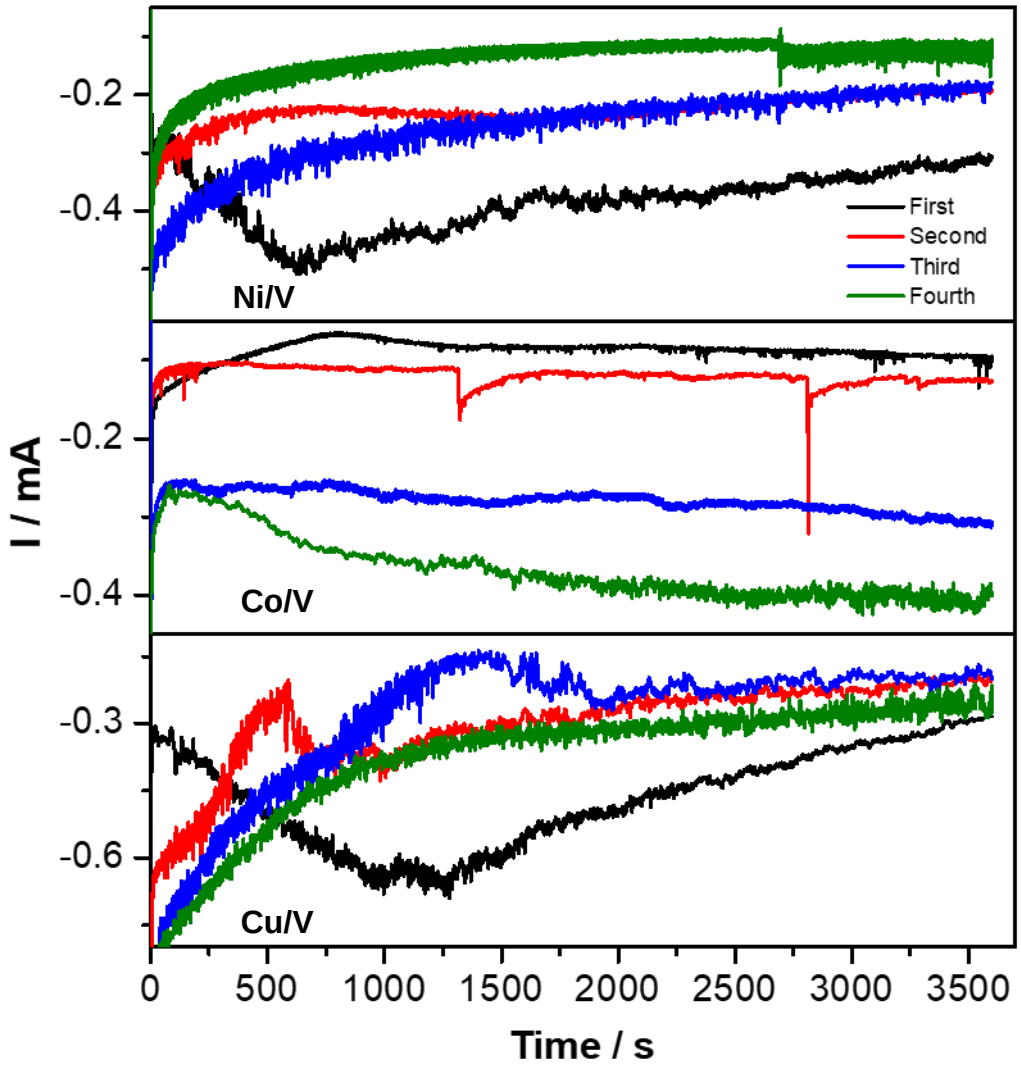

Figure 5.3 Electrodeposition results from the RoDSE method of the Ni, Co and Cu precursors ($NiCl_2$, $CoCl_2{\cdot}6H_2O$ and $CuCl_2$) on carbon V in 20 mL of 0.1 M $KClO_4$.

5.4.2. X-ray powder diffraction

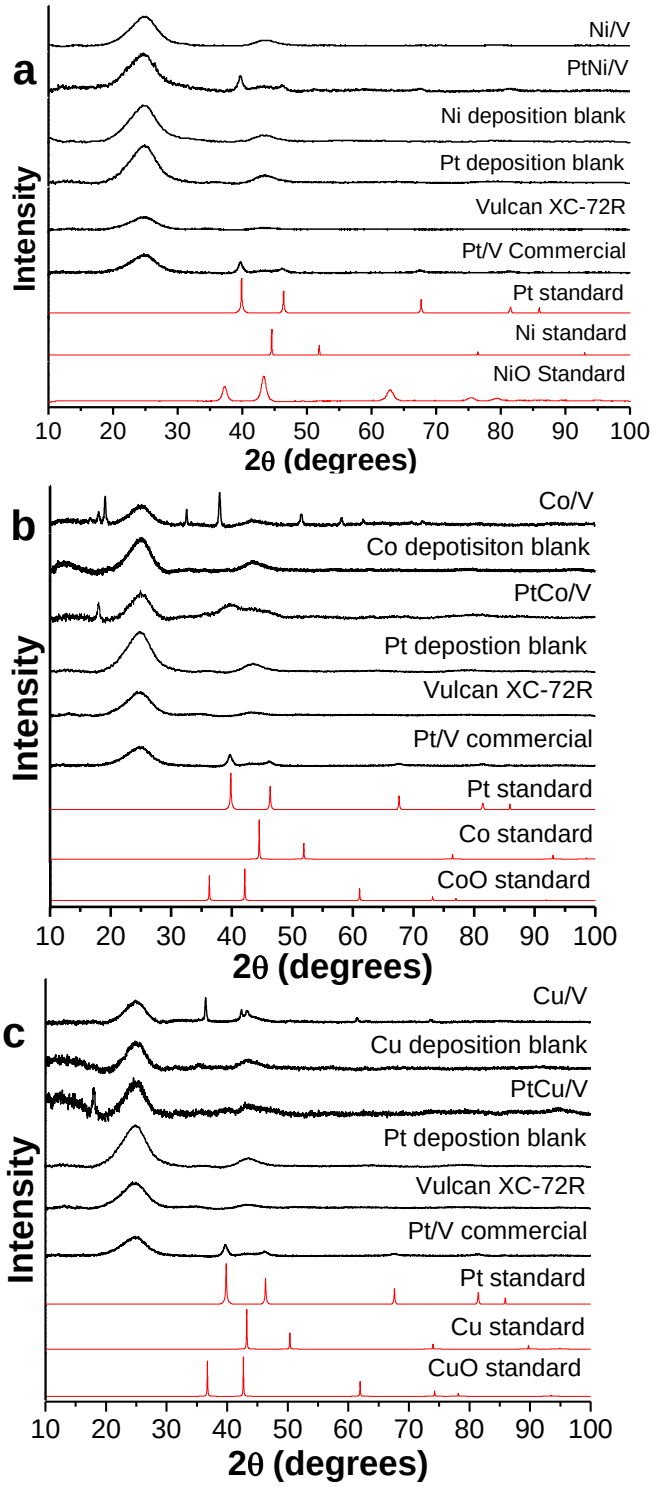

Figure 5.4 PXRD patterns for Ni catalysts (a) Co catalysts (b) and Cu catalysts (c), with their respective commercial standards.

The crystalline structure of the electrocatalysts was confirmed with XRD **Figure 5.4.** First, it was done for the Ni/V, Co/V and Cu/V. For Ni/V **Figure 5.4a** there are no peaks associated with Ni diffraction. Two peaks can be seen at ca. 25° and 43° 2q values associated with the carbon Vulcan XC-72R diffraction. When modifying the Ni/V with Pt the PtNi/V diffractogram shows peaks associated with Pt diffraction at 39.9° (111), 46.5° (200) and 67.9° (220) attributed to fcc Pt.[11] To corroborate further if the obtention of a PtNi/V material is obtained by the presence of electrochemically reduced Ni/V and not just an absorption process of the materials we decided to run a blank experiment of the RoDSE methodology without applying a reduction potential. The material was recovered, and the Ni deposition blank shows a similar diffractogram to the Ni/V sample. However, the Pt deposition blank—using the Ni deposition blank sample for the SGD procedure to obtain a simulated PtNi/V material— does not show any peak related to Pt diffraction. They are letting us conclude that the presence of Pt in the PtNi/V sample is attributed to the Ni/V material obtained by electrodeposition. A similar analysis was executed for the Co/V and Cu/V samples. However, in this case, for both samples, some diffraction peaks can be associated with a mixture of reduced Co and CoO (for the Co/V) and reduced Cu and CuO (for the Cu/V) **Figure 5.4b** and **Figure 5.4c**. Similar peak positioning of Pt diffraction in the PtNi/V can be seen for the PtCo/V and PtCu/V samples.

5.4.3. Transmission electron microscopy and ICP

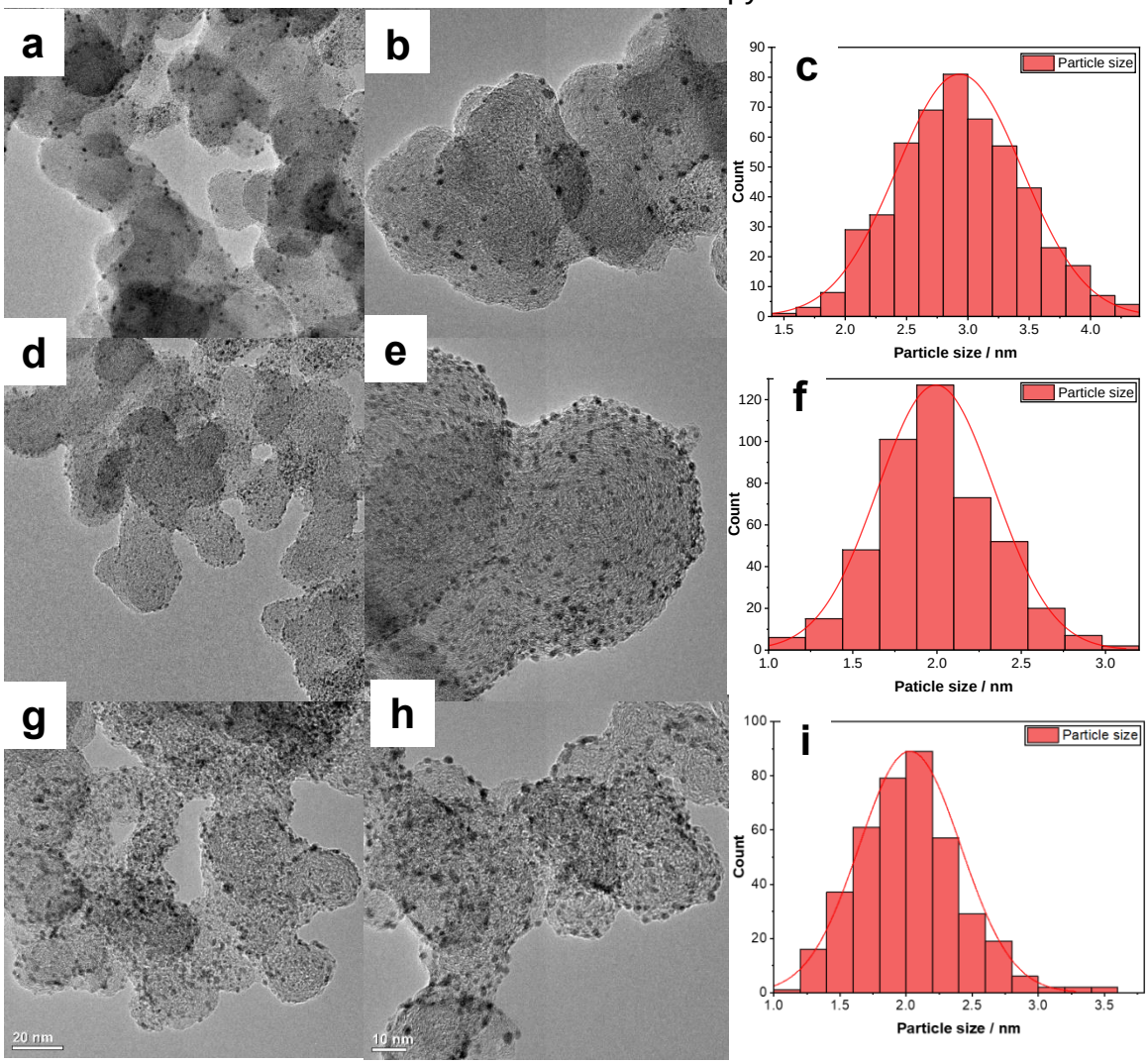

Figure 5.5 TEM images of electrocatalysts and their particle size distribution, PtNi (a), (b), (c), PtCo (d), (e), (f), PtCu (g), (h) and (i).

Table 5.1 Metals concentrations with ICP-OES

Metal	***%w/w concetraction***	***%w/w deviation***	***Atomic Ratio % (Pt:M)***
Ni	0.9	0.2	
Ni in PtNi	0.015	0.003	3%
Pt in PtNi	1.7	0.2	97%
Co	0.7	0.7	
Co in PtCo	0.02	0.01	2%
Pt in PtCo	1.9	0.3	98%
Cu	0.35	0.03	
Cu in PtCu	0.07	0.02	4%
Pt in PtCu	2.97	0.01	96%

To further corroborate the shape and size of the electrocatalysts, we used TEM **Figure 5.5** Very well-dispersed nanoparticles with similar size distribution were found. The resulting particle sizes were 3 nm, 2 nm and 2 nm for the PtNi/V, PtCo/V and PtCu/V, respectively. To obtain the chemical composition of the nanoparticles, we utilized ICP-OES and the results demonstrated that the PtNi/V had a Pt % of 1.7 ± 0.2 the PtCo/V 1.9 ± 0.3 and the PtCu/V 2.97 ± 0.01 **Table 5.1**.

5.4.4. ORR catalytic activity

The purpose of obtaining a low Pt loading using the RoDSE methodology was achieved. However, we need to test the electrochemical activity of these electrocatalysts. The voltammogram shapes of the Pt/M **Figure 5.6a** show the typical electrochemical processes associated with a Pt CV. The difference comes in the current values of the voltammograms comparing the lab-made materials (that had lower currents) and the Pt/V 20% catalyst. This variance is mainly related to their difference in Pt %, proving again that our lab-made materials had low Pt

loadings. The M **Figure 5.6b** also shows characteristic CV patterns for Ni, Co and Cu redox processes.[12,13] It is also confirmed that Ni is present in the Ni/V catalysts obtained by electrodeposition.[12] The electrochemical performance of the PtM/V was tested for ORR **Figure 5.6c** using a mass loading of 100 μg/cm$^2_{geo}$ and PtCo/V had a closer half-wave potential to the commercial catalysts with $E_{1/2}$ = 0.85 V. The M precursor were further tested for OER and Ni/V **Figure 5.6d** showed lower overpotential with 450 mV at 10 mA/cm$^2_{geo}$.

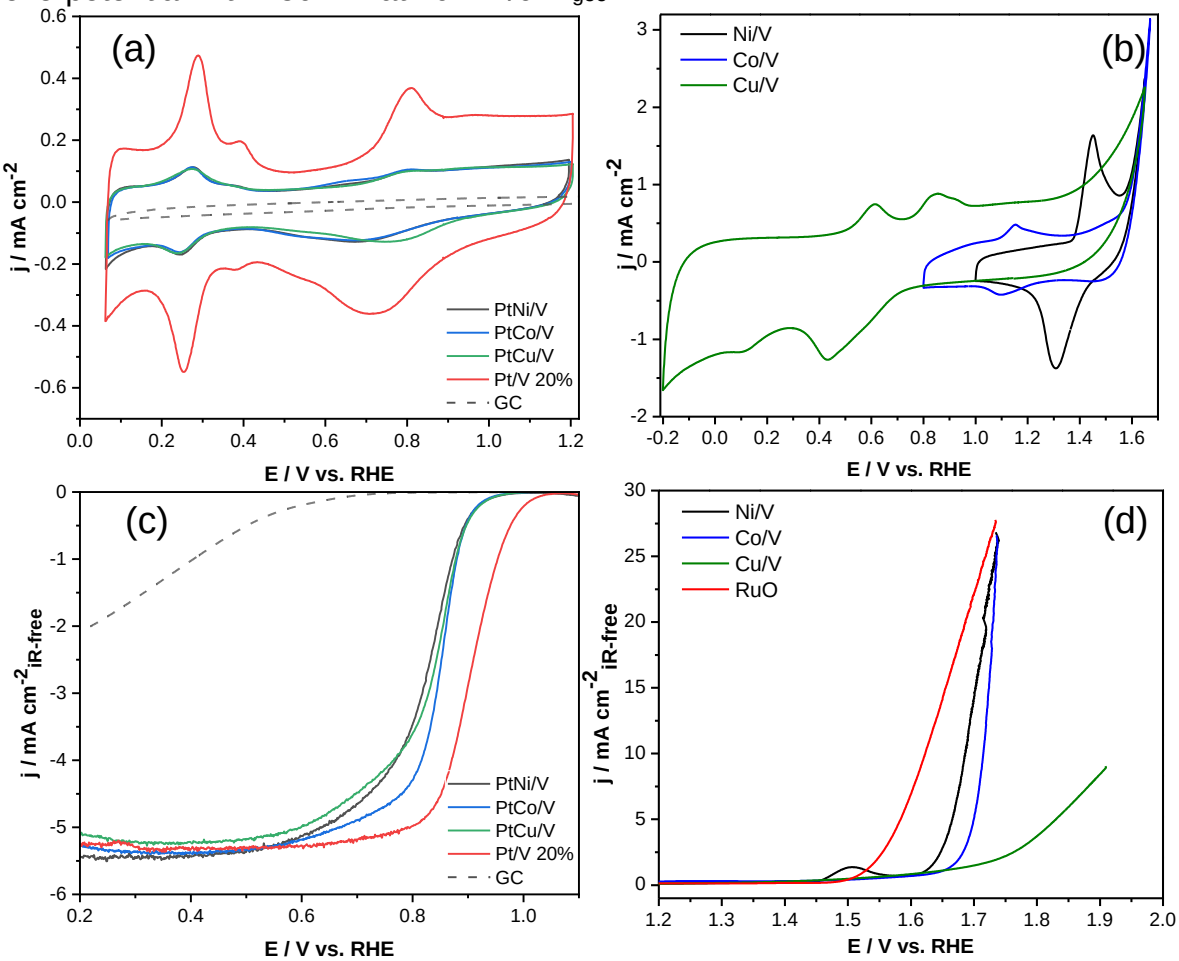

Figure 5.6 (a) Voltammograms of PtNi/V, PtCo/V, PtCu/V and commercial Pt/V at 25 mV/s (b) Voltammograms of Ni/V, Co/V and Cu/V at their respective potential windows at 25 mV/s. (c) ORR polarization curves of PtNi/V, PtCo/V, PtCu/V and commercial Pt/V at 10 mV/s at 1600 rpm. (d) OER polarization curves of Ni/V, Co/V, Cu/V and commercial RuO at 10 mV/s and at 1600 rpm. All the experiments were carried out in 0.1 M KOH.

To determine the number of electrons transferred for each electrocatalyst, we did the KL analysis using **Equations 4.2 and 4.2** as discussed in chapter 4. The KL plots **Figure 5.7** were obtained to get the Levich slope and solve the equations for n. The provided n values were: 4 for PtNi/V, 3.9 for PtCo/V and 4 for PtCu/V. Suggesting that all electrocatalysts reduced molecular oxygen to OH^- through the four-electron pathway. Tafel analysis **Figure 5.8a** was done to understand the kinetics of the ORR after the calculation of the kinetic current densities (j_k)[14] at a fixed rotation rate (1,600 rpm) with **equation 5.1**:

$$j_k = \frac{j}{1-\left(\frac{j}{j_L}\right)} \qquad \textbf{Eq. 5.1}$$

Different tafel slopes could be obtained depending on the electrocatalyst and electrolytes that are chosen.[15] For Pt catalyst under acidic conditions, two tafel slopes are typically obtained with values of 60 mV/decade in the high overpotential region (HOPR) beyond 0.8 V and 120 mV/decade in the low overpotential region (LOPR) below 0.8 V.[16] In alkaline medium specifically 0.1 M KOH slope values for Pt have typical values of 60 mV/decade in the HOPR and 200-490 mV/decade in the LOPR.[17,18] In addition, Pt alloys in an alkaline medium could have values as low as 47 mV/decade in the HOPR to as high as 304 mV/decade in the LOPR.[15] Our electrocatalysts comply with these values obtaining values for PtNi/V, PtCo/V, PtCu/V and Pt/V 20% in the HOPR of 68 mV/decade, 54 mV/decade, 65 mV/decade, 79 mV/decade and in the LOPR of 197 mV/decade, 253 mV/decade, 238 mV/decade and 229 mV/decade, respectively.

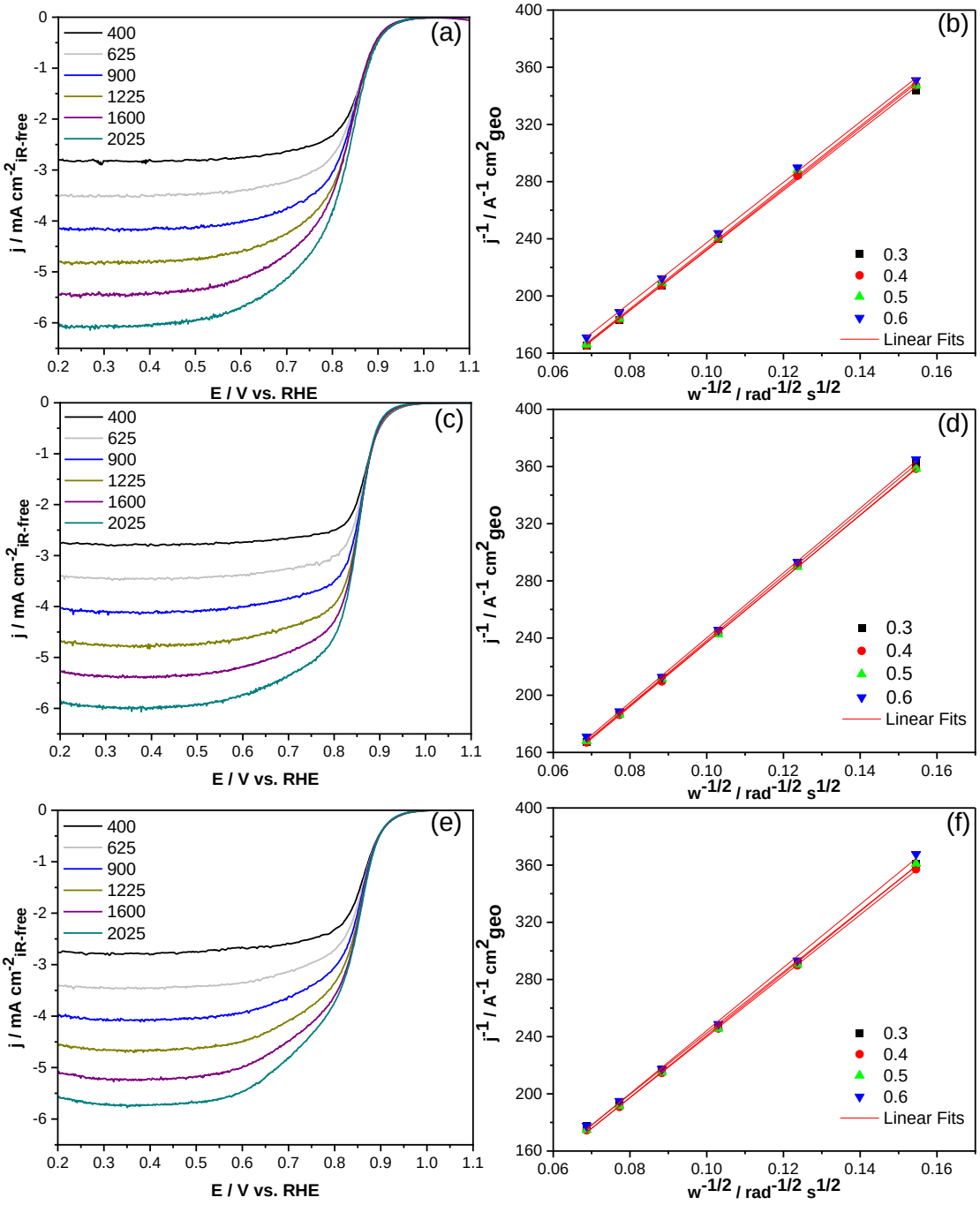

Figure 5.7 ORR polarization curves at 10 mV/s in 0.1 M KOH at various rpm for (a) PtNi/V (b) PtCo/V (c) PtCu/V and Koutecký–Levich plots of (d) PtNi/V (e) PtCo/V and (f) PtCu/V.

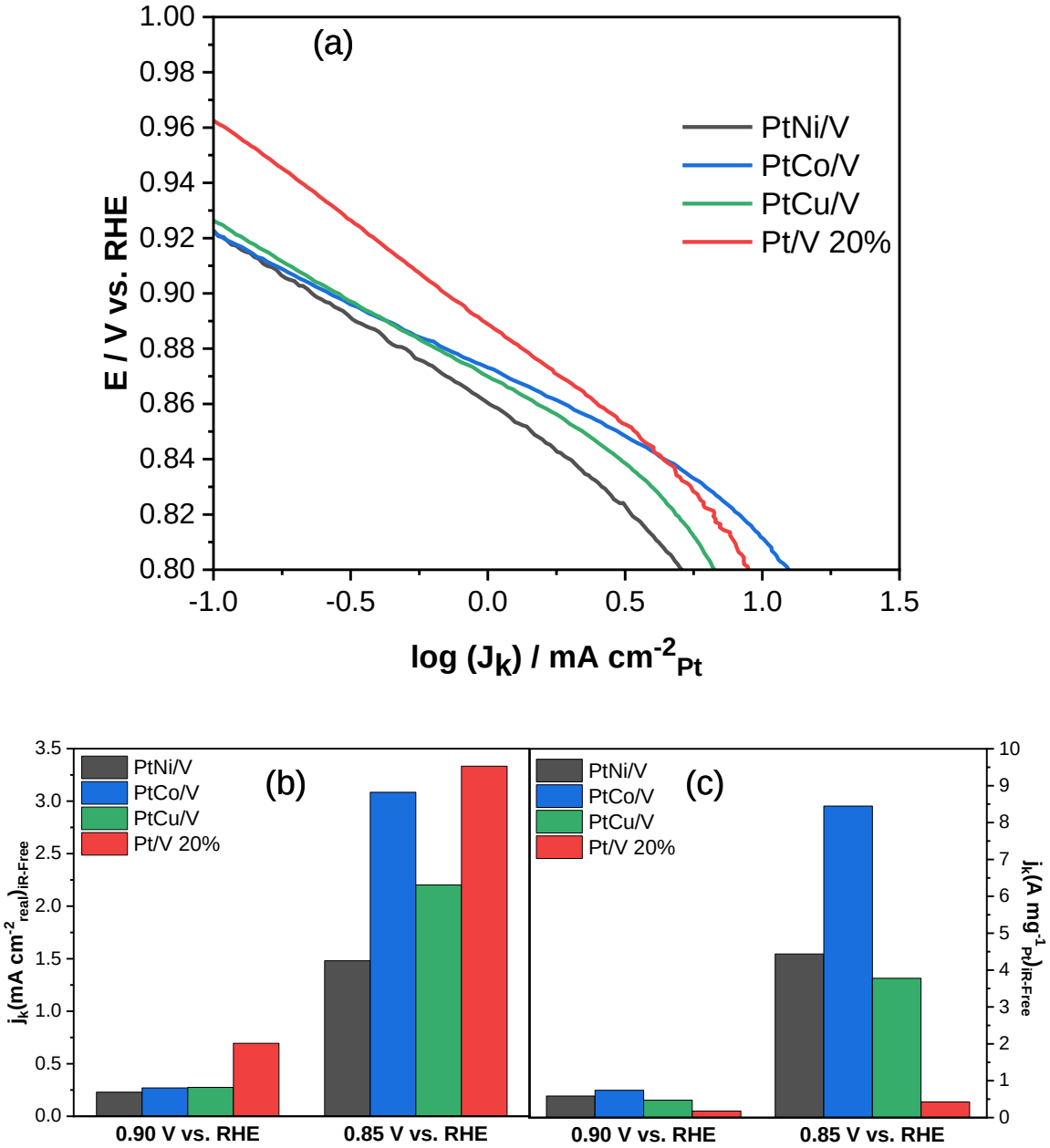

Figure 5.8 (a) Tafel plots (b) specific activities and (c) mass activities for the catalysts derived from kinetic current of the Tafel plots.

The tafel analysis was further used to determine the specific and mass activities. The specific activities (mA cm^{-2}_{real}) **Figure 5.8b** of our catalysts were close to each other with values of 0.229, 0.271 and 0.275 at 0.90V and 1.480, 3.083 and 2.202 values at 0.85 V for PtNi/V, PtCo/V and PtCu/V, respectively. However, the Pt/V commercial catalysts had 0.694 at 0.90 V and 3.332 at 0.85 V. This were expected results considering that the commercial catalyst had a lower overpotential in the ORR polarization curves. The determinant difference came when we analyzed the mass activities (A mg^{-1}_{Pt}) **Figure 5.8c**,—an important parameter for catalysts efficiency in terms of cost— we see that all the lab-made electrocatalyst surpassed the Pt/V 20% commercial catalyst with PtCo/V having the highest values with 0.741 at 0.90 V and 8.446 at 0.85 V.

5.4.5. Durability experiments

Considering that PtCo/V and PtNi/V gave better mass activities values, we examined their ORR performance with accelerated durability experiments to tests in 0.1 M KOH **Figure 5.9**. Both catalysts exhibited good performance through 10k cycles. PtNi/V gave the best overpotential resulting in 5 mV compared to PtCo/V 28 mV and Pt/V commercial 27 mV. After 30 k cycles, the catalysts remained active and comparable overpotential results to Pt/V were obtained for PtNi/V and PtCo/V with 40 and 50 mV, respectively. Although our most active catalyst—considering PGM mass—did not retain higher $E_{1/2}$ activity after 30 k cycles, their overpotential performance is like the Pt/V commercial catalyst, suggesting that they are suited for further AEMFCs studies.

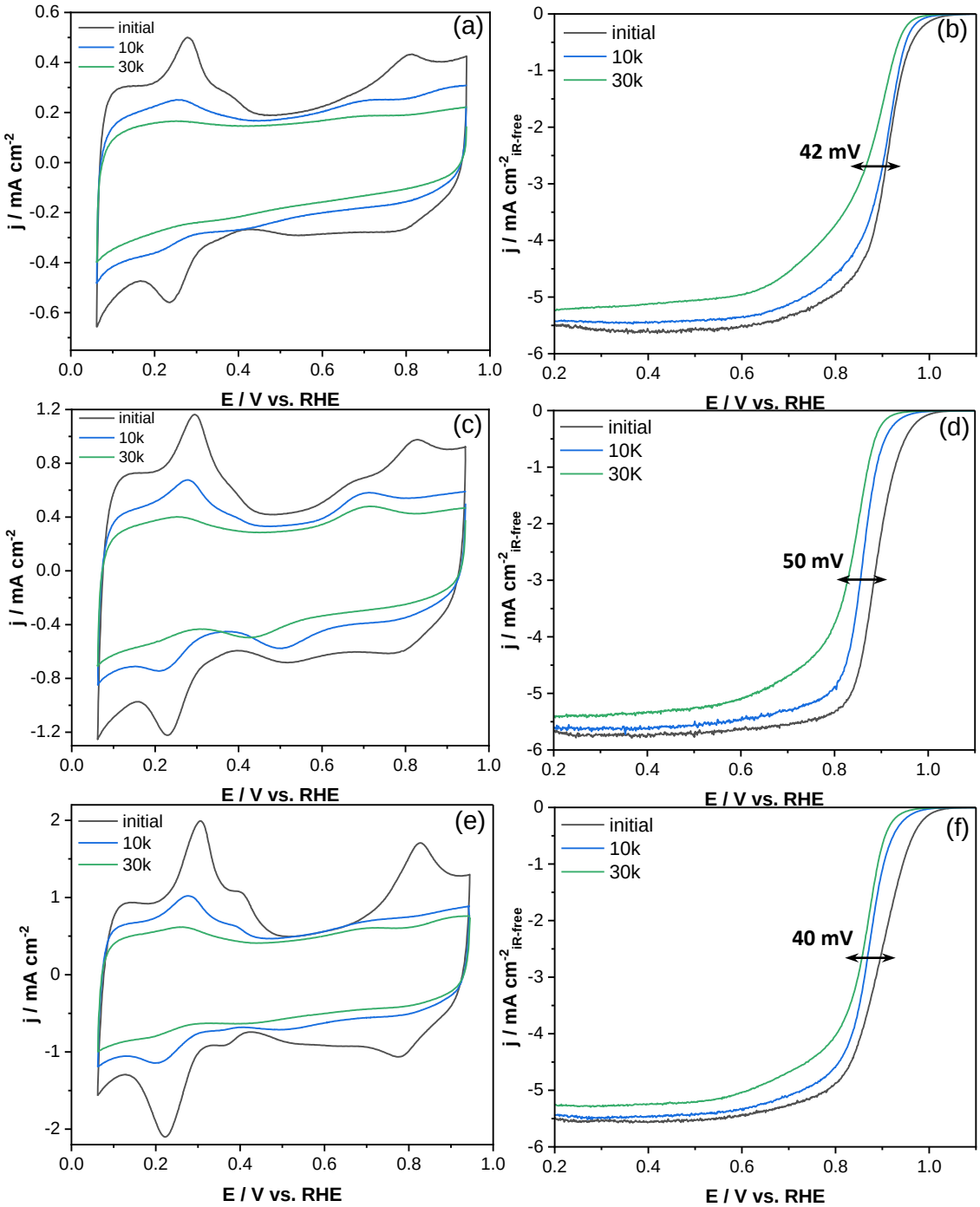

Figure 5.9 Cyclic voltammograms at 25 mV/s in 0.1M KOH for (a) PtNi/V (b) PtCo/V (c) Pt/V 20% commercial and ORR polarization curves at 10 mV/s in 0.1 M KOH at 1,600 rpm (d) PtNi/V (e) PtCo/V and (f) Pt/V 20% commercial. All recorded with initial measurements, after 10k cycles and after 30k cycles.

5.4.6. Ex situ X-ray absorption spectroscopy

All the samples were submitted to ex situ XAS characterizations, see **Figure 5.10**. Depending on the selected energy, a specific electronic transition will be obtained, serving as a probe to identify our elemental species. We focused on the XANES region to obtain information regarding the samples' electronic structure and the local chemical environment. The obtained spectra were compared with the respective standards. However, it is essential to highlight that first-row transition metals using the K-edge can exhibit what is called the forbidden transition (1s → 3d), which is associated with a pre-edge peak. The Ni samples, Ni/V and PtNi/V, shown in **Figure 5.10a,** exhibit higher intensity than the NiO and Ni foil standards, suggesting that the samples are both oxidized. But the intensity of Ni/V is higher than PtNi/V. This could indicate that Pt is donating electrons to Ni or that since Ni is expected to be in the core of the PtNi/V sample Ni, it is not being oxidized by the air, resulting in a more reduced Ni specie. The Co sample shows a similar behavior as seen in **Figure 5.10b**. Both, Co/V and PtCo/V have higher intensity than the standards. A lower intensity is observed in the PtCo/V than the Co/V, suggesting the same statement for the Ni sample. The Cu sample is different, see **Figure 5.10c** shows that Cu in the Cu/V has lower intensity, meaning that it is less oxidized compared to the Cu in the PtCu/V sample. This means that Cu is donating electrons to Pt. These Pt samples were then compared using the Pt L_3-edge, see **Figure 5.10d**. The lab-made Pt samples show a similar spectrum with their intensity close by to the PtO_2 and Pt/V standards. This tells us that the Pt samples have more presence of oxide species.

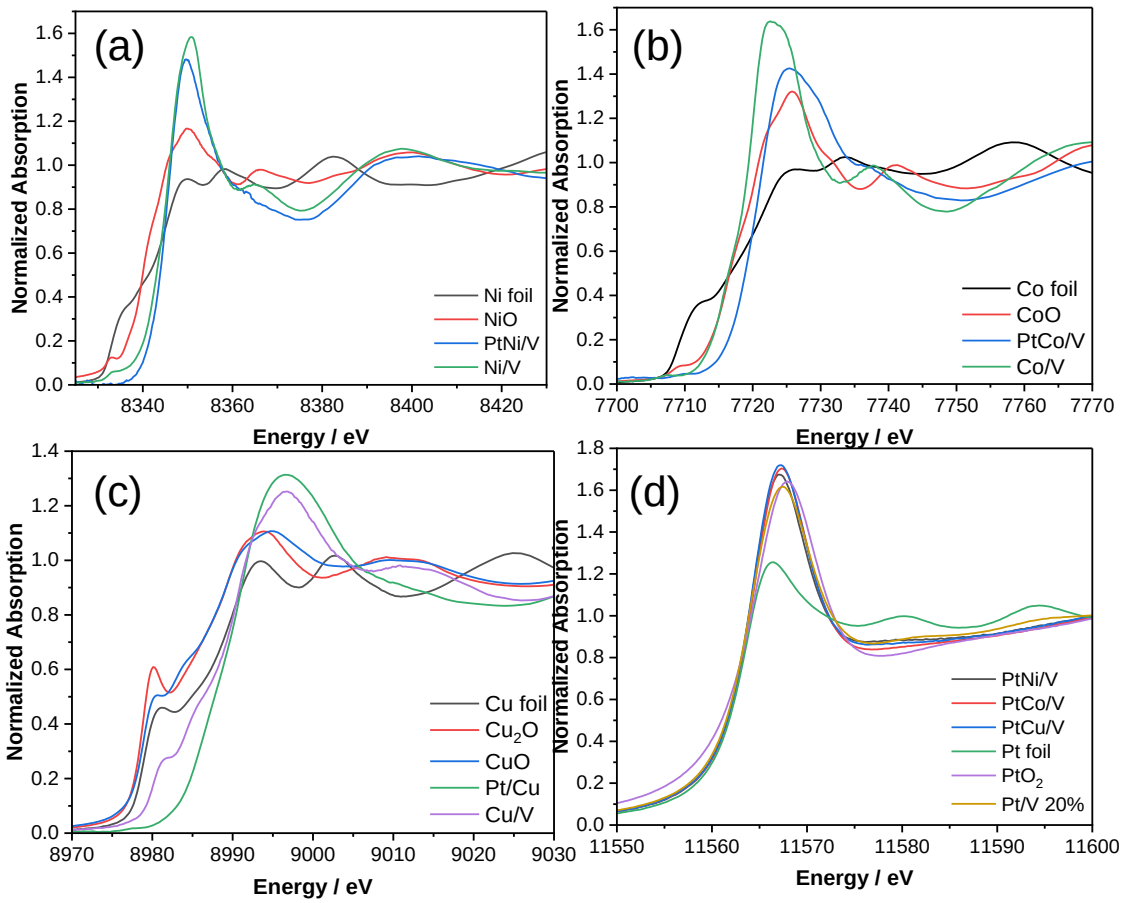

Figure 5.10 Ex-situ XANES spectrums for (a) Ni samples using Ni K-edge (b) Co samples using Co K-edge (c) Cu samples using Cu K-edge and (d) Pt samples using Pt L_3-edge, all with their respective standards.

5.4.7. *In situ* X-ray absorption spectroscopy

Recognizing that PtCo/V gave us the best ORR performance, we decided to study the sample with *in situ* electrochemical XAS experiments using the Pt L_3-edge **Figure 5.11**. These studies were done while air was permitted inside the electrochemical cell, simulating an ORR experiment. There is a clear relationship between the intensity of the whiteline peak and the applied electrochemical potential in the XANES region of the PtCo/V and the Pt/V 20% **Figure 5.11a and**

b. As the applied potential is more negative, a decrease in the whiteline intensity is observed, indicating that the Pt species are reduced in both samples.

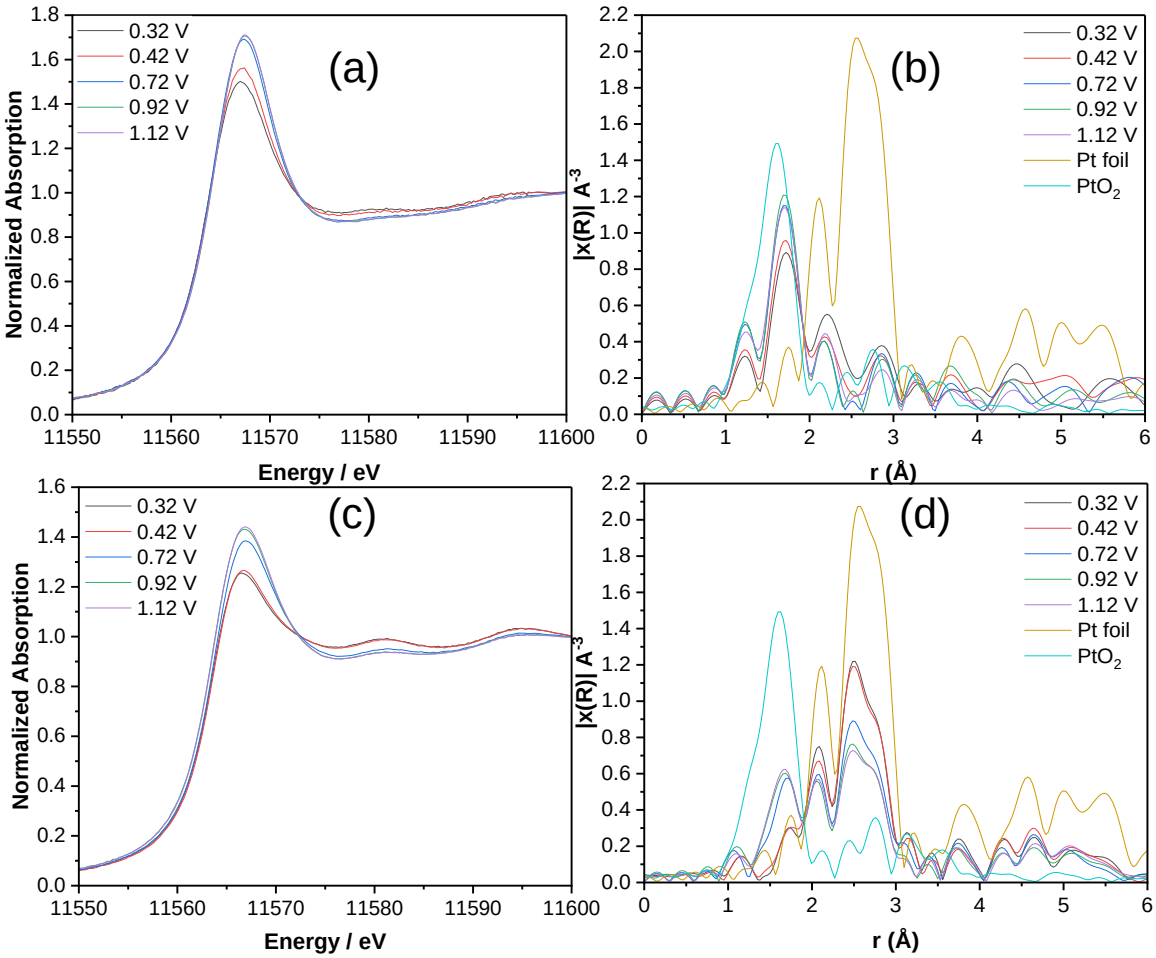

Figure 5.11 *In situ* electrochemical experiments using the Pt L_3-edge for (a) the XANES region and (b) EXAFS region of the PtCo/V samples and for the (c) the XANES region and (d) EXAFS region of the Pt/V 20% commercial sample.

These experiments can further relate to classic ORR polarization curves obtained by RDE. First, the intensities of both samples at potentials 1.12 V and 0.92 V are very similar. These potentials are associated with the onset potential region of the ORR. Then, at 0.72 V we notice that the intensity is decreased more,

suggesting that the ORR is happening. However, a more significant jump to lower intensities is seen in both samples between potentials 0.72 V and 0.42 V. This makes sense because this is a potential active region where the ORR occurs. Then, we see that the whiteline intensity at 0.32 V is very similar to 0.42 V, indicating that this may be the limiting current region. This information clarifies that our catalyst undergoes ORR in the Pt species and behaves similarly to a commercial catalyst.

The EXAFS region was also analyzed as shown in **Figures 5.11b and d**. Comparing the samples with Pt foil and PtO_2 standards, we get that the PtCo/V sample at each potential shows a significant peak in the region of the Pt—O distance at ca. 1.6 Å, see **Figure 5.11b**. When we look at the intensity of the Pt—Pt bond in the region of ca. 2.6 Å we notice that theres is no clear difference agains the backround noise for most of the potentials. This suggests that the sample is a Pt oxide as it has a similar spectrum to the PtO_2. Interestenly, at potentials 0.42 and 0.32 V the Pt—Pt bond peak has higher intensity while Pt—O reduces its intensity, suggesting that the Pt is changing from being as a PtO_2 to a Pt^0. It could also be that the particles are way to small to exhibit the bouncing near neighbor phenomenon of metal absorber. On the other hand, the Pt/V 20% at each applied potential shows a similar spectrum to the Pt foil standard, suggesting that the sample is metallic. There's a clear peak at the Pt—Pt bond region and a lower intensity of the peak located at the Pt—O bond region.

5.5. Conclusions

The RoDSE methodology was successfully explored for the first time to synthesize Ni, Co and Cu nanoparticles supported on Vulcan. These nanoparticles were very dispersed and had homogeneous diameter sizes of ca. 2-3 nm. They were then tested for their OER activity in which Ni/V had a lower overpotential with 450 mV at 10 mA/cm^2_{geo} among the lab-made catalysts. Then, after SGD, PtM/V nanoparticles were obtained with low Pt % content. These PtM/V samples were submitted to multiple characterizations, and their electrochemical performance was exanimated for the ORR. All the samples followed a 4-electron pathway for the ORR. Compared with all samples, the PtCo/V had better mass activity ($A\ mg^{-1}_{Pt}$) values with 0.741 at 0.90 V and 8.446 at 0.85 V. Then, durability experiments showed that PtNi/V and PtCo/V had similar performance to a commercial Pt/V 20% catalysts after 30 K CV cycles of accelerated durability tests, suggesting that our catalysts can be further tested in AEMFCs.

The samples' electronic structure was studied with XAS techniques confirming the presence of all the elements in our samples. The ex-situ XAS studies suggested that all the samples were oxidized. The PtCo/V sample was further tested for *in situ* electrochemical XAS experiments. After monitoring the XANES region, we concluded that this oxidized sample followed a typical ORR RDE experiment having its whiteline intensity decreased—this is associated with a less oxidized electronic structure—as more negative potentials were applied. The EXAFS region also confirmed the oxide form of Pt (PtO_2) in the PtCo/V samples. The low Pt amount of the samples did not limit its ORR performance suggesting

that low percentages of PGM should be incorporated into PGM catalysts to optimize mass activity performances directly related to catalysts cost and efficiency. Since these samples are close to 2 nm in diameter (like quantum dots and close to single-atom catalysts), further characterization with better electron microscopy resolution techniques at the beamline is suggested to understand the samples' electronic structure better.

5.6. References

(1) Santiago, D.; Rodríguez-Calero, G. G.; Palkar, A.; Barraza-Jimenez, D.; Galvan, D. H.; Casillas, G.; Mayoral, A.; Jose-Yacamán, M.; Echegoyen, L.; Cabrera, C. R. Platinum Electrodeposition on Unsupported Carbon Nano-Onions. *Langmuir* **2012**, *28*, 17202–17210.

(2) Vélez, C. A.; Corchado-García, J.; Rojas-Pérez, A.; Serrano-Alejandro, E. J.; Santos-Homs, C.; Soto-Pérez, J. J.; Cabrera, C. R. Manufacture of Pd/Carbon Vulcan XC-72R Nanoflakes Catalysts for Ethanol Oxidation Reaction in Alkaline Media by RoDSE Method. *J. Electrochem. Soc.* **2017**, *164*, D1015–D1021.

(3) Vélez, C. A.; Soto-Pérez, J. J.; Corchado-García, J.; Larios, E.; Fulvio, P. F.; Echegoyen, L.; Cabrera, C. R. Glucose Oxidation Reaction at Palladium-Carbon Nano-Onions in Alkaline Media. *J. Solid State Electrochem.* **2021**, *25*, 207–217.

(4) Betancourt, L. E.; Ortiz-Rodríguez, Á. M.; Corchado-García, J.; Cabrera, C. R. RoDSE Synthesized Fine Tailored Au Nanoparticles from Au(X)4- (X = Cl-, Br-, and OH-) on Unsupported Vulcan XC-72R for Ethanol Oxidation Reaction in Alkaline Media. *ACS Appl. Energy Mater.* **2019**, *2*, 287–297.

(5) Vega-Cartagena, M.; Flores-Vélez, E. M.; Colón-Quintana, G. S.; Blasini Pérez, D. A.; De Jesús, M. A.; Cabrera, C. R. Silver-Palladium Electrodeposition on Unsupported Vulcan XC-72R for Oxygen Reduction Reaction in Alkaline Media. *ACS Appl. Energy Mater.* **2019**, *2*, 4664–4673.

(6) Peña-Duarte, A.; Vijapur, S. H.; Hall, T. D.; Hayes, K. L.; Larios-Rodríguez, E.; Pilar-Albaladejo, J. Del; Santiago, M. B.; Snyder, S.; Taylor, J.; Cabrera, C. R. Iron Quantum Dots Electro-Assembling on Vulcan XC-72R: Hydrogen Peroxide Generation for Space Applications. *ACS Appl. Mater. Interfaces* **2021**, *13*, 29585–29601.

(7) Ravel, B.; Newville, M. ATHENA, ARTEMIS, HEPHAESTUS: Data Analysis for X-Ray Absorption Spectroscopy Using IFEFFIT. *J. Synchrotron Radiat.*

2005, *12*, 537–541.

(8) Alfantazi, A. M.; Ahmed, T. M.; Tromans, D. Corrosion Behavior of Copper Alloys in Chloride Media. *Mater. Des.* **2009**, *30*, 2425–2430.

(9) Lantelme, F.; Seghiouer, A.; Derja, A. Model of Nickel Electrodeposition from Acidic Medium. *J. Appl. Electrochem.* **1998**, *28*, 907–913.

(10) Arkam, C.; Bouet, V.; Gabrielli, C.; Maurin, G.; Perrot, H. ELECTROCHEMICAL SOCIETY LETTERS Quartz Crystal Electrogravimetry with Controlled Hydrodynamics Applications to the Study of Nickel Electrodeposition. *J. Electrochem. Soc* **1994**, *141*, L103–L105.

(11) Jia, Q.; Zhao, Z.; Cao, L.; Li, J.; Ghoshal, S.; Davies, V.; Stavitski, E.; Attenkofer, K.; Liu, Z.; Li, M.; Duan, X.; Mukerjee, S.; Mueller, T.; Huang, Y. Roles of Mo Surface Dopants in Enhancing the ORR Performance of Octahedral PtNi Nanoparticles. *Nano Lett.* **2018**, *18*, 798–804.

(12) Oshchepkov, A. G.; Braesch, G.; Bonnefont, A.; Savinova, E. R.; Chatenet, M. Recent Advances in the Understanding of Nickel-Based Catalysts for the Oxidation of Hydrogen-Containing Fuels in Alkaline Media. *ACS Catal.* **2020**, *10*, 7043–7068.

(13) Giri, S. D.; Sarkar, A. Electrochemical Study of Bulk and Monolayer Copper in Alkaline Solution. *J. Electrochem. Soc.* **2016**, *163*, H252–H259.

(14) Briega-Martos, V.; Herrero, E.; Feliu, J. M. Effect of PH and Water Structure on the Oxygen Reduction Reaction on Platinum Electrodes. *Electrochim. Acta* **2017**, *241*, 497–509.

(15) Shinagawa, T.; Garcia-Esparza, A. T.; Takanabe, K. Insight on Tafel Slopes from a Microkinetic Analysis of Aqueous Electrocatalysis for Energy Conversion. *Sci. Rep.* **2015**, *5*, 13801.

(16) Murthi, V. S.; Urian, R. C.; Mukerjee, S. Oxygen Reduction Kinetics in Low and Medium Temperature Acid Environment: Correlation of Water Activation and Surface Properties in Supported Pt and Pt Alloy Electrocatalysts. *J. Phys. Chem. B* **2004**, *108*, 11011–11023.

(17) Zinola, C. F.; Castro Luna, A. M.; Triaca, W. E.; Arvia, A. J. Kinetics and Mechanism of the Electrochemical Reduction of Molecular Oxygen on Platinum in KOH: Influence of Preferred Crystallographic Orientation. *J. Appl. Electrochem.* **1994**, *24*, 531–541.

(18) Tammeveski, K.; Arulepp, M.; Tenno, T.; Ferrater, C.; Claret, J. Oxygen Electroreduction on Titanium-Supported Thin Pt Films in Alkaline Solution. *Electrochim. Acta* **1997**, *42*, 2961–2967.

Chapter 6. **Metallic Monolayers on Copper supports for Energy Conversion Reaction**

6.1. Abstract

The Pb e-less deposition method was used on Au monocrystals, NbN/V, and Cu catalysts. The Au monocrystal experiments proved the Pb e-less deposition concept. The use of STEM provided information on the Pt positioning on the NbN/V, suggesting a correlating behavior of more Pt as more Pb e-less cycles were done. Pd catalysts were then obtained on Cu (100) NPs and PdCu (100) and the current associated with Pb ML UPD and e-less deposition probed a ML deposition were measured. The PdCu(100) electrocatalyst was further used in an alkaline medium for ORR studies. The oxygen polarization curves demonstrate that the PdCu(100) outperforms commercial PdCu/V and Pd/V catalysts obtaining a half-wave potential ($E_{1/2}$) of 0.88 V vs. RHE and that it also drives the ORR by the 4-electron pathway.

6.2. Introduction

This research project utilizes a novel Pb electroless deposition method[1], which leads to Pb being deposited on a support (in this case, a Cu catalyst). Then, after spontaneous galvanic displacement (SGD), the Pb is replaced by M (M= Pt, Pd…) and MCu (M= Pt and Pd) ML electrocatalysts are obtained. We can design active materials by controlling the low index planes of the ML electrocatalysts. Hoshi *et* al. proved that a Pd (100) has a higher activity for ORR compared to Pd (100) and Pd (110).[2] We hypothesize that if we deposit a Pd ML on a Cu (100)

support, we will obtain a PdCu(100) catalyst that will have higher ORR activity than a polycrystalline Pd commercial catalyst.

6.3. Research design and methods

6.3.1. Catalyst synthesis

In a typical synthesis, a $NbCl_5$ precursor and Vulcan XC-72R were dissolved on chloroform—previously purified by molecular sieves A4— for 1 h in a dry box filled with UPD Ar. The solution samples were stirred for 1 h. Then, the solution was transferred to a Schlenk line where the dissolved chlorides were exposed to NH_3 gas for 8 h.[3] The annealing step was followed using a tube furnace. The solvent was exposed to 700 °C for 2 h and 700 °C for 10 h under NH_3 flow. The sample was reconstituted in powder form and the NbN/V was obtained. The Cu (100) nanoparticles were obtained in collaboration with CFN at BNL.

The catalysts were synthesized based on the Pb electroless deposition on selected supports, followed by a spontaneous galvanic displacement. Here, the desired material, in most cases metal, is deposited on a layer of another material at an OCP. This process is surface selective, surface controlled and self-terminating. The synthesis was based on the electrochemical potentials of Pb (PbO) and V (VCl) redox couples. The respective Pb and V solutions concentrations were calculated considering their stoichiometry. We used a two-electrode electrochemical setup based on a WE, which could be a GC electrode modified with the selected catalyst as described in chapter 5, section 5.3.3. or a metal monocrystal and Ag/AgCl (sat. KCl) as the RE. The electrodes were immersed in an electrochemical cell, sealed, and saturated with Ar, with 3 mM PbO

solution in 0.1 M $HClO_4$ see **Figure 6.1** to follow a schematic procedure. Then, the OCP monitoring technique was chosen on the potentiostat software (EC-Lab). The system was left at equilibrium, and after ca. 1 min, the calculated aliquot of 50 mM VCl_2 in 0.1 M $HClO_4$ was slowly added to the electrochemical cell. The synthesis was finished when the OCP was close to the redox potential of Pb vs. Ag/AgCl.

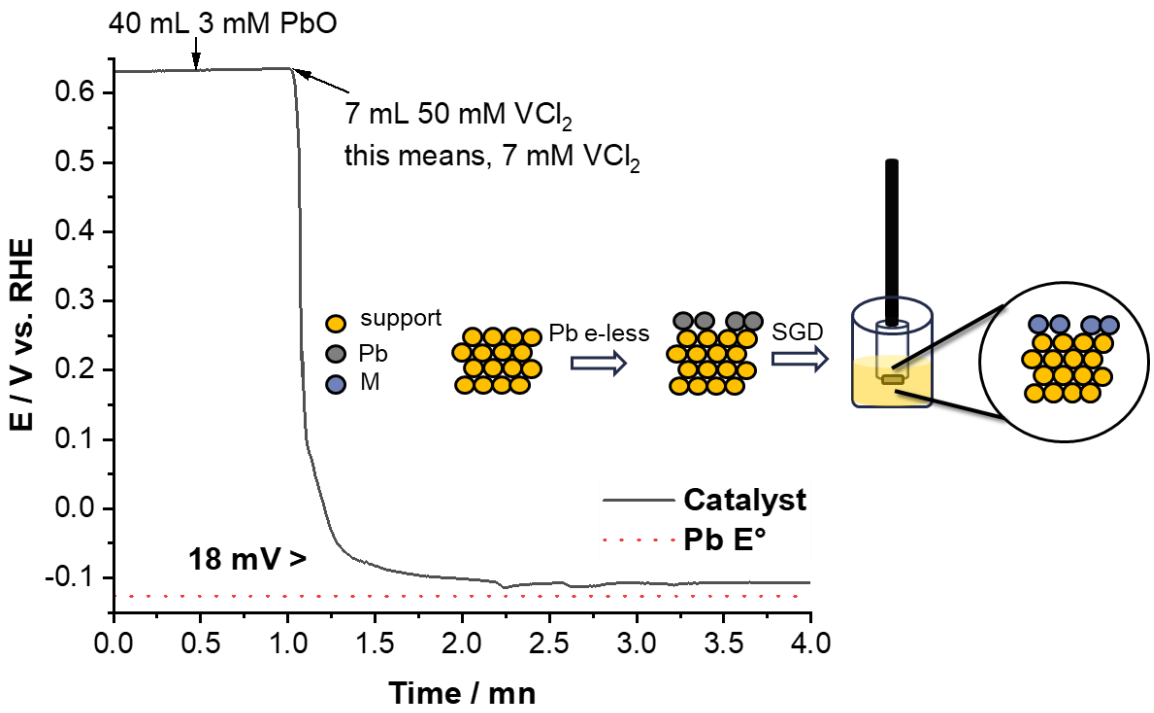

Figure 6.1 Scheme explanation of open circuit transient of Au (III) catalysts while the Pb e-less method using 3 mM PbO and 7mM VCl_2 and spontaneous galvanic displacements process after the Pb-eless deposition.

For the SGD procedure, the WE, now modified with Pb, was immersed for 1 min on a 10 mM H_2PtCl_4 or 10 mM K_2PdCl_4. Then the WE modified with the selected support and metal surface catalyst was subjected to electrochemical characterization and measurements.

6.3.2. Scanning transmission electron microscopy

STEM was done to examine the atoms' arrangement, size, and surface elemental composition of the catalyst and prove if we could obtain a monolayer of the M on top of the support. The samples were analyzed in STEM annular dark field (ADF) and bright-field (BF) modes and EDS was used to get the elemental compositions using the JEM-ARM200F with an accelerating voltage of 80kV from the facilities of N.E. Chemcat. To obtain the catalysts for STEM analyses, we sonicated the WE modified with the chosen catalysts using Pb electroless deposition method in EtOH and H_2O. Then, before preparing the STEM sample, an ultrasonic wave was used to disperse the dispersion. The dispersion was scooped up on a microgrid Cu mesh grid and dried to obtain the final sample.

6.3.3. Electrochemical measurements

A similar electrochemical setup, GC electrode cleaning/activation and ink preparation was done as described in section 5.3.3. CV was used to characterize the electrocatalysts depending on their respective potential windows. The electroless deposition of Pb was held on different supports. Different Au disks (Au (100), (110) and (111)) were the first supports to confirm the Pb e-less deposition method. Before the synthesis, the Au disks were cleaned by mechanical polishing using alumina with granular sizes of 1.0, 0,5 and 0.03 µm and pure water, in an eighth-shape pattern. The electrodes were rinsed with pure water and thoroughly dried. Each Au electrode was then annealed using a butane torch until achieving a bright orange color. After waiting for 2 min at ambient temperature, a drop of pure water was added to the electrode to prevent further oxidation.

The electrode was then submitted to electrochemical cleaning by oxidizing the surface at 2 V vs Ag/AgCl sat. KCl for 15 seconds in 0.1 M $HClO_4$ until seeing a brownish oxide layer on the Au surface. This AuOx was immersed in 0.1 M HCl, to dissolve the generated oxides and the process was repeated until getting a cleaned surface structure. The Au electrode was rinsed with pure water and then sonicated. To finish, the Au surfaces were cleaned using the hanging meniscus method **Figure 6.2** by cycling in 0.1 M $HClO_4$ within the potential limits of HER and OER to restore the surface structure.

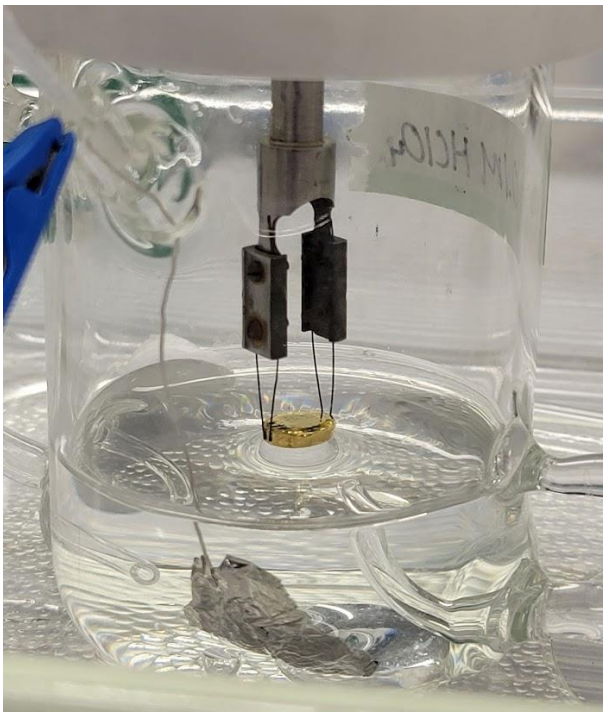

Figure 6.2 Hanging meniscus setup for the monocrystal disk experiments.

For the Cu(*hkl*) experiments, the disk was cleaned using mechanical polishing as described for the Au(111) disk. The Cu disk was then dried very well and was immersed in the concentrated acetic acid solution for 1 min. The electrode was then rinsed with pure water and a drop of water was led in the disk surface to

prevent further oxidation. The electrochemical surface area of the electrode was calculated as explained in section 3.3.4.

6.3.4. Rotating disk electrode experiments

The RDE experiments followed a similar procedure as Chapter 5, section 5.3.4, using 0.1 M KOH and a three-electrode RDE electrochemical setup.

6.4. Results and discussion

6.4.1. Catalyst Pb depositions

6.4.1.1.Au monocrystals and Au/V 20% Pb deposition

The first experiments that were held were using an Au(111) monocrystal since it has already been proven that the Pb e-less process occurs in the Au surface by a similar procedure.[1] The Au(111) electrode shows similar behavior to what we would expect for the deposition of Pb on its surface. When the electrode is only exposed to the dehydrated PbO solution, the OCP transient has a stable potential **Figure 6.3**.

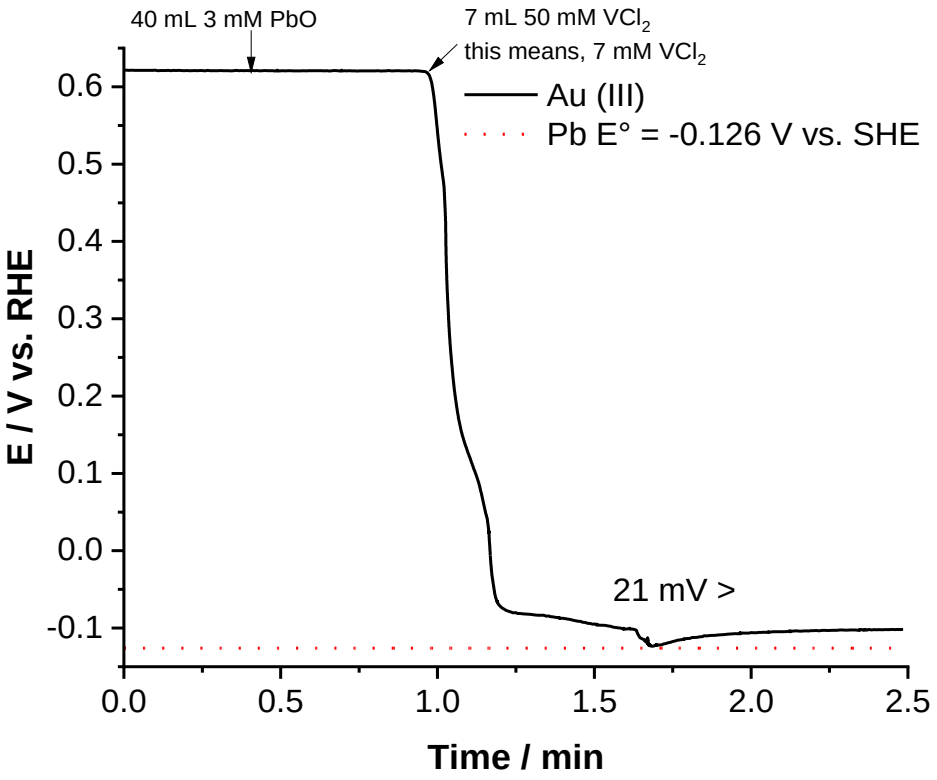

Figure 6.3 OCP transient of the Pb eless deposition on Au (111) monocrystal.

As soon as the VCl_2 solution is added to the PbO solution, a sharp decrease in potential is observed, attributed to the chemical reaction between Pb (**equation 6.1**) and V (**equation 6.2**). This overall reaction considers the parasitic electron reaction of hydrogen (**equation 6.3**) since Pb deposition occurs at a more cathodic potential than the H redox potential. The final reaction (**equation 6.4**) has Pb in its metallic state. This Pb^0 is supposed to be obtained on the surface of the WE, in this case, Au(111). The OCP transient confirms this by having the redox system stabilizing close to the redox potential of Pb.

$$Pb^{2+} + 2e^{-} \leftrightarrow Pb^{0} \; E^{0} = -0.126 \; vs. SHE \qquad \textbf{Eq. 6.1}$$

$$V^{2+} \leftrightarrow V^{3+} + 1e^{-} \; E^{0} = -0.260 \; V \; vs. SHE \qquad \textbf{Eq. 6.2}$$

$$2H^{+} + 2e^{-} \leftrightarrow H_{2(g)} \; E^{0} = 0 \; V \; vs. SHE \qquad \textbf{Eq. 6.3}$$

$$2V^{2+} + 2H^{+} + Pb^{2+} \leftrightarrow 2V^{3+} + Pb^{0} + H_{2(g)} \qquad \textbf{Eq. 6.4}$$

To further confirm that we had the Pb deposited on the surface of Au (111) we proceeded to compare CVs doing underpotential deposition (UPD) monolayers (ML) of Pb on Au (111) with CVs of the anodic stripping of Pb on the Au (111) surface after the Pb e-less process **Figure 6.4a**. The peaks associated with Pb deposition are seen towards the anodic region at potentials between 0 and 0.2 V vs. RHE. A shift to negative potentials of the Pb peaks is obtained in the Pb stripping CV compared to the Pb UPD ML CV. This cathodic shift of the CV may happen because when doing the anodic stripping of Pb the are no Pb^{2+} in the electrolyte.[1,4]

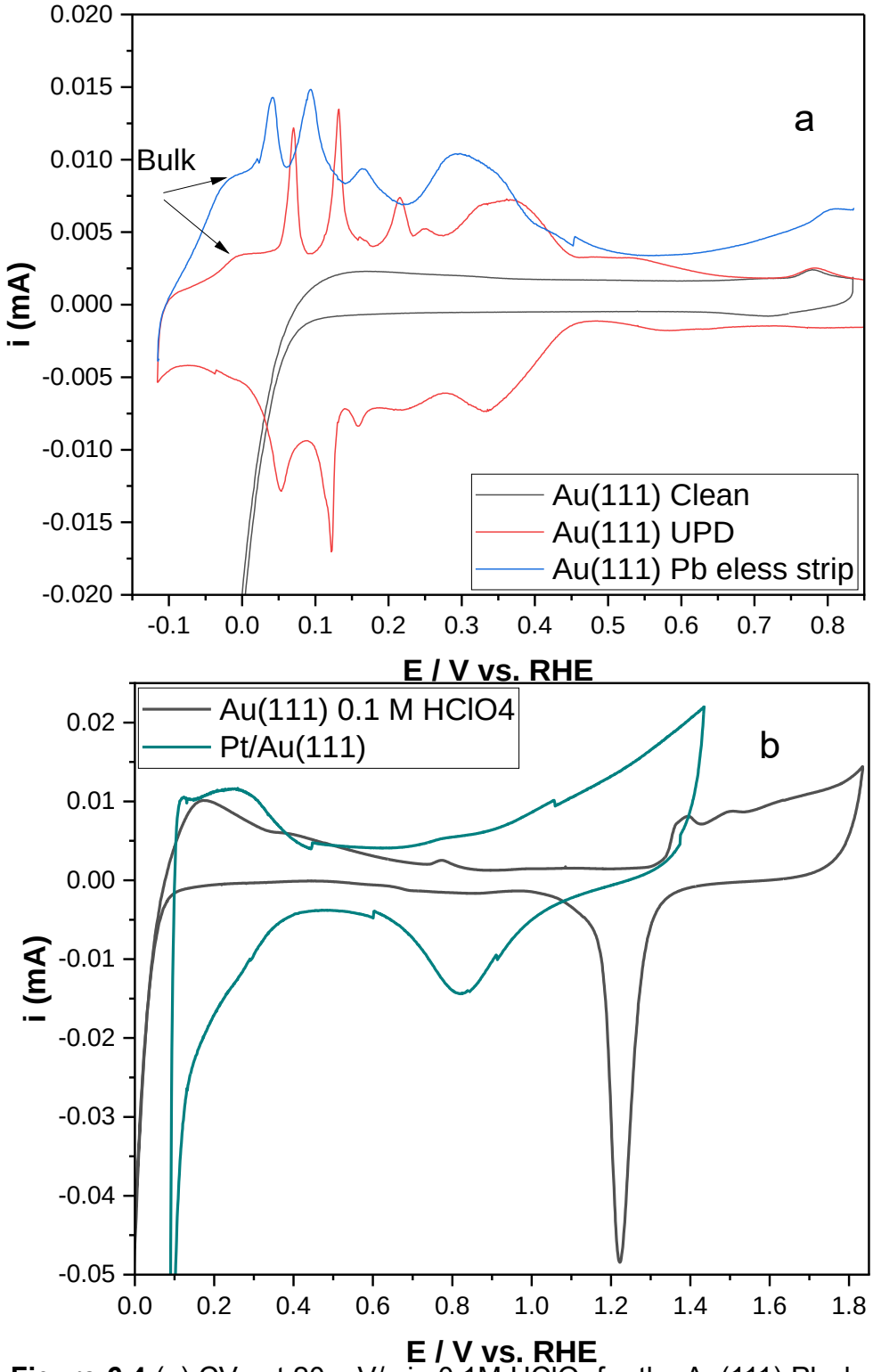

Figure 6.4 (a) CVs at 20 mV/s in 0.1M $HClO_4$ for the Au(111) Pb deposition by UPD and Pb e-less (b) CVs at 20 mV/s in 0.1M $HClO_4$ after the Pb e-less process and Pt SGD.

We followed the Pb e-less deposition process with the SGD using a Pt precursor. The characteristic peaks related to the electrochemical process of Pt—explained in chapter 4 **Figure 4.13**—are seen in **Figure 6.4b**, suggesting that a ML of Pt is obtained in the Au (111) WE. The Pb e-less stripping was also done using other Au monocrystals, Au (110) and Au (100) **Figure 6.5**. All the CVs appear to be similar. Expected peaks for the Au (100) voltammogram in the anodic region near 1.3 V are not seen.

Similarly, the absence of a peak in the cathodic region near 0.87 V should be seen since it was applied a higher potential than 0.5 V to the electrochemical experiment.[5] This peak is related to reconstructing the Au (100) surface to a densely-packed hexagonal layer in $HClO_4$. For the Au (110) electrode, a structure reconstruction should also be seen in $HClO_4$ by cycling the electrode within the Au potential limits. A broader peak at potential ca. 0.9 V in the cathodic region is associated with the Au (110) facet, which is not seen in our electrode. Finally, for the Au (111) a sharper peak should be seen in the OH^- UPD region ca. 1.5 V towards anodic potentials. This peak is associated with the reversible oxidation of OH^- ions between absorbed perchlorate ions.[6] Either the case, a significant peak towards the cathodic potentials at 1.2 V is seen for all electrodes, related to the reduction of AuOx.[7]

Recognizing that we had Au characterized in our electrodes, further studies with Pb UPD measurements for all Au monocrystals in PbO solution diluted in $HClO_4$ **Figure 6.6** were done. The Au monocrystals and Pb UPD CVs are shown

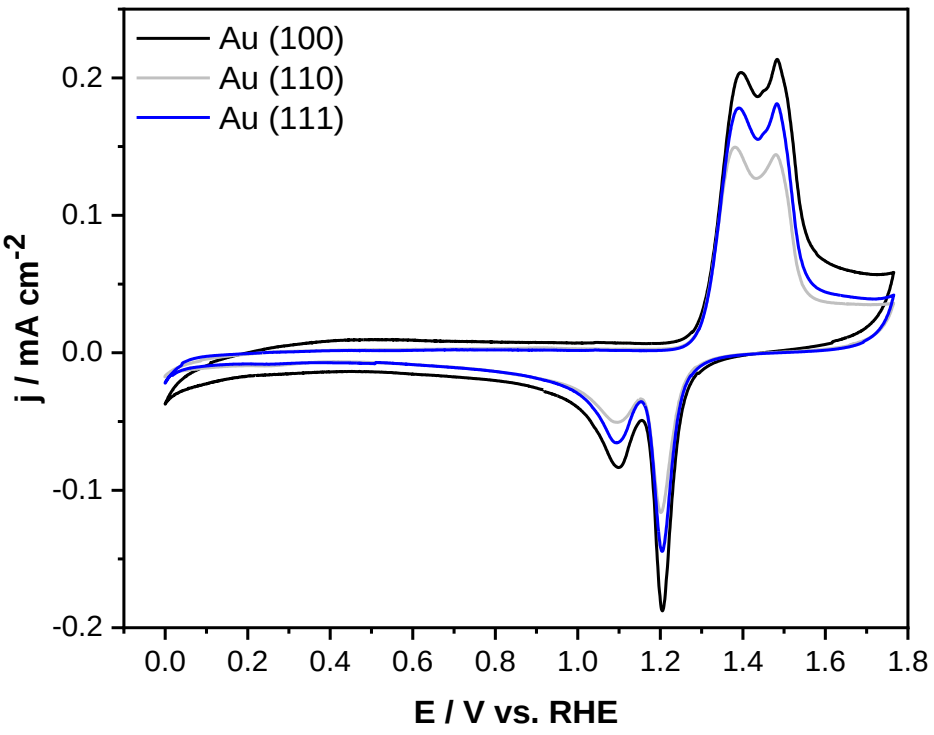

Figure 6.5 Au CVs for the Au (100), (110) and (111) monocrystals in 0.1M $HClO_4$ at 20 mV/s.

in **Figure 6.6a,** characterizing the presence of both Au and Pb. A close-up of the Pb UPD region of this voltammogram is seen in **Figure 6.6b**. Different Pb UPD peaks are expected for different Au facets.[8] The Au (100) shows five peaks associated with Pb UPD. Au (110) has an absent peak at 0 V and a broader peak at ca. 0.3 V. The Au (111) has two peaks which split due to kinetics processes.[9]

Confirming that we had characteristics signs of the presence of each facet in the Au electrodes, we proceeded to do the SGD of the Pb after the e-less process using a Pd precursor in this case. For the ORR on a Pd surface, the expected trend for best reactivity in $HClO_4$ is Pd (100) >Pd (111) >Pd (110)

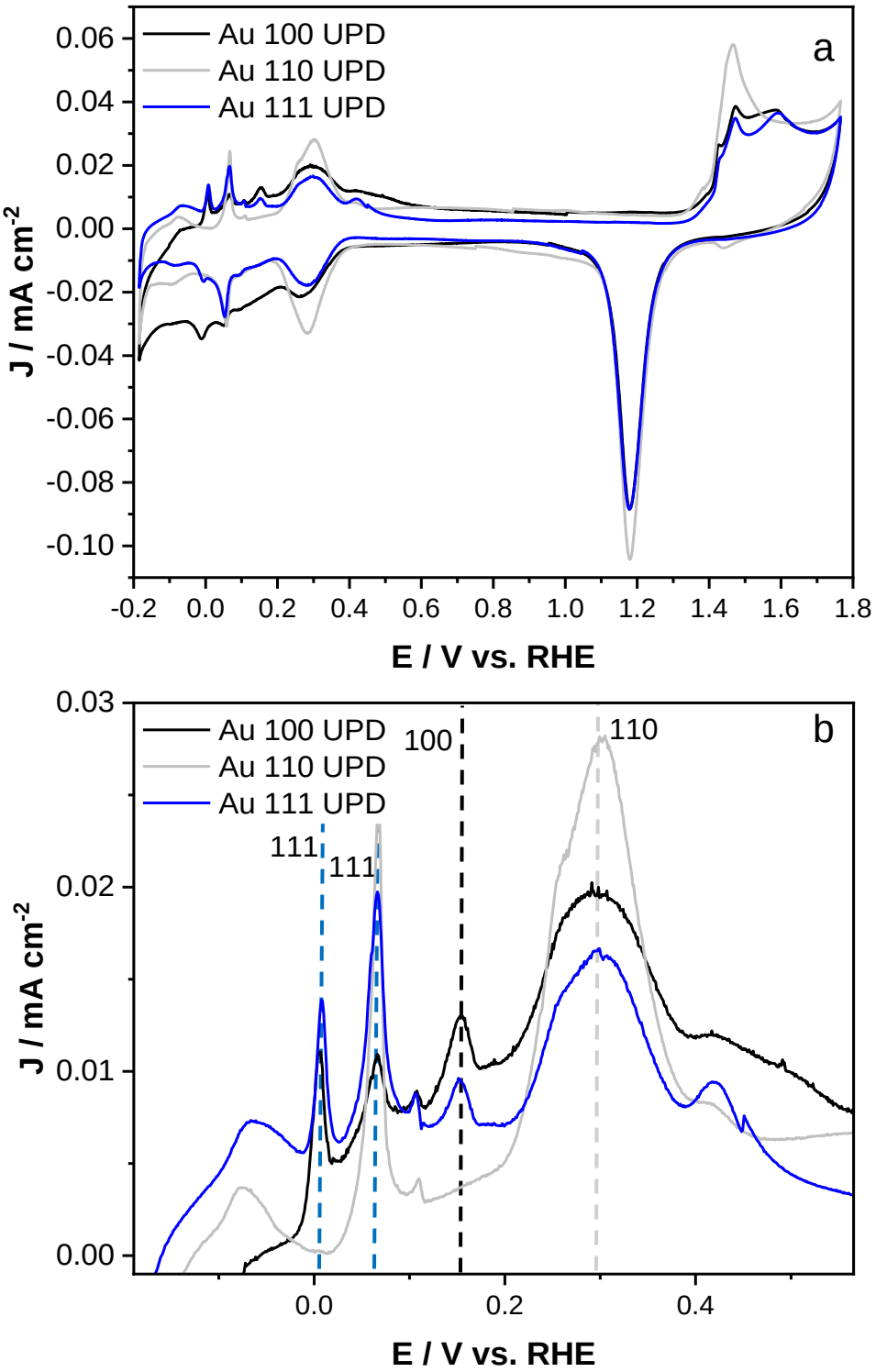

Figure 6.6 (a) Au Pb UPD and (b) Pb UPD region of Au facets. Both in 3.33 mM PbO in 0.1M $HClO_4$ at 20 mV/s.

according to Kondo et. al.[2] The PdAu catalyst oxygen polarization curves in 0.1 M KOH **Figure 6.7** shows the PdAu(100) electrode with an $E_{1/2}$ = 0.2 V, the PdAu(111) with 0.78 V and the PdAu)110) with 0.79 V following a similar trend to what Kondo et al. discussed.

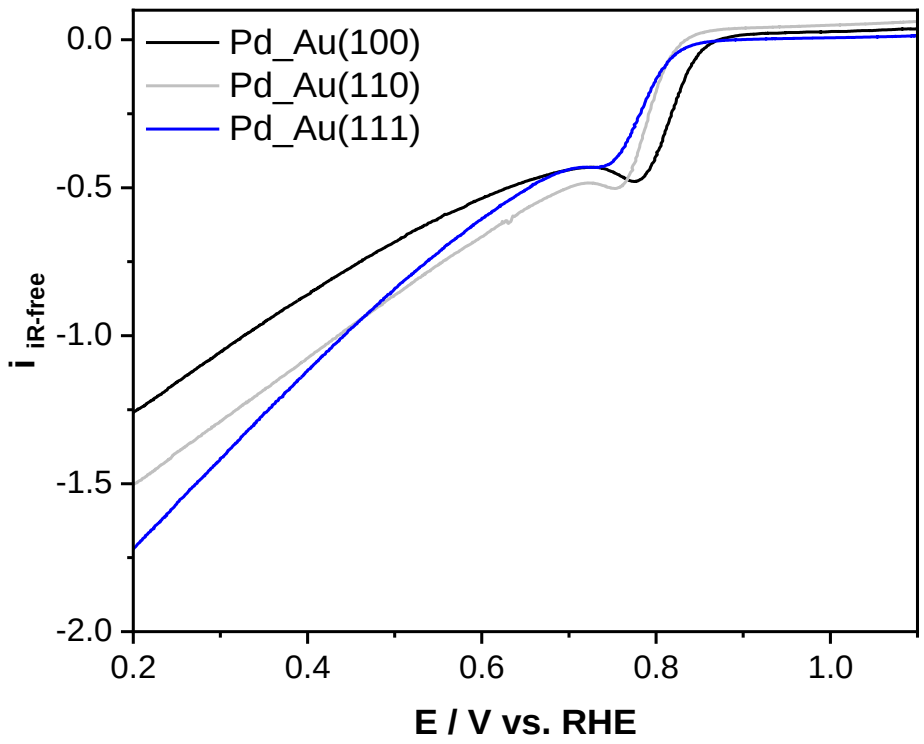

Figure 6.7 LSV corresponding to each PdAu mono with no rotation and 10 mV/s in 0.1M KOH.

Now that the Pb e-less process was confirmed using Au disk electrodes, we proceed to implement the same procedure to commercial Au nanoparticles composed of Au supported on Vulcan carbon (Au/V 20%). The Pb anodic stripping peaks after Pb-eless deposition were compared with Pb UPD on the Au/V 20% catalyst **Figure 6.8**. Similar peaks are found for both voltammograms and the same negative shift is obtained for the anodic stripping

process as for the Au (111) monocrystal **Figure 6.4a**. This same behavior concluded that the Pb e-less approach could be implemented in metal carbide nanoparticles.

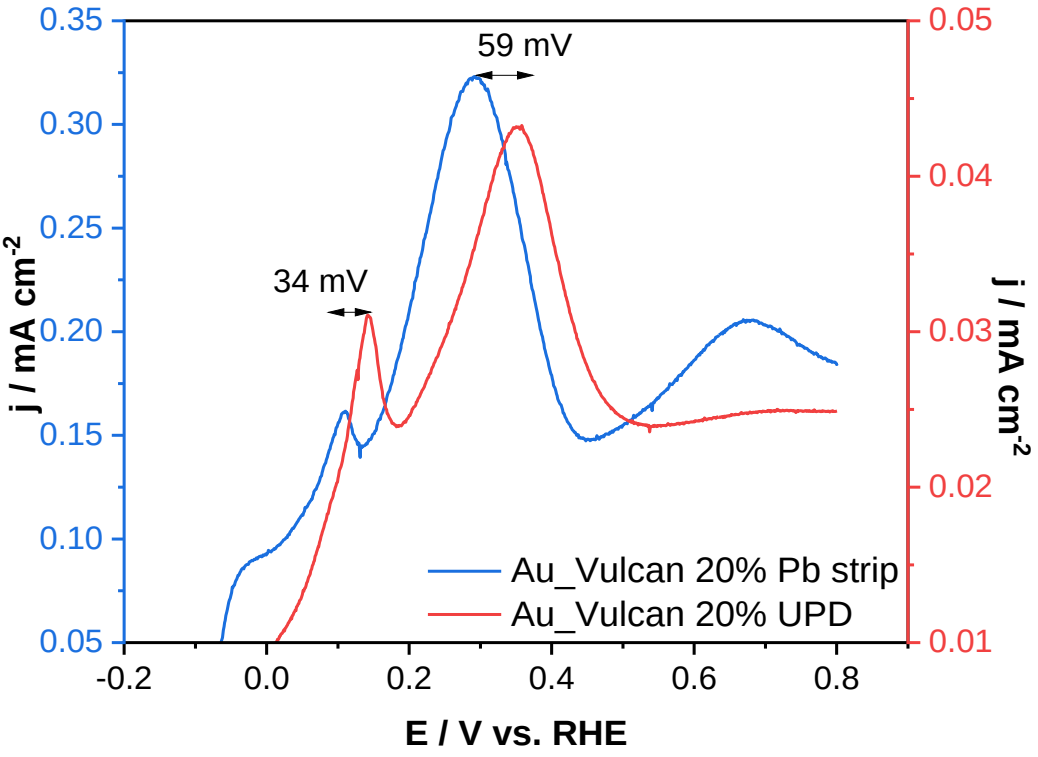

Figure 6.8 CVs of Au/V 20% at 20 mV/s in 0.1M $HClO_4$ in the UPD region of Pb comparing the Pb anodic stripping after the Pb e-less deposition and the Pb UPD measurements in PbO solution.

6.4.1.2.Nitrides Pb deposition

Subsequently, Nb/N supported on V nanoparticles were used as supports for the Pb e-less deposition. The OCP transient **Figure 6.9** demonstrated the Pb e-less process as expected. Then, the SGD of Pb was done using a Pt precursor. The voltammogram of the PtNbN/V sample is seen in **Figure 6.10a** with the Pt characteristic peaks. In this case, we decided to compare the Pb e-less

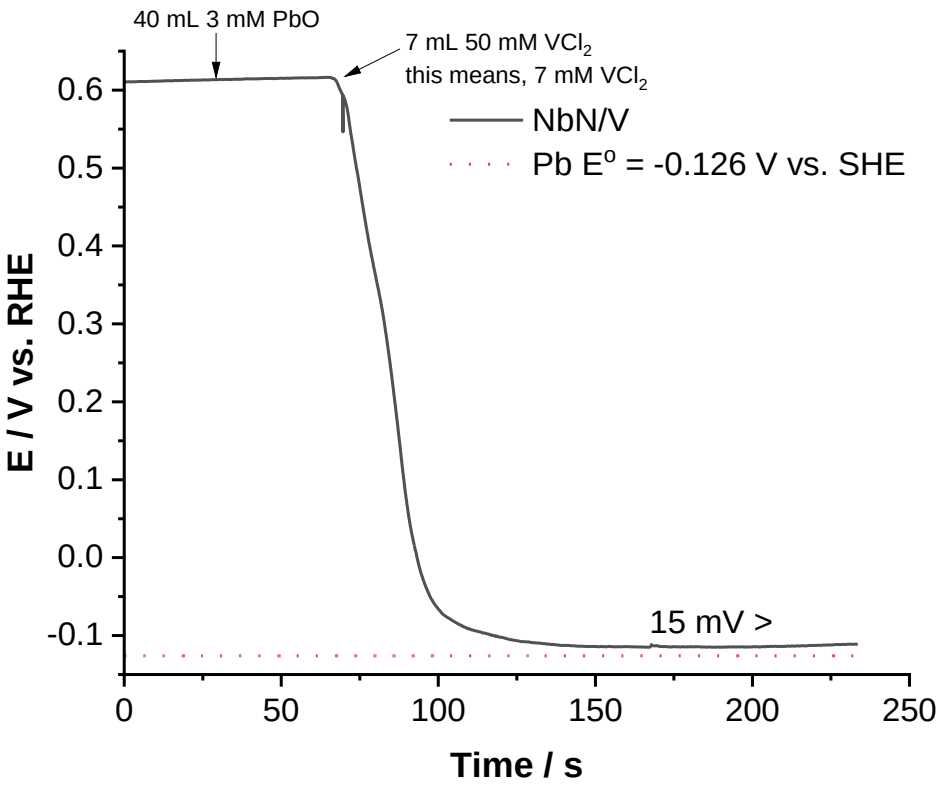

Figure 6.9 OCP transient of the Pb e-lees process for NbN/V in 0.1M $HClO_4$.

process after several e-less cycles (no cycle, 1 and 10) **Figure 6.10b**, a difference in the Pt peaks at the hydrogen UPD region and the PtO region are noticed. With no Pb e-eless process by just immersing the GC WE modified with the NbN/V inside the Pt precursor solution, adsorption processes could happen; therefore, we can see the presence of Pt peaks on the voltammograms. However, an increment in the current of both monitored Pt regions increases as the Pb e-less cycles is increased, indicating that the deposition of Pt is enhanced by repetitive cycles of the e-less process.

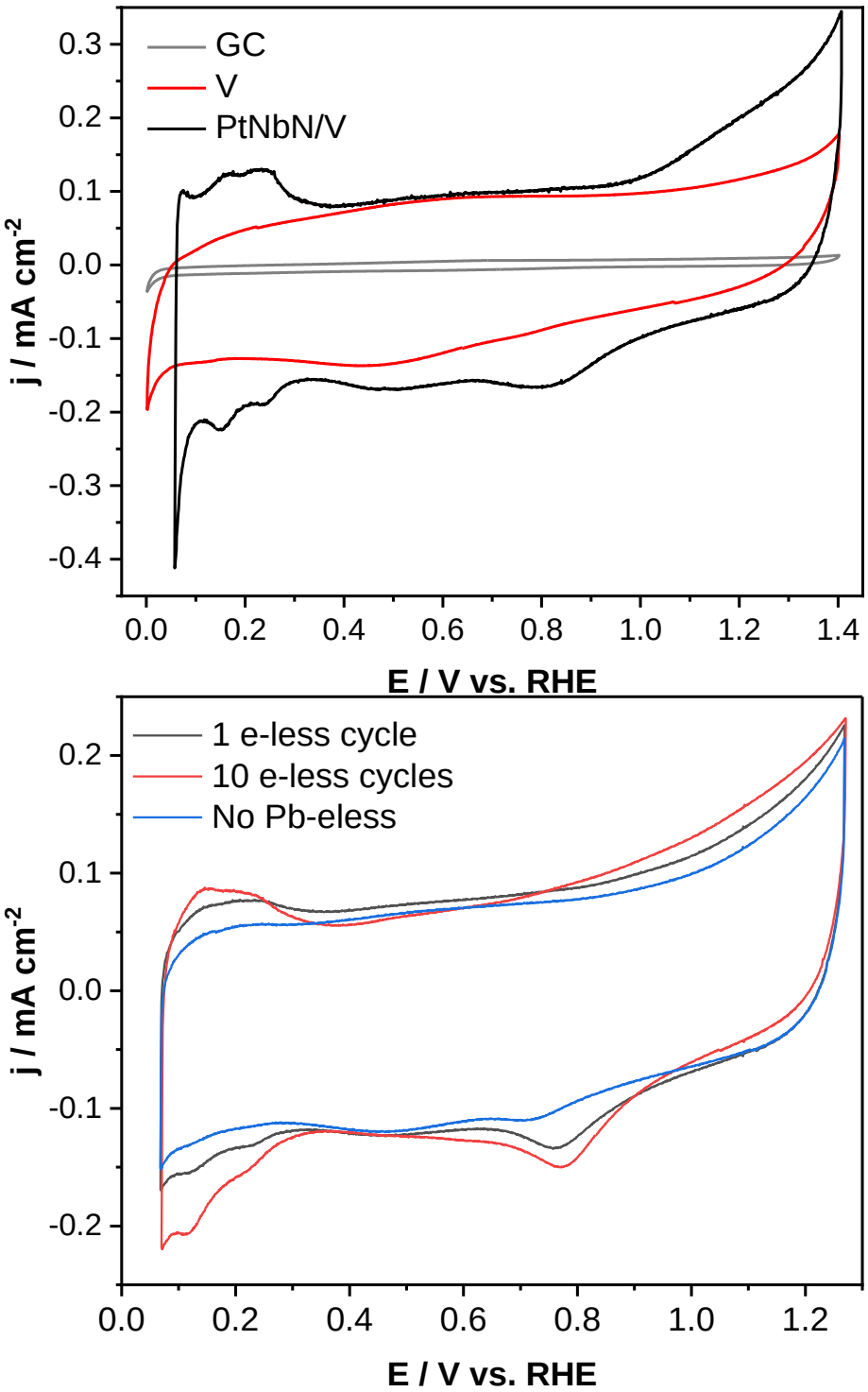

Figure 6.10 Cyclic voltammograms of Pt-NbN/V at 25 mV/s in 0.1M $HClO_4$.

STEM EDS measurements were done after obtaining the different Pt-Nb/V samples **Figure 6.11**. The e-less process with only 1 cycle demonstrated that the Pt atoms were very dispersed in the sample with no preferred deposition on the Nb substrate. However, after 5 cycles of the e-less procedure, a more concentrated allocation of the Pt atoms is seen on the Nb spots. The formation of Pt-Nb/V nanoparticles with sizes of ca. 20 nm could also be seen. After 10 cycles, the Pt atoms' presence is seen on the Nb spots with similar sizes to what was found for the previous Pt-Nb/V nanoparticles. With these images, we can confirm the correlation between doing more cycles of the Pb e-less process and having enhanced current associated with Pt redox process, as seen in **Figure 6.10**.

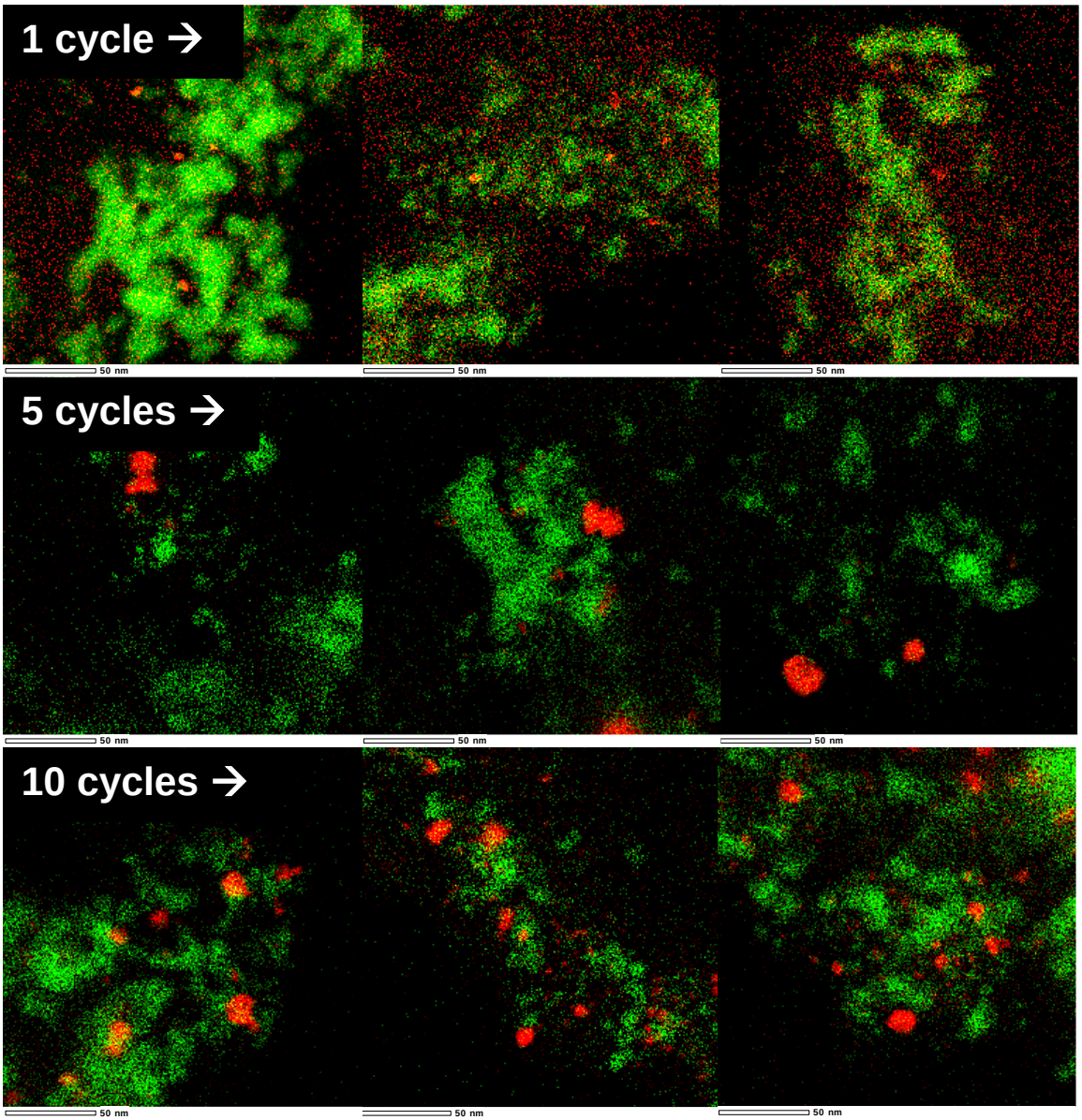

Figure 6.11 STEM EDS mapping of Pt-Nb/V samples after 1, 5 and 10 Pb e-less deposition cycles and SGD using the Pt precursor. The green dots represent Nb atoms and the red dots represent the Pt atoms.

6.4.1.3.Cu depositions

The next support that we decided to study was Cu. The characterization of the Pb e-less deposition on Cu (100) nanoparticles is demonstrated in **Figure 6.12**, where the OCP transient followed the explained process in section 6.4.1.1. Then, the Pb UPD experiments were held for the Cu (100) nanoparticles, a Cu (*hkl*) disk and polycrystalline commercial Cu/V 20% nanoparticles **Figure 6.13**. A significant peak at ca. 0.02 V associated with a Pb ML[10] is seen for the three samples.

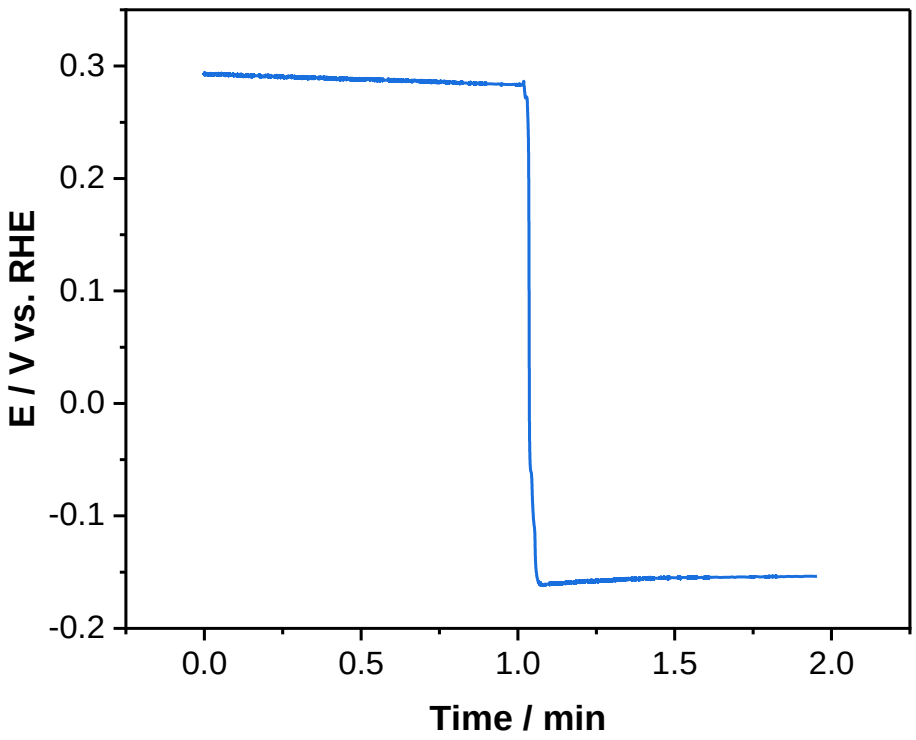

Figure 6.12 OCP transient of the Pb e-less deposition on Cu (111) nanoparticles.

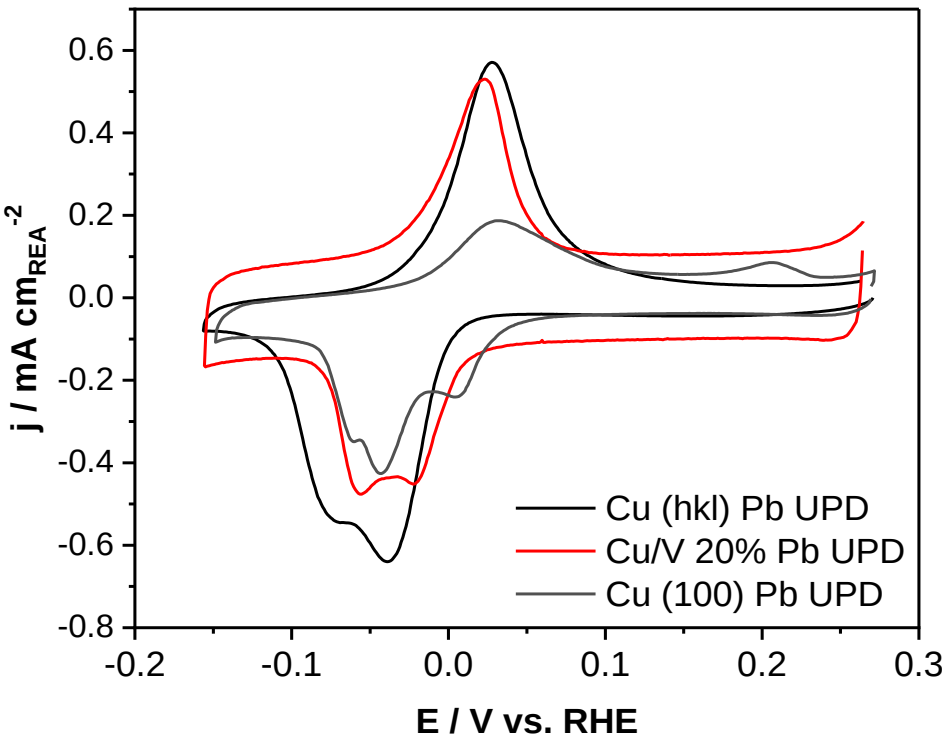

Figure 6.13 CVs of Cu samples in the UPD region of Pb in 3.33 mM PbO in 0.1 M $HClO_4$ at 20 mV/s.

To further corroborate the Pb e-less method, we compare the charge values of the Cu(*hkl*) disk anodic stripping and UPD measurements **Figure 6.14**. These charges are associated with a full Pb ML on the Cu support and according to Vasilic et al. a theoretical charge value of ca. 300 μC cm^{-2} is expected.[10] The anodic stripping provided 293 μC cm^{-2} and the Pb UPD measurements 311 μC cm^{-2} **Table 6.1**, suggesting that the formation of a full Pb ML on the Cu (*hkl*) disk was achieved. The electrochemical properties of the PdCu samples were tested for the ORR in 0.1 M KOH. In **Figure 6.15a** the Cu (100) cubes nanoparticles were characterized, showing that Cu's typical redox process in an alkaline medium is obtained as explained in chapter 3, section 3.3.4. These Cu (100) cubes were further modified

with the Pd precursor following the Pb e-less procedure and the SGD **Figure 6.15b** and the typical redox Pd process is seen, highlighting the PdO ML reduction peak at ca. 0.7 V.[11] The oxygen polarization curves at 1,600 rpm for the PdCu (100), PdCu/V 20% (here, the Cu/V 20% is a commercial catalyst) and the commercial Pd/V 20% are shown in **Figure 6.15c**. The PdCu (100) sample shows superior current density and improved $E_{1/2}$ potential with 0.88 V, indicating that the Pd (100) facet has better ORR activity compared with Pd (*hkl*) samples as previously explained by Kondo et al.[2]. The KL analysis was done for the PdCu (100) catalyst **Figure 6.15d**, 3.92 e^- were obtained, confirming that the PdCu (100) followed a 4-electron pathway to produce water.

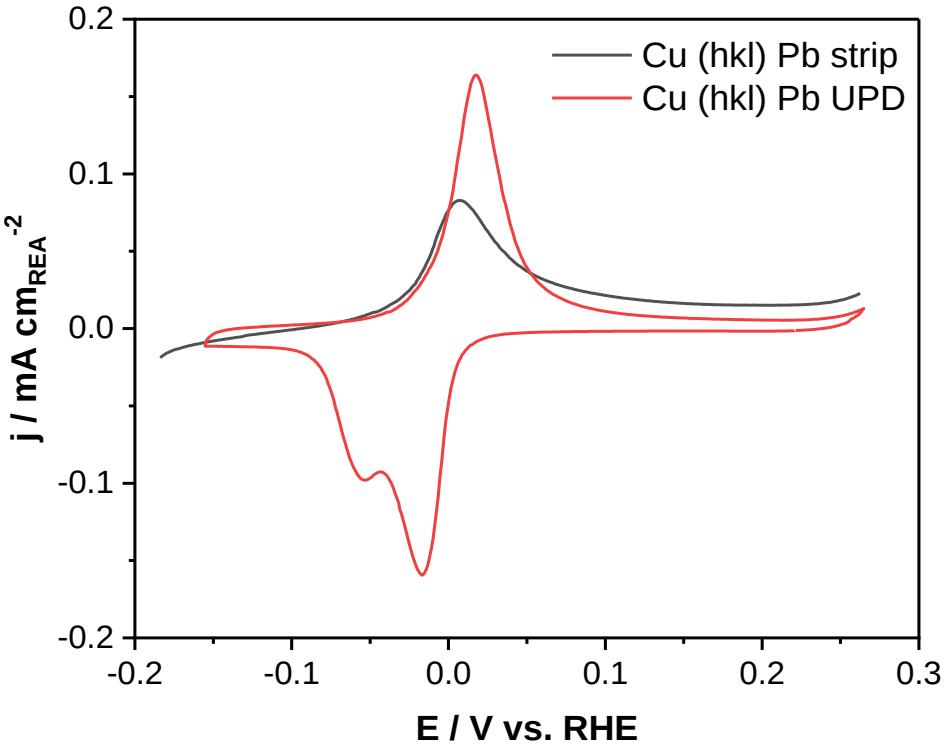

Figure 6.14 CVs of Cu samples in the UPD region of Pb in 3.33 mM PbO in 0.1 M $HClO_4$ at 20 mV/s.

Table 6.1 Cu real surface area values and Pb charge densities for polycrystalline standards.

Sample	*Cu real surface area (cm^2)*	*Pb Charge density ($\mu C\ cm^{-2}$)*
Cu poly STRIP	0.95	293.5
Cu poly UPD	0.95	311.7
Cu/V 20% UPD	0.28	262.6

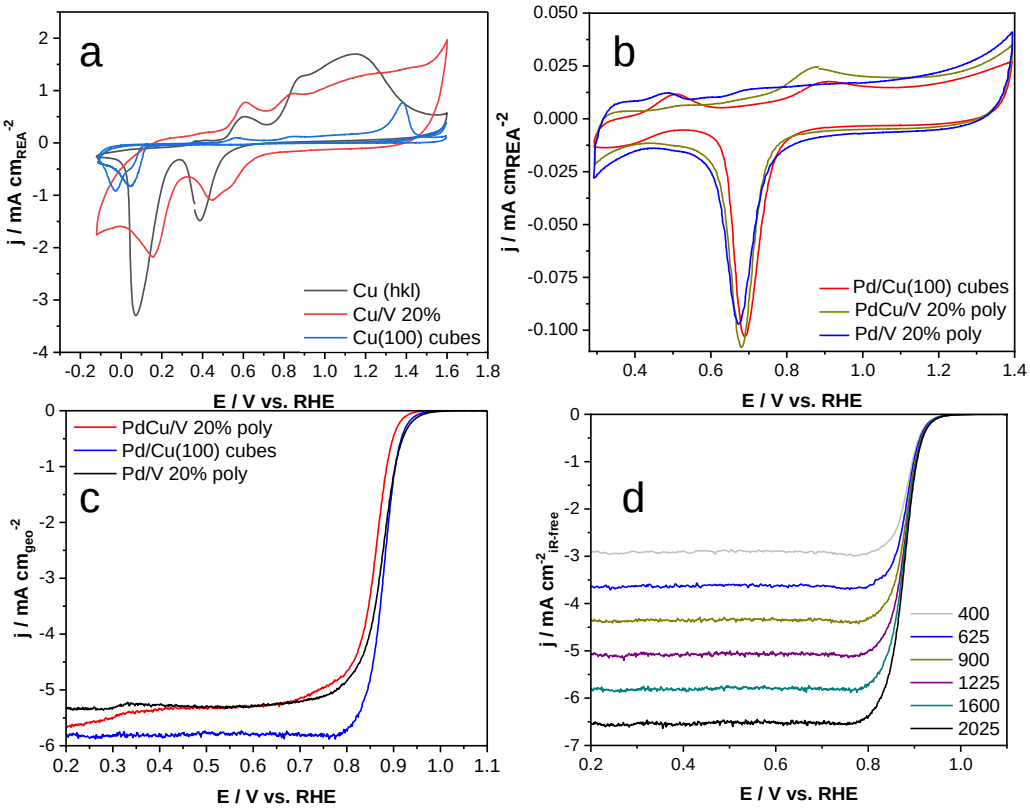

Figure 6.15 (a) Voltammograms of the Cu catalysts in the typical potential window of Cu at 20 mV/s. (b) Voltammograms of the Cu catalysts modified with Pd after the Pb e-less deposition (PdCu(poly) commercial and PdCu(100)) and Pd/V commercial catalysts at 20 mV/s. (c) LSV of the PdCu(poly) commercial, PdCu(100) and Pd/V catalysts at 1,600 rpm and 10 mV/s. (d) Koutecký-Levich plots varying the rotation rate (rpm) at 10 mV/s for the PdCu(100) catalysts demonstrating a four-electron pathway for the ORR. All electrochemical experiments were done in a 0.1 M KOH solution.

6.5. Conclusions:

The Pb e-less procedure was applied to Au, Nb and Cu samples. We were able to use different substrates, disks, and nanoparticles. The Au experiments confirmed that the Pb e-less process is facet specific. Then, we were able to confirm that the Pb deposition process could be done with a catalyst in nanoparticle powder form. This was useful for the upcoming NbN/V experiments. We characterized the samples using STEM-EDS and showed that repetition of the deposition of Pb and the SGD with the metal precursor provides different deposition results after 5 cycles, the Pt atoms are located on the Nb spots.

To finalize, we applied the procedure to Cu electrodes, specifically Cu (100), to obtaining PdCu (100) for the ORR. The Pb e-less ML deposition was confirmed with UPD and anodic stripping measurements using a Cu (*hkl*) disk. The electrochemical results indicated that the PdCu (100) catalyst had better ORR performance than commercial Pd/V 20% and a Pb e-less catalysts (PdCu/V 20%) made with commercial Cu/V 20% and Pd. We also held the KL analysis, where the 4 electron pathway was confirmed. The synthesis of different catalysts for the ORR using the Pb e-less deposition method was successful. Further experiments are suggested to confirm the Au and Nb Pb ML charge values. This catalyst should be used for other energy conversion reactions such as EtOH oxidation, HER, HOR or OER.

6.6. References:

(1) Wu, D.; Solanki, D. J.; Ramirez, J. L.; Yang, W.; Joi, A.; Dordi, Y.; Dole, N.; Brankovic, S. R. Electroless Deposition of Pb Monolayer : A New Process and Application to Surface Selective Atomic Layer Deposition. **2018**, *38*, 11384–11394.

(2) Kondo, S.; Nakamura, M.; Maki, N.; Hoshi, N. Active Sites for the Oxygen Reduction Reaction on the Low and High Index Planes of Palladium. *J. Phys. Chem. C* **2009**, *113*, 12625–12625.

(3) Choi, D.; Kumta, P. N. Synthesis and Characterization of Nanostructured Niobium and Molybdenum Nitrides by a Two-Step Transition Metal Halide Approach. *J. Am. Ceram. Soc.* **2011**, *94*, 2371–2378.

(4) Budevski, E.; Staikov, G.; Lorenz, W. J. *In Electrochemical Phase Formation and Growth*; Alkire, R.C. et al Ed. VCH: Berlin, 1996.

(5) Tidswell, I. M.; Marković, N. M.; Lucas, C. A.; Ross, P. N. In Situ X-Ray-Scattering Study of the Au(001) Reconstruction in Alkaline and Acidic Electrolytes. *Phys. Rev. B* **1993**, *47*, 16542–16553.

(6) Hamelin, A.; Martins, A. M. Cyclic Voltammetry at Gold Single-Crystal Surfaces. Part 2. Behaviour of High-Index Faces. *J. Electroanal. Chem.* **1996**, *407*, 13–21.

(7) Łukaszewski, M.; Soszko, M.; Czerwiński, A. Electrochemical Methods of Real Surface Area Determination of Noble Metal Electrodes-an Overview. *Int. J. Electrochem. Sci* **2016**, *11*, 4442–4469.

(8) Herrero, E.; Buller, L. J.; Abruña, H. D. Underpotential Deposition at Single Crystal Surfaces of Au, Pt, Ag and Other Materials. *Chem. Rev.* **2001**, *101*, 1897–1930.

(9) Tao, N. J.; Pan, J.; Li, Y.; Oden, P. I.; DeRose, J. A.; Lindsay, S. M. Initial Stage of Underpotential Deposition of Pb on Reconstructed and Unreconstructed Au(111). *Surf. Sci.* **1992**, *271*, L338–L344.

(10) Vasilic, R.; Vasiljevic, N.; Dimitrov, N. Open Circuit Stability of Underpotentially Deposited Pb Monolayer on Cu(111). *J. Electroanal. Chem.* **2005**, *580*, 203–212.

(11) Liang, Z. X.; Zhao, T. S.; Xu, J. B.; Zhu, L. D. Mechanism Study of the Ethanol Oxidation Reaction on Palladium in Alkaline Media. *Electrochim. Acta* **2009**, *54*, 2203–2208.

Chapter 7. **General conclusions**

In this thesis work, we synthesized PGM catalysts alloyed using first-row transition metals with different structures by various methods. All these catalysts were tested for the ORR in an alkaline medium. The synthesis of PtNi-NWs/V led to better specific activities than commercial Pt/V catalysts. As of our understanding, we were the first to implement an electrochemical *in situ* XAS methodology for PtNi/NW catalysts in an alkaline medium. These experiments confirmed that Pt and Ni were alloyed in the PtNi/NW and that the electronic structure of Pt is changed as an electrochemical potential is applied to the electrochemical system under an oxygen atmosphere.

The use of catalysts with nanoparticle shapes was not the exception in our dissertation work; we expanded the RoDSE methodology by successfully electrodepositing Ni, Co and Cu catalysts on carbon V support for the first time. These catalysts were modified with Pt to obtain PtNi/V, PtCo/V and PtCu/V. According to the TEM results, the sizes of these catalyst resulted with ca. 2-3 nm in diameter, and low Pt loadings of ca. 2% were achieved on each catalyst. After evaluating their performance for the ORR, all the catalysts surpassed the mass activity of commercial Pt/V catalysts in an alkaline medium. Further, *in situ* electrochemical XAS studies using the Pt L_3 edge confirmed that the low amounts of Pt in our catalyst could be monitored by the technique showing changes in the whiteline intensity as different applied potentials.

We then proceeded to synthesize ML catalyst to maximize and tunned the use of PGM. PdCu (100) NPs were obtained following a Pb e-less method based

on the chemical interaction between Pb and V in $HClO_4$. The Pd ML on the PdCu (100) was confirmed calculating the Pb UPD and e-less charge densities, which gave close values to the Pb theoretical charge density. The PdCu (100) catalyst was tested for the ORR in alkaline electrolyte and obtained a better $E_{1/2}$ than a Pd (*hkl*)/V commercial catalysts.

7.1. Future perspectives

The tunning of the Pt loading on the PtNi/NWs is suggested to be improved to promote the catalysts' mass activities. Other catalysts such as PtCo/NW and PdCu/NW are recommended for synthesis, recognizing the excelled mass activity of PtCo/V nanoparticles versus commercial Pt/V and the PdCu (100) ML catalysts versus the PtCu (*hkl*) commercial catalysts. The leaching behavior of the catalyst is recommended to be examined as durability experiments are executed. The experimental protocol regarding the *in situ* electrochemical experiments is recommended to be followed to get detailed information regarding the changes in the chemical structure of the electrocatalysts. Finally, the PtNi/NWs, PtCo/V and the PdCu/ (100) catalysts are recommended for further experiments in the cathode of an AEMFCs.

Appendix A. List of publications and contributions to the University of Puerto Rico

- Vélez, C.; Corchado-García, J.; Rojas-Pérez, A.; J. Serrano-Alejandro, E.; Santos-Homs, C.; **Soto-Pérez, J**.; Cabrera, C., Manufacture of Pd/Carbon Vulcan XC-72R Nanoflakes Catalysts for Ethanol Oxidation Reaction in Alkaline Media by RoDSE Method. *J. Electrochem. Soc***. 2017**, 164, D1015-D1021. https://doi.org/10.1149/2.1041714jes.
- Vélez, C.; **Soto-Pérez, J**.; Corchado-García, J.; Larios, E.; Fulvio, P.; Echegoyen, L.; Cabrera, C., Palladium Electrodepostion on Unsupported Carbon Nano Onions: A Glucose Oxidation Study in Alkaline Media. *J. Solid. State. Electrochem.* **2021**, 25, 207-217. https://doi.org/10.1007/s10008-020-04729-5.
- **Soto-Pérez, J.**; Betancourt, L. E.; Trinidad, P.; Larios, E.; Rojas-Pérez, A.; Quintana, G.; Sasaki, K.; Pollock, C. J.; Debefve, L. M.; Cabrera, C. R. In Situ X-Ray Absorption Spectroscopy of PtNi-Nanowire/Vulcan XC-72R under Oxygen Reduction Reaction in Alkaline Media. *ACS Omega* **2021**, 27, 17203–17216. https://doi.org/10.1021/acsomega.1c00792.
- **Soto-Pérez, J**.; Peña, A.; Trinidad, P.; Zhao, X.; Quintana, G.; Sasaki, K.; Cabrera, C. Ni, Co and Cu modified with Pt as Catalysts for the Oxygen Evolution Reaction and Oxygen Reduction Reaction in Alkaline Medium. Manuscript in preparation, **2022**.
- **Soto-Pérez, J**.; Lu, F.; Zhang, Y.; Sasaki, K.; Cabrera, C. Pb electroless deposition on nitrides and carbides. Manuscript in preparation, **2022**.
- Martinez R.; Cruz, E.; Zografos, S.; Santillan, J.; **Soto, J**.; Palai, R.; Nicolau, E.; Cabrera, C. Perovskite materials for electrochemical energy storage in hybrid supercapacitors. Manuscript in preparation, **2022**.
- **Soto-Pérez, J**.; Peña-Duarte, A.; Cabrera, C. Chalcogenides and electrocatalysis. Manuscript in preparation, **2022**.
- Rivera-Reyez, J.; **Soto-Pérez, J**.; Trinidad-Pérez, P.; Luna-Ramirez, Alanys.; Cabrera-Martínez, C.; Jones, J. P.; Piñero-Cruz, D. New palladium and platinum complexes from a salen and a hydroxy-substituted salpn-naphthalene ligands with CO_2 reduction activity. Manuscript in preparation, **2022**.